E.O. Paton Electric Welding Institute of the National Academy of Science of Ukraine
International Association “Welding”

The Paton Welding Journal

12
2025

International Scientific-Technical and Production Journal ♦ Founded in January 2000 (12 Issues Per Year)

Address of Editorial Office:
E.O. Paton Electric Welding Institute, 11 Kazymyr Malevych Str., 03150, Kyiv, Ukraine
E-mail: office@paton.kiev.ua; https://paton.org.ua/en/

Address of Publisher:
International Association “Welding”, 11 Kazymyr Malevych Str., 03150, Kyiv, Ukraine
Tel.: (38044) 205 23 90, E-mail: patonpublishinghouse@gmail.com; journal@paton.kiev.ua
https://patonpublishinghouse.com/eng/journals/tpwj

The Journal was registered by the National Council of Ukraine on Television and Radio Broadcasting on 09.05.2024, carrier identifier R30-04569
ISSN 0957-798X (Print), ISSN 3041-2293 (Online)
DOI: https://doi.org/10.37434/tpwj, from #01, 2020 to now; DOI: https: //doi.org/10.15407/tpwj from #01, 2014 to #12, 2019.

Subscriptions, 12 issues per year:
348 Euro — annual subscription for the printed (hard copy) version, air postage and packaging included;
288 Euro — annual subscription for the electronic version (sending issues in pdf format or providing access to IP addresses).

Representative Offices of “The Paton Welding Journal”:

BRAZIL, Arc Dynamics
Address: Nova Iguacu, Rio de Janeiro, Brazil
Daniel Adolpho, Tel.: +55 21 9 6419 5703,
E-mail: dadolpho@arcdynamics.com.br

CHINA, China-Ukraine Institute of Welding, Guangdong Academy of Sciences
Address: Room 210, No. 363 Changxing Road, Tianhe, Guangzhou, 510650, China
Zhang Yupeng, Tel.: +86-20-61086791,
E-mail: patonjournal@gwi.gd.cn

BULGARIA, Bulgarian Welding Society
Address: Blvd. Asen Yordanov No.10, Sofia 1592, Bulgaria
Pavel Popgeorgiev, Tel.: +359 899 96 22 20,
E-mail: office@bws-bg.org

POLAND, PATON EUROPE Sp. z o. o.
Address: ul. Kapitałowa 4, 35-213, Rzeszów, Poland
Anton Stepakhno, Tel.: +38067 509 95 67,
E-mail: Anton.Stepakhno@paton.ua

The content of the Journal includes articles received from authors from around the world in the field of welding, cutting, cladding, soldering, brazing, coating, 3D additive technologies, electrometallurgy, material science, NDT and selectively includes translations into English of articles from the following journals, published in Ukrainian:

- «Avtomatychne Zvaryuvannya» (Automatic Welding), https://patonpublishinghouse.com/eng/journals/as;
- «Suchasna Elektrometalurhiya» (Electrometallurgy Today), https://patonpublishinghouse.com/eng/journals/sem;
- «Tekhnichna Diahnostyka ta Neruinivnyi Kontrol» (Technical Diagnostics & Nondestructive Testing), https://patonpublishinghouse.com/eng/journals/tdnk.

CONTENTS

ORIGINAL ARTICLES

INFORMATION

*Translated Article(s) from “Avtomatychne Zvaryuvannya” (Automatic Welding), No. 6, 2025.

**Translated Article(s) from “Suchasna Elektrometalurhiya” (Electrometallurgy Today), No. 4, 2025.

***Translated Article(s) from “Tekhnichna Diahnostyka ta Neruinivnyi Kontrol” (Technical Diagnostics & Nondestructive Testing), No. 3, 2025.

Indexing: The electronic edition of the Journal is stored in the V.I. Vernadsky National Library of Ukraine (eVerLib), included in the OPEN UKRAINIAN CITATION INDEX database and international databases: CROSSREF, EBSCO, Google Scholar, INDEX COPERNICUS, ULRICHSWEB.

DOI: https://doi.org/10.37434/tpwj2025.12.01

STRUCTURE AND PROPERTIES OF WELDED JOINTS OF PT-3V TITANIUM ALLOY PRODUCED BY NARROW-GAP WELDING

S.V. Akhonin, V.Yu. Bilous, R.V. Selin

E.O. Paton Electric Welding Institute of the NASU
11 Kazymyr Malevych Str., 03150, Kyiv, Ukraine

ABSTRACT

Narrow-gap gas tungsten arc welding is an efficient and economical method for producing joints in thick titanium alloys. A key feature of the developed technology is the stable chemical composition of the weld metal, with the proportion of base metal in the weld reaching 89–91%. This work examines the influence of filler material on the structure and properties of welded joints in PT-3V titanium alloy produced by narrow-gap welding with a tungsten electrode and magnetically controlled arc. Filler wires of grades 2V and SPT2 provide high-quality formation of a concave weld bead surface during narrow-gap welding of PT-3V titanium alloy. The tensile strength of welded joints produced using 2V filler wire reaches 643 MPa, corresponding to 86 % of the strength of the base metal. The use of SPT2 filler wire for narrow-gap welding of PT-3V titanium alloy made it possible to obtain a weld metal structure similar to that of the base metal and to achieve weld strength equivalent to that of the base metal in the as-welded condition.

KEYWORDS: titanium, titanium alloy, pseudo-α alloys, gas tungsten arc welding, narrow-gap welding, controlling magnetic field, filler wire, microstructure, mechanical properties

INTRODUCTION

Narrow-gap gas tungsten arc welding is an efficient and economical method for producing joints in thick titanium alloys [1, 2]. For welded joints of titanium alloys, it is particularly important to reduce the consumption of filler wire and simplify the joint edge preparation [3, 4].

At the E.O. Paton Electric Welding Institute, a method for narrow-gap welding (NGW) with a tungsten electrode and magnetically controlled arc has been developed [5]. This welding method offers advantages such as a narrow weld width and a small volume of deposited filler metal [6, 7]. Another important feature of the technology is the simple joint edge design [8]. In addition, welding is performed under constant parameters. The weld metal has a stable chemical composition [9, 10], and the proportion of base metal in the weld metal reaches 89–91 %.

For welding PT-3V alloy joints by both manual and automatic arc welding, filler materials of grades VT1-00sv and 2V according to TUU 05416923.041–98 or GOST 27265–87 are recommended. VT1-00sv is an unalloyed titanium wire with a tensile strength of σ_t = 295–470 MPa. Since tungsten arc NGW with magnetically controlled arc results in a high proportion of filler metal in the weld formation, the mechanical properties of welded joints produced by NGW are primarily determined by the properties of the filler wire material [11]. Therefore, to ensure high strength of the weld metal and the welded joint, the use of 2V filler wire (Ti–Al–V system) is necessary.

However, the 2V filler wire is less alloyed compared to the base PT-3V titanium alloy, which results in lower weld metal strength compared to the base metal. To achieve equal-strength weld joints using NGW, it would be desirable to use filler wire with a chemical composition equivalent to PT-3V alloy. Unfortunately, such filler wire is not specified in TUU 05416923.041–98 or GOST 27265–87, therefore it is reasonable to investigate the possibility of using alternative filler wires.

Thus, it is important to study the influence of the chemical composition of various filler wires on the properties of welded joints of PT-3V titanium alloy produced by NGW with a magnetically controlled arc.

OBJECTIVE OF THE WORK

To investigate the influence of filler material on the structure and properties of welded joints of PT-3V titanium alloy produced by NGW with a tungsten electrode under a controlling magnetic field.

MATERIALS AND METHODS

To achieve this objective, multipass NGW with a magnetically controlled arc was performed on 45-mm-thick specimens made of PT-3V titanium alloy (Ti–Al–V system), GOST 19807–91. The chemical composition of PT-3V alloy is given in Table 1, and the mechanical properties for 12–60 mm thickness are listed in Table 2. The length of the test samples for welding was 600 mm.

Table 1. Chemical composition of PT-3V titanium alloy (GOST 19807–91), wt.%

Main components			Impurities, not more than							
Ti	Al	V	Zr	Si	Fe	C	O_2	N_2	H_2	Total other impurities
Base	3.5–5.0	1.2–2.5	0.3	0.12	0.25	0.1	0.15	0.04	0.015	0.30

Table 2. Mechanical properties of PT-3V titanium alloy sheets (GOST 19807–91)

Sheet thickness, mm	Ultimate tensile strength (σ_t), MPa	Elongation (δ), %	Reduction of area (φ), %	Impact toughness (*KCU*), kJ/m^2
		No less than		
12–19	638–834	11	25	687
20–60	638–814	10	15	

Table 3. Chemical composition of filler wires 2V and SPT2 (GOST 27265–87), wt.%

Grade	Main components				Impurities, not more than						
	Ti	Al	V	Zr	Si	Fe	C	O_2	N_2	H_2	Total other impurities
2V	Balance	1.5–2.5	1.0–2.0	–	0.10	0.20	0.07	0.12	0.04	0.003	0.30
SPT2		3.0–5.5	2.5–3.5	1.0–2.0		0,15	0,05				

Mechanical properties of the welded joints were determined at room temperature using specimens cut out from the base metal and the weld metal. Static tensile tests were carried out on cylindrical specimens of type MI-12, while impact toughness (*KCV*) was evaluated using sharp-notch specimens of type MI-50.

For welding the PT-3V titanium alloy, it is recommended to use filler wires made of commercially pure titanium grade VT1-00sv or the alloyed filler wire grade 2V (Ti–Al–V system) (Table 3). The mechanical properties of the 2V filler wire are presented in Table 4. To achieve strength matching in the welded joints, the filler wire grade SPT2 (Ti–Al–V–Zr system) (Table 3) was used as the filler material. The PT-3V titanium alloy and the filler wires SPT2 and 2V belong to the group of pseudo-α alloys. The chemical compositions of the SPT2 filler wire and the PT-3V titanium alloy are similar. It should be noted that a distinctive feature of the SPT2 wire is the presence of zirconium as an alloying element in its chemical composition. In titanium alloys, zirconium does not act as either an α-stabilizer or a β-stabilizer.

Table 4. Mechanical properties of welding filler wires 2V and SPT2 (GOST 27265–87)

Grade	Wire diameter, mm	Ultimate tensile strength (σ_t), MPa	Elongation (δ), %, not less than
2V	From 1.6 to 7.0	490–635	20.0
SPT2		645–845	13.0

Assembly of the components prior to welding was performed using a backing, which was manually tack-welded to the reverse side of the parts being joined. This backing forms the lower wall of the groove during the first pass [12, 13]. Welding of PT-3V titanium alloy specimens 45 mm thick in a narrow gap using a tungsten electrode with a magnetically controlled arc was carried out under the welding conditions given in Table 5. Macrosections of the welded joints are shown in Figure 1.

The macrostructure of welds produced by NGW using 2V and SPT2 filler wires is similar. The height of the deposited layer per single pass is 5 mm, and the weld width for the first and subsequent passes is 11.2–11.6 mm. Based on these geometric parameters of the weld macrostructure, the contribution of filler metal to the weld metal is 89–91 %.

The applied filler wires, under the selected NGW parameters for the PT-3V titanium alloy, ensure high-quality formation of a concave weld bead surface. No porosity or lack of fusion was detected in the weld metal.

Table 5. Welding parameters for NGW of PT-3V titanium alloy using a tungsten electrode with an externally controlled magnetic field

Welding speed (V_w), m/h	Arc voltage, V	Welding current (I_w), A	Filler wire feed rate, m/h	Shielding gas flow rate, l/min
8	12–13	420–440	55–65	30

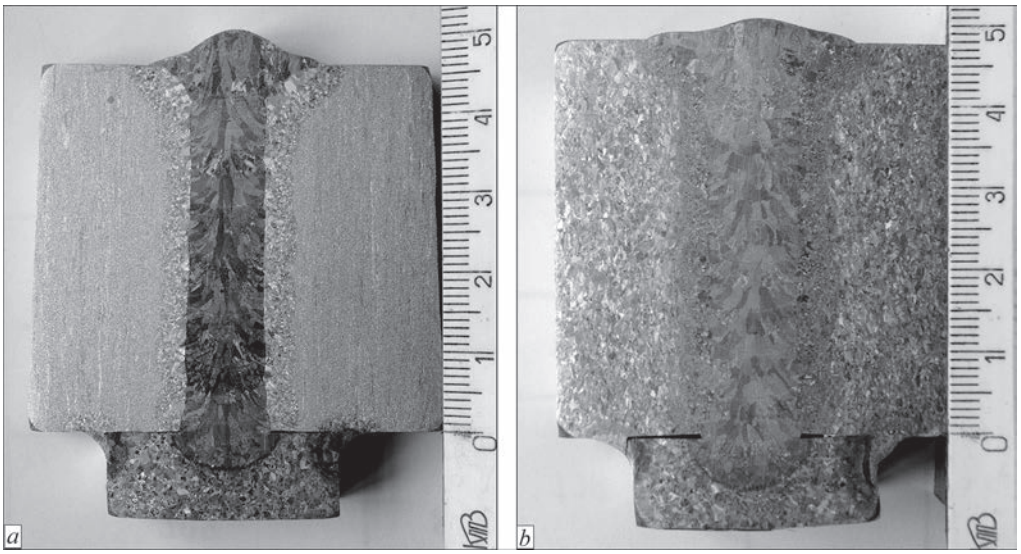

Figure 1. Transverse macrosections of welded joints of 45-mm-thick PT-3V titanium alloy produced by NGW: *a* — using SPT2 filler wire; *b* — using 2V filler wire

During NGW, no more than 11 % of the base metal enters the weld pool. Determining the chemical composition of the base metal and the weld metal produced by NGW using 2V and SPT2 filler wires showed that the weld metal made with filler wire 2V contains the lowest amount of alloying elements (Table 6). When using SPT2 filler wire, the aluminium content in the weld metal is lower compared with the base metal.

INVESTIGATION OF THE MICROSTRUCTURE OF PT-3V TITANIUM ALLOY WELDED JOINTS PRODUCED BY NGW

The microstructure of the base metal of the PT-3V alloy is shown in Figure 2. The base metal structure consists of equiaxed primary β-grains of various sizes, bordered by a continuous or discontinuous α-phase fringe (Figure 2, *a*) up to 15 μm thick. The intragranular structure consists of lamellar α-phase plates up to 1.5 μm thick. The lamellar α-phase structure contains fine parallel boundaries (Figure 2, *b*). Small amounts of β-phase may be present between the α-lamellae, although it is not always detectable by optical microscope.

Thus, the base metal contains predominantly α-phase with residual β-phase stabilized by vanadium. The relatively high density of intersecting lamellar structures indicates good plasticity and deformation capability of the alloy.

The microstructure of the weld metal of the PT-3V alloy produced by NGW using SPT2 filler wire — shown in the middle section of the weld in Figure 3 — consists of equiaxed primary β-grains formed at temperatures in the β-region (Figure 3, *a*, *b*). The boundaries of the primary grains are bordered by a continuous or discontinuous α-fringe up to 15 μm thick. The microstructure inside the primary grains is of the lamellar type. The α-phase plates are grouped into colonies, and within each colony the α-lamellae are parallel (Figure 3, *c*, *d*).

The microstructure of the weld reinforcement area (upper part of the weld) of the PT-3V alloy welded by NGW with SPT2 filler wire does not differ from the microstructure of the rest of the weld (Figure 4, *a*, *b*). The weld metal microstructure also consists of equiaxed primary β-grains. Inside the primary grains, the microstructure is lamellar, with α-phase plates forming colonies in which the lamellae are parallel.

The microstructure of the weld metal of the PT-3V alloy produced by NGW using the 2V filler wire in its central region is shown in Figure 5. The weld metal contains equiaxed and elongated primary grains of various sizes, within which thin packets of lamellar α-phase are located, with clearly defined grain boundaries. Despite the differences in configuration and size of the primary grains, the intragranular microstructure of the weld metal produced by NGW with the 2V filler wire, which is lamellar in nature, is very similar

Table 6. Chemical composition of the base metal and weld metal of PT-3V alloy produced by NGW using 2V and SPT2 filler wires, wt.%

Specimen type	Ti	Al	V	Zr	Cr	Si	Mo	Fe
Base metal	Balance	3.95	2.14	0.05	0.01	0.01	–	0.08
Weld metal, SPT2 filler		3.87	3.0	1.5			0.07	0.04
Weld metal, 2V filler		2.58	1.70	0.03			–	

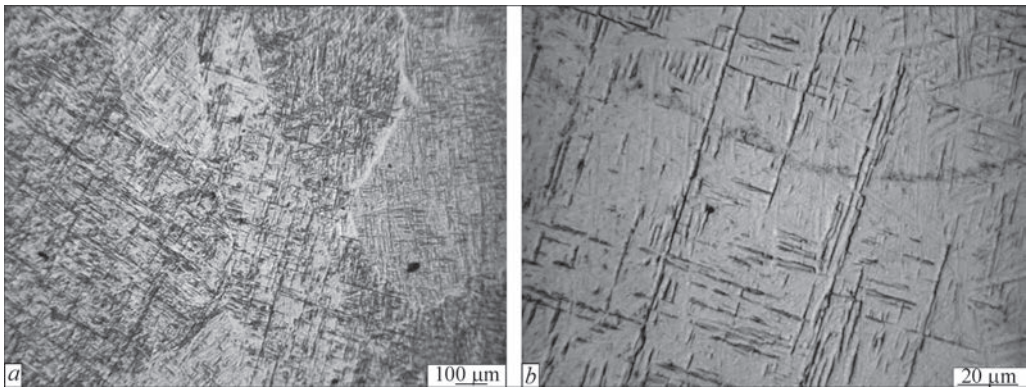

Figure 2. Microstructure of the base metal of PT-3V titanium alloy: *a* — ×50; *b* — ×100

to the microstructure of the base metal (Figure 5, *a*, *b*). The weld metal also contains α-lamellae with different growth orientations, indicating complex orientation relationships and heterogeneity in the formation of the α-phase. In certain regions, fine-dispersed α-structures are observed, which may have formed as a result of additional undercooling.

The microstructure of the metal in the fusion zone of the PT-3V alloy welded joint, produced by NGW using SPT2 filler wire, is shown in Figure 6. In the fu-

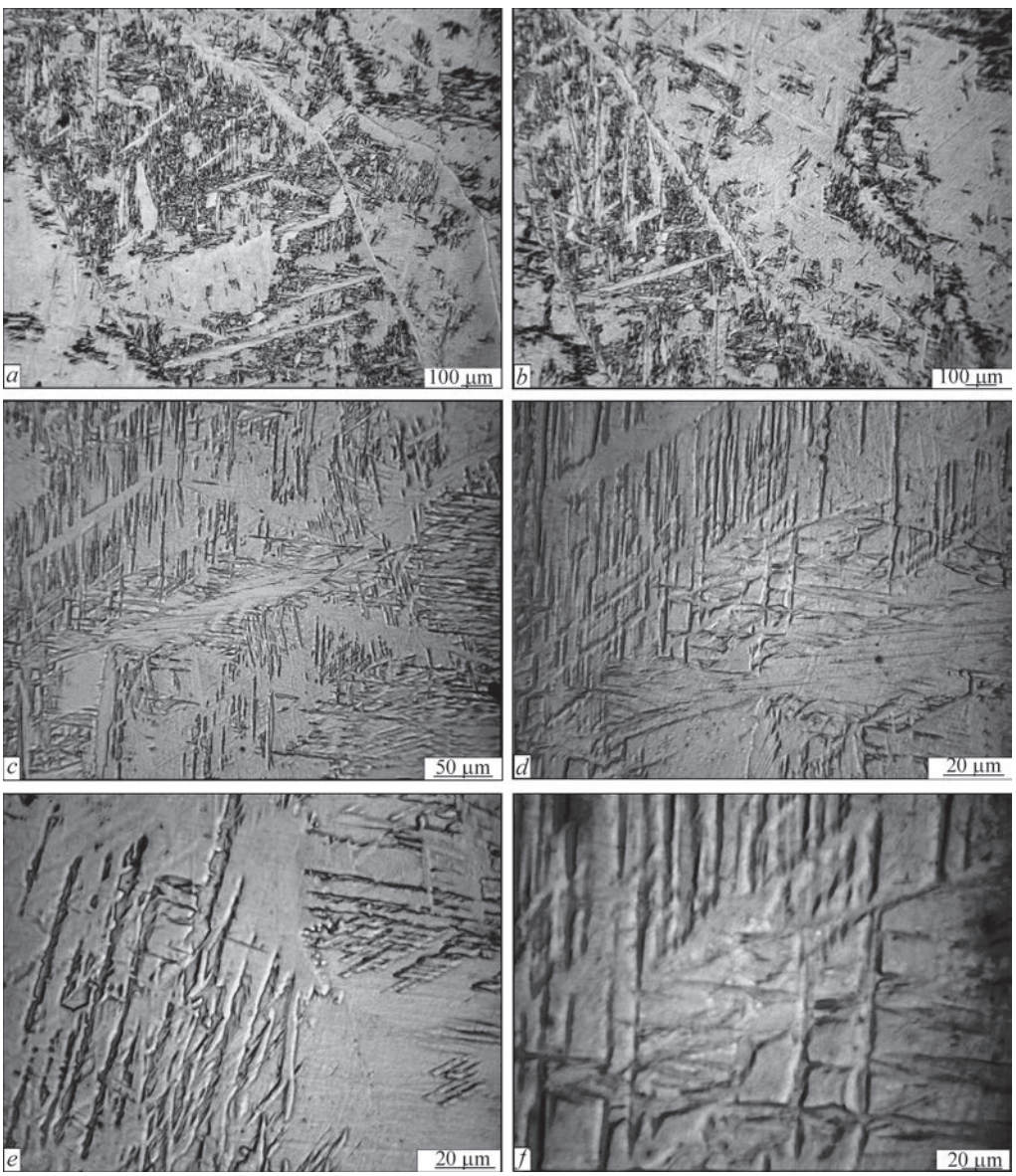

Figure 3. Microstructure of the weld metal of PT-3V titanium alloy produced by NGW using the SPT2 filler wire

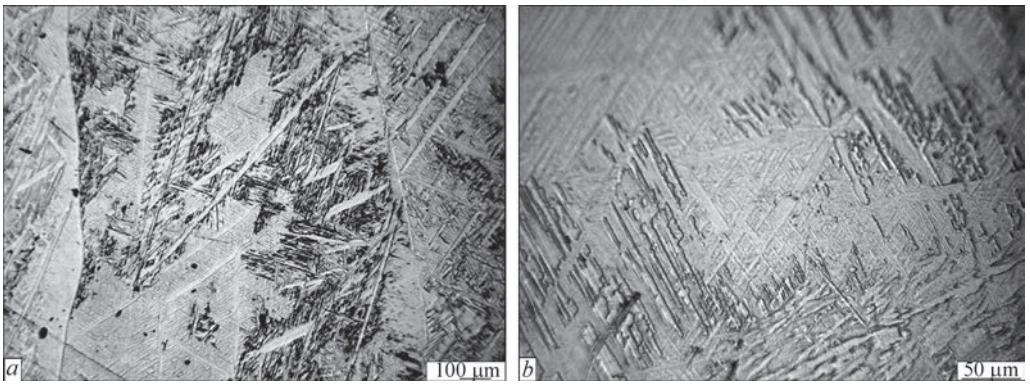

Figure 4. Microstructure of the weld metal in the upper part of the weld of PT-3V titanium alloy produced by NGW using the SPT2 filler wire

sion zone, the formation of fine primary grains is observed (Figure 6, *a*), while the intragranular structure resembles that of the base metal. The microstructure of the fine primary grains is lamellar, consisting of α-phase forming lamellae that can be either parallel or intersect within the former β-grains, which is typical for pseudo-α structures (Figure 6, *b*). This morphology indicates a relatively high cooling rate in this area during welding.

The microstructure of the metal in the fusion zone of the PT-3V alloy welded joint, produced by NGW using 2V filler wire, is shown in Figure 7. Fine primary grains are observed in the fusion zone (Figure 7, *a*), while the intragranular structure resembles that of the base metal (Figure 7, *b*).

The microstructure of the HAZ metal produced using SPT2 and 2V wires, immediately adjacent to the fusion zone — specifically, the large-grain area of the PT-3V alloy — is identical and is shown in Figure 8. The metal in this zone consists of equiaxed primary grains (Figure 8, *a*) with a microstructure similar to the intragranular structure of the weld metal grain (Figure 8, *b*, *c*). The structure contains coarse grains and elongated α-plates, predominantly oriented parallel to the heat gradient (Figure 8, b). A redistributed α-structure is noticeable in the form of loosely ordered overlapping packets. The boundaries of primary β-grains, partially transformed into α-phase, are occasionally observed.

In Figure 8, *d*, dispersed second-phase particles, most likely β-phase, can be seen along the α-plate boundaries. The size of these particles is 0.5 μm or smaller (Figure 8, *d*). The microstructure of the HAZ metal near the base metal (Figure 8, *d*, *e*) is also very

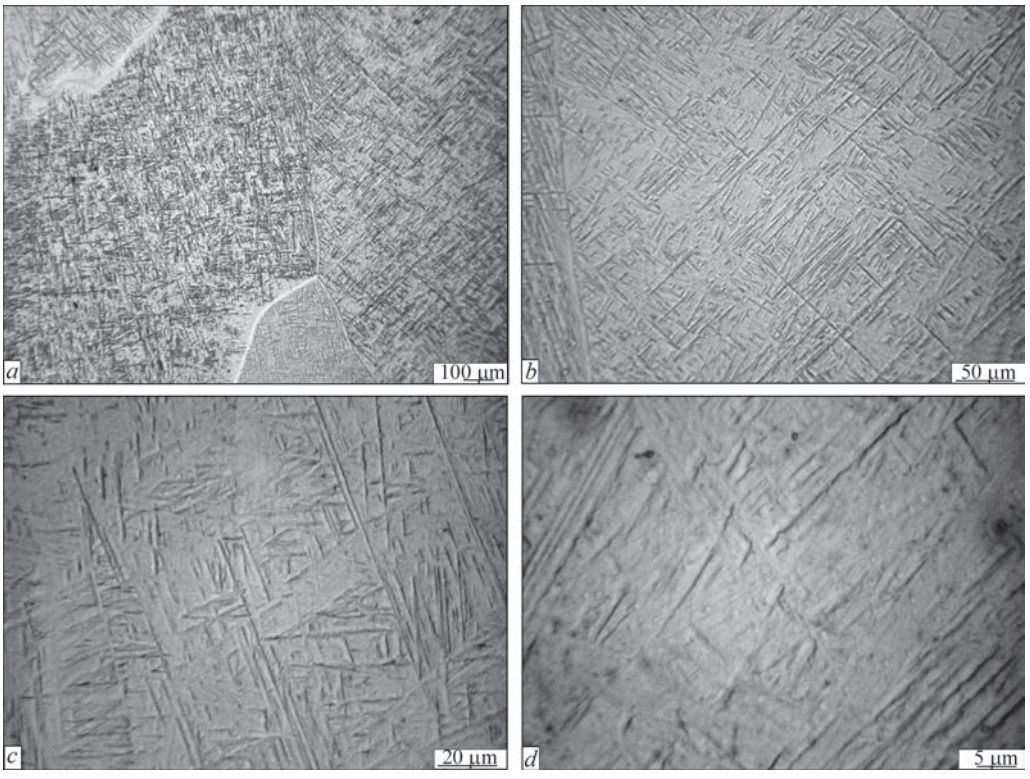

Figure 5. Microstructure of the weld metal of the PT-3V titanium alloy, produced by NGW using 2V filler wire

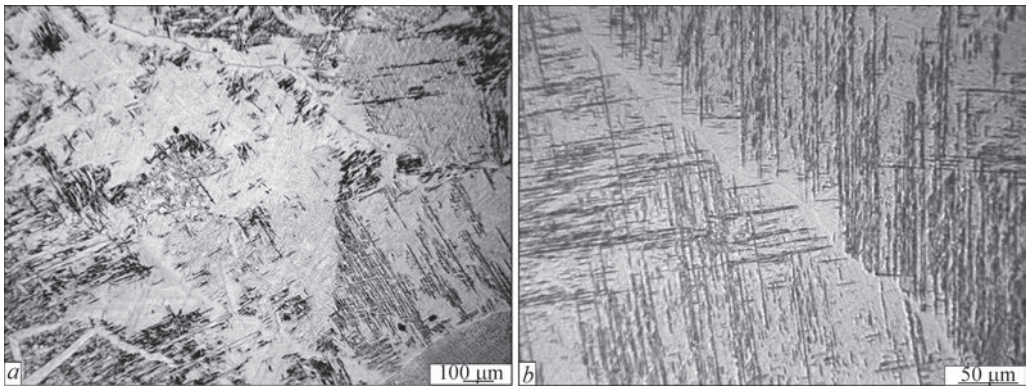

Figure 6. Microstructure of the fusion zone metal of the PT-3V titanium alloy, produced by NGW using SPT2 filler wire

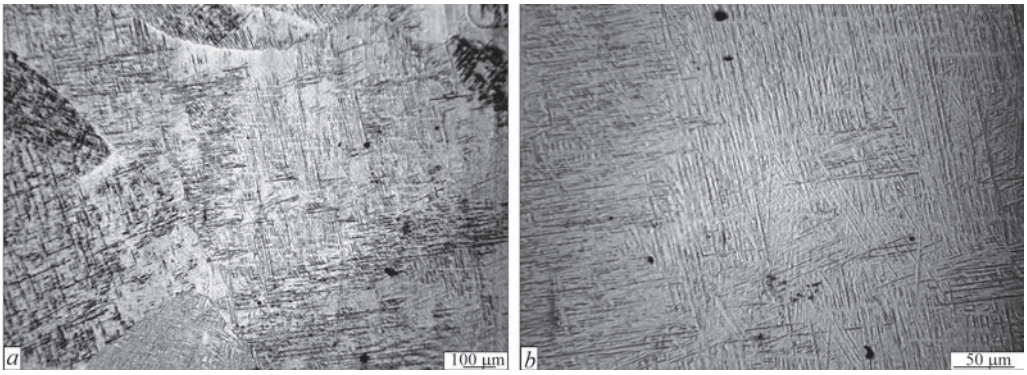

Figure 7. Microstructure of the fusion zone metal of the PT-3V titanium alloy, produced by NGW using 2V filler wire

similar to other areas of the PT-3V alloy welded joint produced by NGW with 2V filler wire.

Thus, the microstructures of the weld metal in PT-3V alloy joints produced by arc welding with SPT2 and 2V filler wires are similar. The similarity of microstructures in different areas of PT-3V welded joints may indicate a close phase composition, which provides several advantages for these filler materials belonging to the pseudo-α alloy class. Specifically, these alloys are practically insensitive to strengthening heat treatment. The martensitic α′-phase formed upon cooling from above the critical temperature has physical and mechanical properties similar to those of the α-phase. Moreover, the amount of β-phase in alloys of this class is so small that its eutectoid decomposition, if it occurs, does not significantly affect the physical and mechanical properties. Thanks to these characteristics, the 2V and SPT2 filler metals exhibit excellent weldability, typical of pseudo-α alloys, and high thermal stability.

DISCUSSION OF RESULTS

Determination of the mechanical properties of welded joints of the new pseudo-α titanium alloy PT-3V, produced by NGW with SPT2 and 2V filler wires, led to the conclusion that the lowest postweld strength values were observed in joints made with 2V filler wire, at 643 MPa (Table 7), which corresponds to 86 % of the base metal strength.

The highest postweld strength values were observed in joints made by NGW with SPT2 filler wire, at 759 MPa (Table 7). The strength of joints produced using SPT2 filler wire is comparable to the strength of the base metal (Table 7). It should be noted that the weld metal strength is somewhat higher, reaching 818 MPa, or 109 % relative to the base metal strength. Failure of the MI-12 specimens during testing of the welded joints occurred through the weld when 2V filler wire was used, and through the base metal when SPT2 filler wire was used. Thus, the weld metal of joints produced with SPT2 filler wire exhibits slightly higher strength — about 9 % greater than the base metal — immediately after welding.

The impact toughness values of the notched welded joint specimens produced with 2V filler wire exceed those of the base metal. This is due to the lower content of alloying elements in the weld metal, which consists of approximately 90 % filler metal from the 2V wire. The impact toughness values of welded joints produced with SPT2 filler wire are about 83 % of the base metal and correspond to the impact toughness values of the weld metal. The conducted studies allow the conclusion that using SPT2 filler wire for NGW of PT-3V titanium alloy enables the formation of a weld metal structure similar to that of the base metal and ensures comparable strength of the welded joint. For a comparative assessment of the performance of

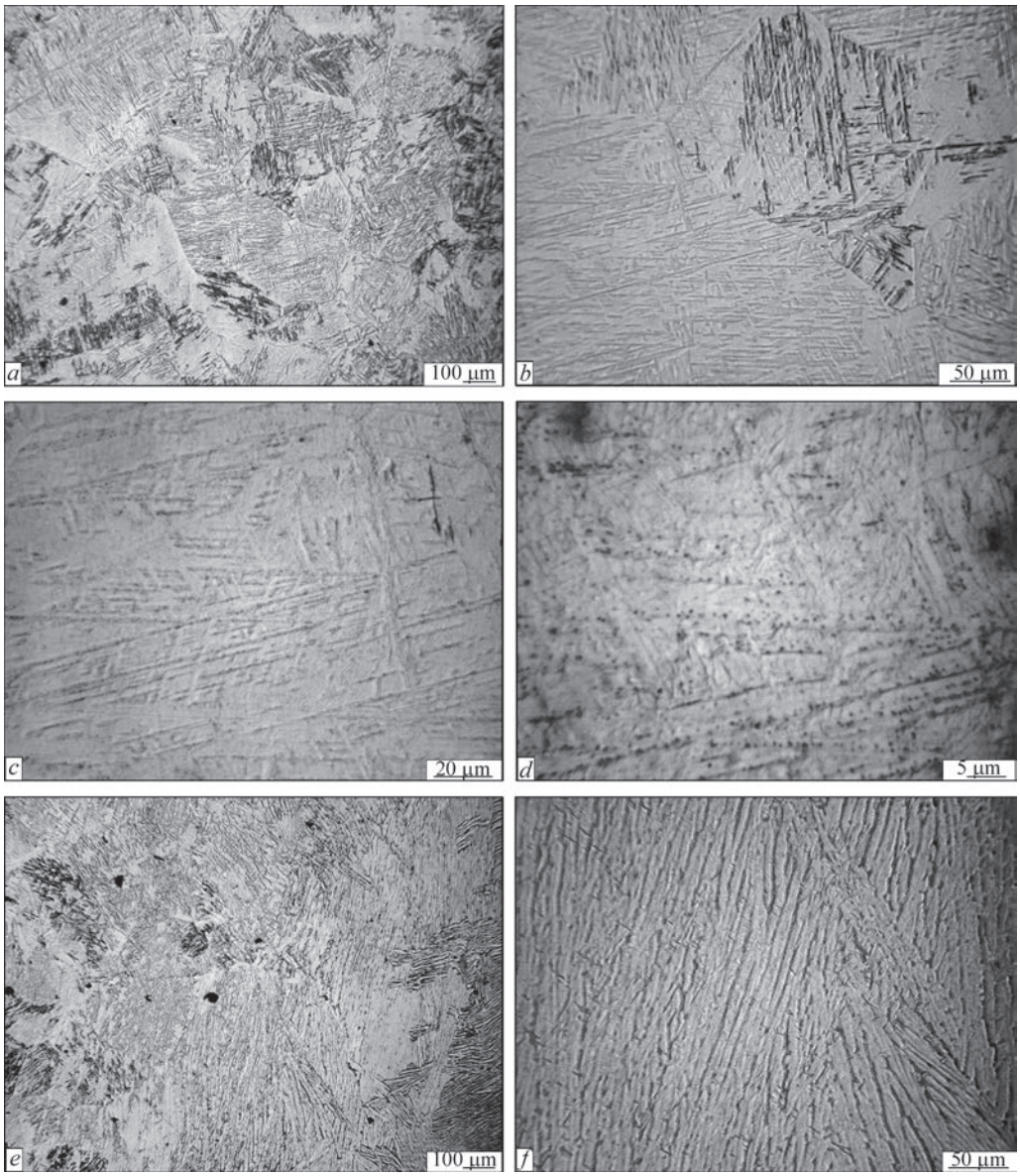

Figure 8. Microstructure of the HAZ metal of the PT-3V alloy, produced by NGW

welded joints produced with SPT2 and 2V filler wires, further studies on low-cycle fatigue strength are required. It should be noted that when using 2V filler wire, the strength of the welded joints is slightly lower than that of the PT-3V base metal. However, during arc welding of titanium alloys, the weld metal is also alloyed through the transfer of elements from the base metal into the weld. This allows the use of filler wire less alloyed than the base metal. High performance of welded joints in thick titanium alloys can be ensured due to the high ductility and impact toughness of the weld metal.

Table 7. Mechanical properties of the base metal and welded joints with a thickness of 45 mm made of PT-3V titanium alloy, welded by EBW*

Specimen	σ_t	σ_{02}	δ,%	ψ, %	*KCV*, J/cm²	
	MPa				Weld	HAZ
Base metal PT-3V, δ = 45 mm	747	678	12.7	30.8	95.3	
Welded joint, filler metal 2V	643	604		41.2	107	78
Weld metal, filler metal 2V	609	506	18.3	47.4	107	
Welded joint, filler metal SPT2	759	691	12.1	30.1	79	77
Weld metal, filler metal SPT2	818	716	11.8	36.9	79	
Weld metal, filler metal 2V after heating at 780 °C	799	750	10.7	45.1	89.2	

*Average of three results is given.

To increase the strength of PT-3V alloy welded joints when using 2V filler wire, postweld annealing can be applied. Annealing at 780 °C followed by furnace cooling allows the weld metal strength to rise to 799 MPa, with an impact toughness of KCV = 89 cm² (see Table 7). However, practical application of annealing is not always feasible for welded joints of thick titanium alloys.

Thus, the use of SPT2 filler wire for NGW of PT-3V titanium alloy with a magnetically controlled arc ensures that the welded joint achieves strength comparable to the base metal immediately after welding.

CONCLUSIONS

1. Filler wires 2V and SPT2, when used for NGW of PT-3V titanium alloy with a magnetically controlled arc, ensure sound formation of the concave weld bead surface. The strength of welded joints made with 2V filler wire is 643 MPa, which is 86 % of the base metal strength.

2. The microstructure of the weld metal in PT-3V alloy joints produced by NGW with SPT2 and 2V filler wires is similar and consists of equiaxed and non-equiaxed primary β-grains. The microstructure within the primary grains is lamellar α-phase. The similarity of microstructures in different areas of the welded joints of PT-3V alloy indicates a close phase composition.

3. The use of SPT2 filler wire for NGW of PT-3V titanium alloy allows the formation of a weld metal structure similar to that of the base metal and ensures comparable strength of the welded joint immediately after welding.

REFERENCES

1. Hori, K., Heneda, M. (1999) Narrow gap arc welding. *J. of the JWC*, **3**, 41–62.
2. Jae-Ho Jun, Sung-Ryul Kim, Sang-Myung Cho (2016) A study on productivity improvement in narrow gap TIG welding. *J. of Welding and Joining*, 34 (**1**), 68–74. DOI: https://doi.org/10.5781/JWJ.2016.34.1.68
3. Gaurav Dak, Navneet Khanna, Chandan Pandey (2023) Study on narrow gap welding of martensitic grade P92 and austenitic grade AISI 304L SS steel for ultra-supercritical power plant application. *Archiv. Civ. Mech. Eng*., 23(**14**), DOI: https://doi.org/10.1007/s43452-022-00540-3
4. Fang, N., Guo, E., Huang, R. et al. (2021) Effect of welding heat input on microstructure and properties of TC4 titanium alloy ultra-narrow gap welded joint by laser welding with filler wire. *Materials Research Express*, 8(**1**), 016511. DOI: http://dx.doi.org/10.1088/2053-1591/abd4b3
5. Akhonin, S.V., Belous, V.Yu., Romanyuk, V.S. et al. (2010) Narrow-gap welding of up to 110 mm thick high-strength titanium alloys. *The Paton Welding J*., **5**, 34–38. https://patonpublishinghouse.com/eng/journals/as/2010/05/07
6. Dong, Z., Tian, Y., Zhang, L. et al. (2024) Research status of high efficiency deep penetration welding of medium-thick plate titanium alloy: A review. *Defence Technology*, **45**, March, 178–202. DOI: https://doi.org/10.1016/j.dt.2024.08.004
7. Fang, D.S. (2017) *Study on the characteristics of three-wire indirect arc and its thick-wall narrow gap welding process under gas protection*: Ph.D. Thesis, Dalian University of Technology, Dalian, China.
8. Akhonin, S.V., Bilous, V.Yu., Selin, R.V. et al. (2023) Narrow-gap TIG welding of thick steel 20. *The Paton Welding J*., **6**, 21–26. https://doi.org/10.37434/as2023.06.04
9. Ding, L., Qin, B., Ge, K. et al. (2023) Microstructures and mechanical properties of thick Ti–6Al–3Nb–2Zr–1Mo joint by magnetron-controlled narrow gap TIG welding. *Metals and Materials Inter*., 29(**8**), 2304–2315. DOI: http://dx.doi.org/10.1007/s12540-02-01367-6
10. Wan, L., Huang, Y., Lv, S. et al. (2016) Narrow-gap tungsten inert gas welding of 78-mm-thick Ti–6Al–4V alloy. *Materials Sci. and Technology*, 32(**15**), 1545–1552. DOI: https://doi.org/10.1080/02670836.2015.1131941
11. Xinyu Bao Yonglin Ma, Shuqing Xing, Yongzhen Liu, Weiwei Shi (2022) Effects of pulsed magnetic field melt treatment on grain refinement of Al–Si–Mg–Cu–Ni alloy direct-chill casting billet. *Metals*, 12(**7**), 1080. DOI: https://doi.org/10.3390/met12071080
12. Belous, V.Yu., Akhonin, S.V. (2011) Formation of narrow-gap welded joints on titanium using the controlling magnetic field. *The Paton Welding J*., **4**, 19–23. https://patonpublishinghouse.com/eng/journals/as/2011/04/04
13. Yujun Hu, Hongjin Zhao, Xuede Yu et al. (2022) Research progress of magnetic field regulated mechanical property of solid metal materials, *Metals*, 12, 1988. DOI: https://doi.org/10.3390/met12111988

ORCID

S.V. Akhonin: 0000-0002-7746-2946,
V.Yu. Bilous: 0000-0002-0082-8030,
R.V. Selin: 0000-0002-2990-1131

CONFLICT OF INTEREST

The Authors declare no conflict of interest

CORRESPONDING AUTHOR

S.V. Akhonin
E.O. Paton Electric Welding Institute of the NASU
11 Kazymyr Malevych Str., 03150, Kyiv, Ukraine.
E-mail: akhonin.sv@gmail.com

SUGGESTED CITATION

S.V. Akhonin, V.Yu. Bilous, R.V. Selin (2025)
Structure and properties of welded joints of PT-3V titanium alloy produced by narrow-gap welding.
The Paton Welding J., **12**, 3–10.
DOI: https://doi.org/10.37434/tpwj2025.12.01

JOURNAL HOME PAGE

https://patonpublishinghouse.com/eng/journals/tpwj

Received: 10.07.2025
Received in revised form: 17.07.2025
Accepted: 18.12.2025

DOI: https://doi.org/10.37434/tpwj2025.12.02

APPROACHES TO ENHANCING THE BALLISTIC PERFORMANCE OF WELDED JOINTS IN HIGH AND ULTRA-HIGH HARDNESS ARMOR STEELS (REVIEW)

O.A. Slyvinskyy, M.M. Kovtoniuk

National Technical University of Ukraine "Igor Sikorsky Kyiv Polytechnic Institute"
37 Prosp. Beresteiskyi, 03056, Kyiv, Ukraine

ABSTRACT

The paper is devoted to the analysis of modern approaches to improving the bullet resistance of welded joints of high and ultra-high hardness armor steels. Based on the analysis of actual chemical composition of foreign-produced armor steel heats, the average content of key alloying elements influencing the structural and phase transformations under welding thermal cycles has been determined. In order to reduce the level of structural and mechanical heterogeneity of the metal of the welding heat-affected zone (HAZ) during the manufacture of welded assembly units of armored vehicle hulls from foreign-made steels, the content of Ni, Cr, Mo, B, as well as Si and V (in the case of alloying steel with them) should be the object of in-coming quality control, for which the minimum lower limit of the content of alloying elements in them should be determined through additional research. The current state of welding-metallurgical approaches for improving the ballistic resistance of armor steels is examined. These methods involve differentiating the mechanical properties of welds through the combination of welding, hardfacing, and auxiliary materials, or through the regulation of their structural and phase composition using advanced filler metals and combined or hybrid welding technologies. Literature data on the compositions of primary welding materials used for deposition of ballistic-resistant layers by hardfacing are provided. Particular attention is given to the potential of plasma powder hardfacing (PPH) for local reinforcement of weld metal and HAZ, ensuring controlled heat input and minimal mixing between base and filler metals. The advantages and limitations of PPH are summarized, and key directions for further research are outlined to facilitate the successful implementation of this technique for enhancing the ballistic performance of welds of high and ultra-high hardness armor steels.

KEYWORDS: welded joints, high and ultra-high hardness armor steels, bullet resistance, hardfacing, plasma-powder hardfacing

INTRODUCTION

Rolled sheets from armor steels are widely used in welding production of military vehicle hulls with the level of protection from small arms bullets and small caliber shells. The main characteristic determining the serviceability of these materials for their intended purpose, is ballistic performance, i.e. resistance to kinetic ammunition penetration (bullet resistance, respectively, in the case of antibullet protection of a military equipment object). In its turn, ballistic resistance as a type of the steel resistance to shape change and destruction under the conditions of high-speed impact loading is directly connected with the steel physical and mechanical properties.

The main mechanical characteristic, determining the ability of the material to resist penetration of another body, is its hardness. With increase of hardness which is proportional to the ultimate strength, the ballistic resistance of steels designed for armor protection, also rises [1]. High values of hardness and strength of rolled steel are the necessary conditions for preservation of its ballistic resistance, but the requirements to its characteristics are not limited to them. Under the conditions of pulsed impact loading a transition of the striker kinetic energy into a shock wave occurs during its collision with the armored barrier. This, in its turn, generates a packet of compression and unloading waves with different intensity, resulting from the process of high-speed energy exchange on the contact and reverse surfaces of the barrier, as well as on the interfaces of phases and structural components. Moreover, the pulsed impact loading may lead to considerable heating of the material, which will be accompanied by phase transformations and its transition into the state of hydrodynamic fluidity under the conditions of a nonuniform compression, as a result of which the fracture resistance will be determined not by material strength or hardness, but largely by its dynamic viscosity. By the data of [2] the ballistic resistance of steel armor, alongside its mechanical strength and hardness, is determined by its ability to deformation hardening, resistance to thermal softening, heat capacity, temperature dependence of yield stress, as well as the microstructural features and chemical composition.

The speed of striker interaction with the barrier during firing of small arms ammunition (bullets) is usually in the range of 600–900 m/s. However, the result of this interaction, alongside the dimensions, properties, structure and chemical composition of

Table 1. Typical mechanical properties of high- and ultra-high-hardness hot-rolled armor steels in the heat-treated state

Material	Hardness, *HBW*	Yield limit, $\sigma_{0.2}$, MPa	Ultimate strength, σ_t, MPa	Relative elongation after rupture δ_5, %	Impact energy KV_{-40}, J
High-hardness steel	480–540	≥ 1250	1450–1800	≥ 8	≥ 25
Ultrahigh-hardness steel	> 570	≥ 1300	≥ 2000	≥ 7	≥ 12

the barrier is also determined by the diameter, weight and material of the striker, its hardness, angle of incidence, shape of the head part, etc. Due to the multifactorial nature of the process, there is no unambiguous analytical dependence between the mechanical properties, which can be experimentally determined under the conditions of standard laboratory tests, and bullet resistance of armor material. Proceeding from empirical dependencies of armor steel resistance to penetration, established by the results of ballistic tests, hot-rolled steel designed for antibullet protection of military equipment, should have high hardness and strength, while preserving sufficient impact toughness and ductility (Table 1). Here in countries oriented toward military collaboration with NATO, the rolled steels for light armored vehicles is divided into armor steels of high and ultrahigh hardness, in keeping with the requirements specified in US DOD standards MIL-DTL-46100 "Armor Plate, Steel, Wrought, High-Hardness" and MIL-DTL-32332 "Armor Plate, Steel, Wrought, Ultra-High-Hardness", respectively.

The set of service properties of armor steels of high and ultra-high hardness is ensured by their alloying by Ni, Cr, Mo, V, Si, Mn and B, as well as by the technologies of out-of-furnace treatment during melting to provide high purity of the materials as to impurities and nonmetallic inclusions and of thermomechanical treatment to create maximal dispersion and homogeneity of the structure [1].

HETEROGENEITY OF THE MECHANICAL PROPERTIES OF ARMOR STEEL WELDED JOINTS. STATE OF THE PROBLEM

At present ensuring equivalent ballistic resistance of the welded joint metal, compared to the base metal, remains one of the key challenges in industrial production of welded assembly units from armor steels. The main problem consists in lowering the weld metal hardness and strength through application of welding materials, the chemical composition of which is selected primarily with the purpose of preventing cold cracks. The most widely used composition of such materials is the low-carbon high-alloy steel of austenitic class of 20 % Cr–10 % Ni–6 % Mn type. In its turn, the processes of full and partial austenitization, collective recrystallization, repeat hardening or high-temperature tempering in individual regions of the HAZ, which are due to the influence of the thermodeformational cycle of welding, have a significant impact on the service properties of the metal in this part of the joints [3, 4].

Figure 1 gives a typical result of testing a bullet-resistant welded joint in high-hardness armor steel with damage to the metal of the weld and HAZ.

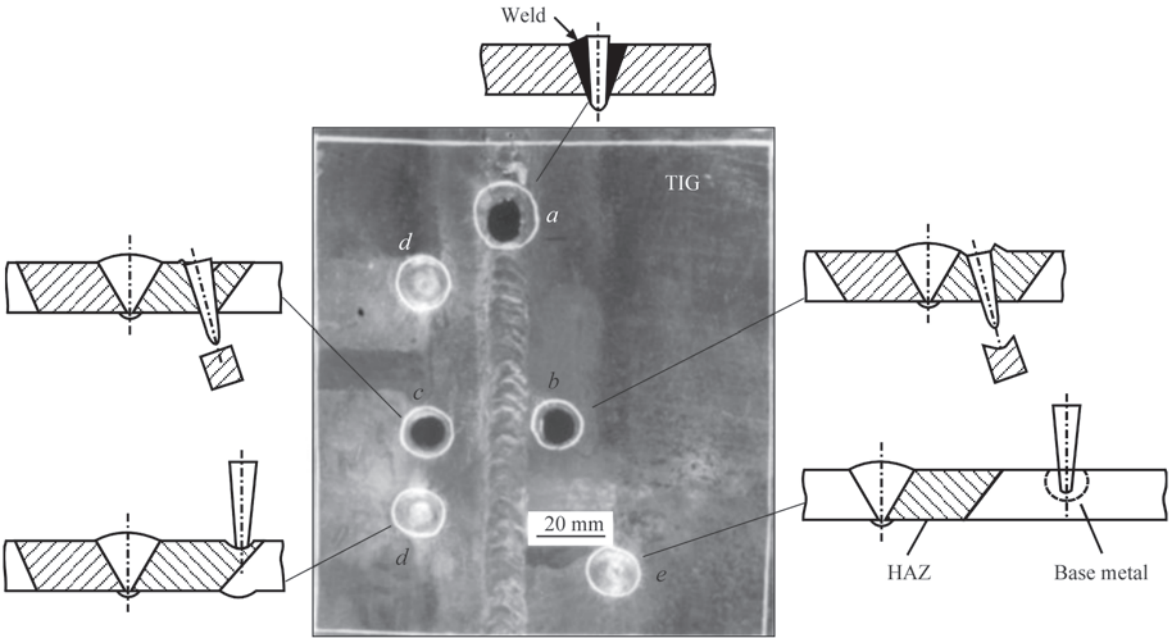

Figure 1. Results of ballistic testing of a welded joint of high-hardness armor steel [5]: *a* — piercing; *b* — plug knocking out; *c* — plug shearing; *d* — bulge; *e* — striker fragmentation

Based on the results of ballistic testing, according to the behaviour of the material of the target and the armor-piercing striker, we can single out five main mechanisms of their interaction [5]:

- puncture, which is accompanied by plastic expansion of the hole without striker deformation (Figure 1, *a*);
- plug knocking out — target material tearing out with signs of plastic deformation at the point of its interaction with the striker (Figure 1, *b*);
- plug shearing — target material tearing out without macroplastic deformation, striker deformation (Figure 1, *c*);
- formation of a bulge on the back side of the target, striker deformation or fragmentation (Figure 1, *d*);
- striker fragmentation with full preservation of target integrity (Figure 1, *e*).

On the whole, the nature of substandard damage to the weld and individual sections of the HAZ may differ from the one shown in Figure 1, depending on the multifactor mechanism of interaction of the means of destruction and the armor barrier. However, insufficient resistance of the metal of the weld and HAZ during high-velocity shock-wave loading, caused by bombardment by kinetic munitions, is a common problem when welding armor steels, and it is directly connected with the course of structural-phase transformations, which accompany welded joint formation. Influence of thermal cycles of welding on the structure and phase composition of the HAZ metal in quenched and tempered armor steels is quite well studied in [6–8]. Based on the results of these experiments the degree of degradation of the mechanical properties of welded steel, with other things being equal, in particular constant welding heat input, is determined by its chemical composition, namely content of elements, capable under the non-equilibrium conditions of phase transformations, to ensure austenite transformation at as high a temperature as possible in the high-temperature part of the HAZ, with the purpose of partial self-tempering of the newly formed martensite, and maximum possible deceleration of tempering of the initial structure in the HAZ low-temperature part.

Table 2 is a comparison of the requirements to the chemical composition of armor steels according to MIL-DTL-46100 and MIL-DTL-32332 with the declared (according to the manufacturer) maximal content of elements in the foreign-made steels of high (Armox 500T) and ultra-high (Mars 600) hardness widely used in local production of armored vehicles. One can see from the above that in contrast to domestic practice, when the respective regulatory documents clearly indicate the steel alloying limits, the content of elements, critically important for the set of properties of armor steels, in particular C, Mn, Si, Ni, Cr, Mo, V, B, in this case is either not regulated at all, or just the upper alloying limit is indicated.

Table 3 gives a comparison of the declared by the manufacturer maximum content of the main alloying elements for a number of foreign-made armor steels with average content based on the results of chemical analysis of the heats.

Table 2. Regulated chemical composition of high- and ultra-high-hardness armor steels, wt.%

Chemical element	Maximum permissible value acc. to MIL-DTL-46100	Armox 500 (maximal content by manufacturer's specification)	Maximum permissible value acc. to MIL-DTL-32332	Mars 600 (maximal content by manufacturer's specification)
Carbon	0.32	0.32	0.55	0.45
Manganese	Not limited	1.2	Not limited	1.0
Phosphorus	0.02	0.015	0.02	0.01
Sulphur	0.01	0.01	0.01	0.002
Silicon	Not limited	0.4	Not limited	1.0
Nickel		1.81		2.4
Chromium		1.01		0.5
Molybdenum		0.7		0.5
Vanadium		–		–
Niobium	–	–	Not limited	–
Boron	0.003	0.005	0.003	0.003
Copper	0.25	–	0.75	–
Nitrogen	0.03	–	0.03	–
Titanium	0.1	–	0.1	–
Zirconium	0.1	–	0.1	–
Aluminium	0.1	–	0.1	–
Lead	0.01	–	–	–
Tin	0.02	–	–	–
Antimony	0.02	–	–	–
Arsenic	0.02	–	–	–

Table 3. Maximum and average content of the main elements in foreign-made armor steels based on chemical analysis of the melts

Steel	C		Mn		Si		Ni		Cr		Mo		Number of melts
	Max.	Av.	Max.	Av.	Max.	Av.	Max.	Av.	Max.	Av.	Max.	Av.	
Quardian 500	0.30	0.26	1.2	0.80	0.4	0.21	1.2	0.83	0.8	0.44	0.6	0.29	16
Armstal 500	0.32	0.30	1.2	1.0	0.5	0.23	1.1	1.21	0.9	0.86	0.3	0.26	10
Miilux Protection 500	0.30	0.27	1.7	1.1	0.7	0.35	0.8	0.19	1.5	0.41	0.5	0.10	42
Armox 500T	0.32	0.28	1.2	0.85	0.4	0.26	1.8	0.90	1.0	0.50	0.7	0.35	17
Swebor Armor 560	0.36	0.34	1.6	1.3	0.6	0.25	–	0.05	–	0.43	–	0.02	12
Mars 600	0.45	0.44	1.0	0.49	1.0	0.79	2.4	1.90	0.5	0.15	0.5	0.33	12
Armox 600T	0.47	0.40	1.0	0.66	0.7	0.24	3.0	1.98	1.5	0.46	0.7	0.33	12

Despite the complete correspondence of rolled sheets from the steels given in Table 3 to the required level of ballistic protection, it is exactly the significantly lower content of alloying elements (compared to the declared maximum) which may lead to formation of extended sections of the HAZ with a low level of strength and/or impact toughness in the welded joints [6, 8] and which can have a negative effect on their bullet resistance. For instance, by the data of [6] increase in welding energy input from 0.5 to 0.9 kJ·mm^{-1} resulted in an increase in the extent of HAZ section "softened" (in relation to base metal hardness) 2.9 times for Miilux Protection 500 steel and just 1.5 times for alloyed steel of 30Kh2N2MF type. Under the conditions of exposure to identical welding thermal cycles, the hardness of the high-temperature tempering section of the HAZ in Miilux Protection 500 steel decreased ~2 times, while its structure consisted predominantly of granular bainite (Figure 2, *a*). For steel of 30Kh2N2MF type metal hardness of a similar HAZ section with the formed structure of troostite with different degree of dispersion was reduced ~1.65 times (Figure 2, *b*).

The authors [6] explain the different level of structural-mechanical heterogeneity of the welded samples by that an increased content of Si, Cr, Mo in the steel of 30Kh2N2MF type and its additional alloying by V ensure a more significant inhibition of the processes of softening of the HAZ sections in it, which are heated to the temperatures of high-temperature tempering and partial austenitization during welding, than that in Miilux Protection 500 steel, which *de facto* was alloyed only with Mn and B, while the content of other elements (0.31 wt.% Si; 0.41 wt.% Cr; 0.08 wt.% Mo; 0.012 wt.% V) did not provide a sufficient influence on deceleration of tempering of its initial structure.

Thus, minimizing the extent of softened HAZ sections and degree of degradation of the mechanical properties of the metal in these sections, requires at the least a rational selection of the base metal, with a sufficient content of elements increasing the stability of overcooled austenite and slowing down its tempering, in particular, nickel, chromium, molybdenum, boron, as well as silicon and vanadium (in the case the steel is alloyed with them) [1, 6]. From the materials given in Table 3 this primarily concerns Miilux Protection and Swebor Armor steels. Additional research is needed to determine the minimum lower limit of alloying element content for the rolled stock from these materials applied in manufacture of welded armored vehicle hulls.

At present two approaches — design and metallurgical are used to ensure equivalent ballistic resistance of the metal of armor steel welded joints, compared to the base metal. In the first case, respective design of welded components of the military armored vehicle hulls is envisaged, with mounting of reinforcing armor lining on the reverse side of the weld or application of such joint types, where one of the parts completely covers the weld, by using tee-, overlap, tenon, and slot joints. A drawback of such solutions is greater metal content and weight of the structure, unsolved

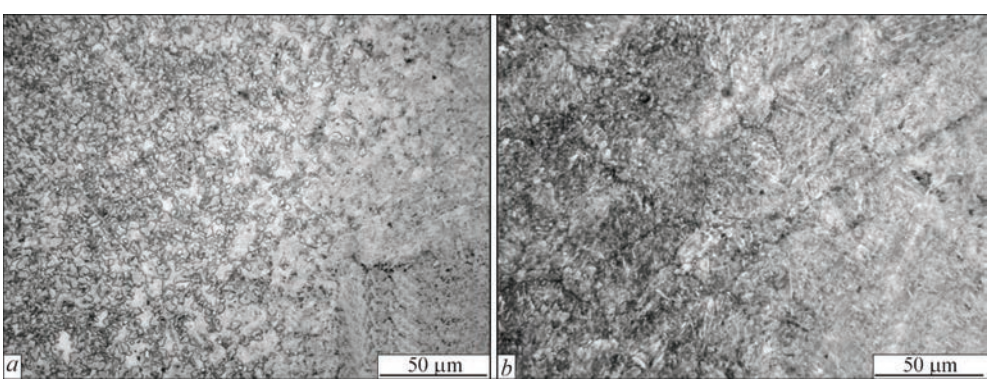

Figure 2. Microstructure of the transition zone between the incomplete recrystallization area (left) and tempering area (right) in welded samples of Miilux Protection 500 steel (*a*) and 30Kh2N2MF steel (*b*) at a welding energy input of 0.9 kJ·mm^{-1} [6]

problem of possible softening of the HAZ metal and the metal loosing the necessary bullet resistance.

The metallurgical approach envisages an increase in ballistic resistance of butt welded joints of armor steels by forming heterogeneous properties of the weld metal due to a combination of welding, hardfacing and auxiliary materials or regulation of their structural and phase composition by introducing advanced welding materials, combined and hybrid welding technologies.

FORMATION OF HETEROGENEOUS (COMBINED) PROPERTIES OF THE WELD METAL

A method of multipass welding with alternation of the applied welding materials and using plastic interlayers in the weld structure is known from the experience of cold cracking prevention in thick-walled welded joints of hardening steels. This approach was the base for a series of studies on creation of a heterogeneous weld structure with mechanical properties differentiated across the joint thickness. The authors of [9] proposed using 1–2 high-hardness layers 18 mm thick in the weld structure for coated electrode welding of armor steel butt joints. Here, the effect of enhancing the ballistic resistance of the combined weld metal is observed under the condition of formation of a hard interlayer inside across the weld thickness, between the root and filling (facing) passes, made with electrodes of austenitic class (Figure 3).

The role of a buffer interlayer deposited on the edges being joined before welding is emphasized. In the opinion of the authors of [9], this interlayer of a ductile high-alloyed steel of austenitic class not only promotes lowering of the risk of cold cracking during welding, but also prevents propagation of the shock waves through the HAZ metal due to inherent plastic flow in the direction opposite to striker penetration.

For the above welded joint type with a combined weld the optimal thickness of the hard layer of ~5.5 mm was established, which corresponds to ~0.3 of the base metal thickness, and the influence of the composition of reinforcing hardfacing materials on bullet resistance characteristics was compared [10].

Despite the available results, the question of the sequence of hardfacing in the structure of combined welds of armor steel welded joints remains open. In particular, in [11], by the results of comparison of two grades of flux-cored hardfacing wires and the sequence of the hard interlayer arrangement relative to the root and filling passes, made with austenitic electrode wire of G 23 12 L Si type, it was determined that the highest bullet resistance is ensured by the external location of the reinforcing layer from the firing

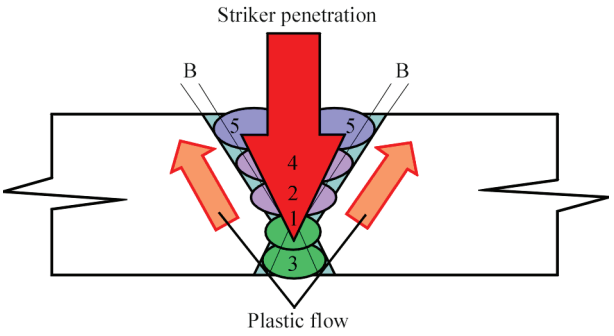

Figure 3. Schematic representation of the interaction of the combined weld with the high-speed striker [9]: B — buffer interlayer deposited on the butt edges; 1 — 6 — sequence of weld layer deposition (1, 3, 5, 6, B — austenitic (stainless) steel, 2, 4 — high-hardness wear-resistant material

side. Although no through-and-through penetration occurred in any of the cases (Figure 4, *c*, *d*), the external location of the hard interlayer allows scattering the impact energy over a larger cross-sectional area of the weld with a high ductility and toughness, capable of relaxing the generated stresses without brittle fracture. In the case of placing the hard interlayer inside the weld, the process of further deposition of facing layers leads to undesirable structural changes which contribute to a decrease in its hardness [11].

The technologies of enhancing the bullet resistance of butt welds in high-hardness armor steel, implemented in welding production of Soviet and domestic armored vehicles, also envisaged hardfacing with special coated electrode or gas-shielded flux-cored wire [12] from the external surface of the welded joints.

The chemical composition of welding materials for making combined welds with an enhanced ballistic resistance and hardness of the formed reinforcing interlayers, based on literature data, is given in Table 4.

Reference [17] is a study of the fundamental possibility of increasing the hardness of the facing layer of the weld by welding with standard chromium-nickel-manganese wire of austenitic class of G 18 8 Mn type in a mixture of 98 % Ar + 2 % CO_2 over a carbon fibre filler (CFF) based on a carbon-containing fabric of UUT-2 grade, placed into the gap between the edges being welded. During welding the electrode and filler carbon material melt forming a liquid pool. Alloying of the surface takes place due to the electrode wire, and CFF allows increasing the carbon content in the weld metal. With increase of CFF specific weight in the weld composition its structure becomes similar to that of high-chromium cast iron with extended precipitates of the cementite component and average microhardness of 380–395 $HV_{0.2}$.

For samples from Armox 500T steel the authors of [18] are studying the method of gas-shielded consumable electrode wire welding over a pre-applied layer

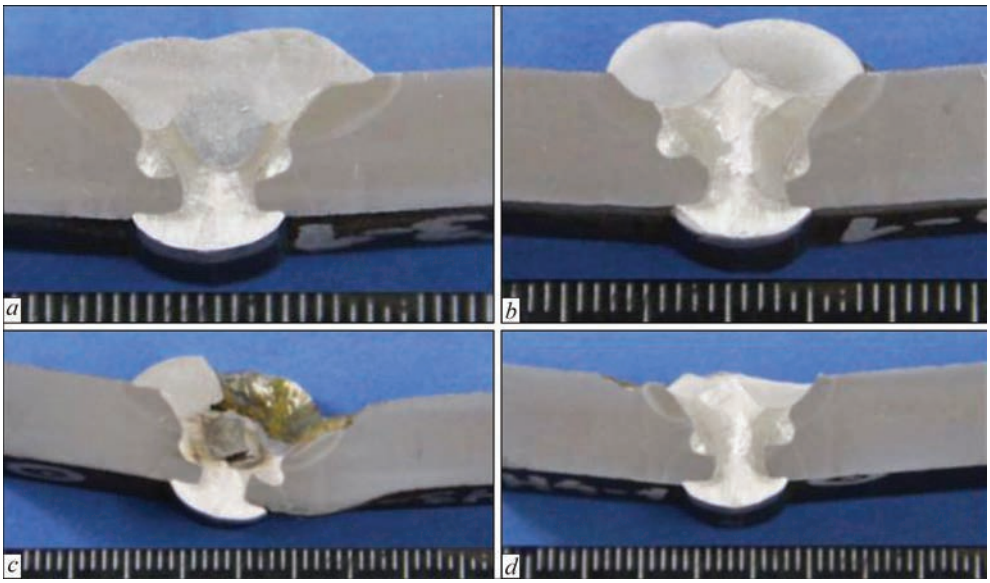

Figure 4. Appearance of a combined welds in butt welded joints of 8 mm Armox 500T steel before (*a*, *b*) and after (*c*, *d*) ballistic tests [11]: *a*, *c* — hard interlayer was made using EnDOtec. DO30 flux-cored wire inside the weld; *b, d* — hard interlayer was made using Durmat FD 739 flux-cored wire on the external surface of the weld

of flux-paste containing nanoparticles of WC, SiC and TiC carbides. Based on the research results, not only an increase in weld metal hardness to 578–654 *HV*, but also refining of its structure and increase in penetration depth through contraction of the arc column by tungsten and silicon ions were established.

REGULATION OF THE STRUCTURAL-PHASE COMPOSITION OF THE WELD METAL

In the contest of welding armor steels, in this research area a search for new promising welding materials with high values of deposited metal strength under the condition of preservation of its crack resistance is performed, as well as introduction of welding methods with the possibility of independently influencing the process productivity indices (penetration depth, welding speed) and consumption of welding materials and their proportion in the weld metal, respectively.

The authors of [19] proved the possibility of formation of the structure of carbide-free bainite in the weld metal of a butt joint in high-hardness armor steel made with an experimental coated electrode of the following composition (wt.%):

Fe – 0.3 C – 1.6 Si – 1.8 Mn – 1.2 Ni – 1.3 Co – –1.3 Cr – 0.25 Mo – 0.015 S – 0.015 P.

Structure of carbide-free bainite, consisting of lath-shaped crystals of the ferrite phase, and residual austenite, and contains no cementite particles, is characterized by high strength, hardness of ~450 *HV* and is not prone to cold cracking. However, the impact toughness values of the weld metal turned out to be somewhat lower than those of the base metal, because

Table 4. Chemical composition and hardness of the deposited layers of materials for the bullet-resistant layer, wt.%

Grade	C	Si	Mn	Cr	Ni	Mo	B	W	V	Nb	Co	Fe	Hardness *HB*	Source
AWS E FeCr–A7	4.0	1.5	1.0	30	–	2.0	–	–	0.5	–	–		~648	[9]
AWS E WC1 30/40	2.4	0.18	–	–	0.3	0.36	–	56.4	–	–	–		595–685	[10]
Durmat FD 739	1.0	–	–	20	–	3.3	4.4	5.7	–	3.4	–		830–900	[11]
Castolin EnDOTec DO*30	0.5	0.4	1.4	1.0	–	–	3.7	–	–	–	–	Bal.	745–850	[11]
AN-180 (15KhN2GM)	0.11–0.20	0.20–0.70	1.0–1.60	1.0–1.60	2.0–2.50	0.35–0.70	–	–	–	–	–		364–477	[12]
Chromium white cast iron	4.3	0.91	1.66	29.8	–	–	–	–	–	–	–		~655	[13]
WC-alloy	1.0	1.5	–	10.0	48	5.4	–	30 (WC)	0.5	–	–	3.5	~595	[14]
Stellite-6 (AWS A5.13 ERCoCr-A)	1.1	< 2.0	–	30	< 3.0	< 1.0	–	4.0–5.0	0.5	–	Bal.	< 3.0	~430	[15]
Castolin EnDOTec DO*390N	5.0	2.0	5.0	20	–	10	5.0	10	–	10	–	Bal.	~900	[16]

of precipitation of an austenite phase with coarse block morphology between the dendrite branches.

A promising direction of development of welding materials for hardening steels are such which allow realization of the effect of low-temperature transformation of austenite in the weld metal [20]. These are low-carbon alloyed welding consumables of Cr–Ni and Cr–Ni–Mn system, which ensure a delay in austenite decomposition to the temperature of 200 °C and lower. In this case, martensite transformation in the welded steel HAZ will occur under the same thermodeformational conditions, as during welding with austenitic materials and that is why welding is allowed to be performed without preheating. In its turn, the low-temperature transformation of austenite into low-carbon lath martensite in the weld metal gives it high strength with sufficient ductility and toughness in most cases. At present, however, the majority of publication devoted to the introduction of these materials for welding high-strength steels, is limited to structural steels with the yield limit of 690–960 MPa.

A certain increase in the values of strength and hardness of the metal of the weld made with standard low-carbon welding materials can be achieved in welding of armor steels containing 0.25–0.45 wt.% carbon by regulation of the weld dilution by the deposited metal. This is impossible for conventional methods of consumable electrode arc welding, as the feed rate of electrode wire is strictly tied to the welding current value, required to achieve certain penetration The methods of welding without filler or with the filler material feed rate independent of the energy parameters of the heat source, the hybrid and combined welding technologies allow influencing the structural and phase composition of the weld metal to a greater extent. There are successful examples of similar approaches to realization of the task of enhancing the strength of the weld metal of welded joints in high-hardness armor steels for hybrid plasma-arc welding [21].

It should be noted that practically all the above-given examples of the methods of enhancing the ballistic resistance of butt welded joints in armor steels are limited to the area of metallurgical reactions during welding, and they are capable of influencing the composition and properties of just the weld metal and the fusion zone. The influence on the softening processes outside the weld is mostly extensive in nature: limitation of welding energy input, application of concentrated welding heat sources with the purpose of maximal narrowing of the HAZ. A promising direction in solving the problem of heterogeneity of the working properties of the metal of armor steel welded joins can be application of the method of deposition of a hard bullet-resistant layer on the surface of the weld, and, if required, the HAZ, with minimal heat input into the welded joint metal, ability of separately controlling the processes of supplying energy and feeding the filler material, and a wide range of materials for the reinforcing coating.

PROSPECTS FOR PLASMA-POWDER HARDFACING

The PPH method allows precisely controlling the deposited layer thickness, ensures localized heat input, minimizing of the degree of mixing and high adhesion of the layer to the base [22]. This is achieved, in particular, due to the high degree of plasma arc ionization, which provides a concentrated thermal impact in a limited zone [23]. More over, feeding the powder filler materials together with the shielding gas directly into the arc zone, prevents its oxidation and allows

Table 5. PPH advantages and drawbacks [22, 26, 27]

Advantages	Drawbacks
High effectiveness of powder utilization (deposition > 95 %)	Requires a metal base for closing the electric circuit
Possibility of using inexpensive powders, resistance to changes in their quality	Limited used on surfaces with complex geometry (for instance, grooves, corners)
Formation of a continuous coating with minimal porosity	High heat input requiring additional cooling in case of hardfacing small parts
Single-pass deposition of thick layers, reducing the number of passes	Impossibility of stable deposition on vertical surfaces due to the influence of gravity
Strong metallurgical bond between the coating and the base	Mixing can change the properties of both the coating and the base material
Fine-grained microstructure of the deposited layer	Residual stresses in the coating, which may influence its durability
Melting zone protection by inert gas prevents metal oxidation during the process	Metallurgical compatibility of the coating material and the substrate should be taken into account
Possibility of forming the alloys directly in the molten pool, including metal composites	
Minimal penetration depth	

producing high-quality coatings clean from the metallurgical viewpoint [24].

As with any other thermal methods of surface engineering, under PPH conditions a heat-affected zone and a region of the coating mixing with the base metal are formed, the processes in which have a significant influence on the treated product performance. However, the degree of mixing for the layers of more than 1 mm thickness, deposited by PPH, usually is not higher than 5 %. At the same time, for arc surfacing methods mixing can be up to 15–40 % which requires multilayer deposition of the coating to achieve the desired properties [25].

Table 5 gives the generalized characteristic of PPH method, based on the data of published sources.

In [14] introducing a reinforcing bullet-resistant interlayer inside a multipass weld was realized by PPH, which allowed controlling the heat input, ensuring a shallow penetration depth, and, consequently, smaller mixing in the zone of fusion with the base. However, despite the technological advantages, the PPH method still has not become widely accepted for deposition of bullet-resistant reinforcing layers on the surface of armor steel welded joints. This is due both to high requirements to the process stability, and the need for further improvement of the technological parameters, allowing for the features of welding high-strength hardening steels. The technology is promising, but it requires further investigations in the direction of selection of powder compositions, lowering the residual stresses and increasing the adaptability to complex product geometries.

CONCLUSIONS

In welding armor steels of high and ultrahigh hardness achievement of equal strength of the welded joint with the base metal requires very complicated technological solutions and is practically impossible at present from the viewpoint of its implementation, while ballistic resistance of the joints should be provided due to design or local reinforcement.

In order to prevent excess softening of the HAZ metal during manufacture of welded assembly units of armored vehicle hulls from foreign-made steels, the content of Ni, Cr, Mo, B, as well as Si and V (in case of the steel alloying with them) should be the object of in-coming control. For this purpose, the minimal lower limit of their alloying element content should be determined by additional studies.

The main welding-metallurgical directions of enhancing the ballistic resistance of the weld metal in armor steel welded joints are as follows:

- differentiation of the mechanical properties by combining the welding, hardfacing and auxiliary materials;
- regulation of the structural and phase composition by introducing new welding materials, combined and hybrid welding technologies.

In the first area high-hardness layers on the surface or inside the metal of a multipass weld are created using hardfacing materials with high values of resistance under the conditions of high-speed shock-wave load.

In the second area a search is carried on to establish new compositions of welding materials capable of ensuring high values of deposited metal strength under the condition of preservation of its crack resistance, and the possibility of applying welding processes with filler material feed rate independent of energy parameters of the heat source, in particular hybrid processes, is investigated.

PPH application can be a promising method to enhance the bullet resistance of the welds and the softened sections of the HAZ, due to a controlled heat input, shallow penetration depth and wide range of powder materials for the reinforcing coating.

REFERENCES

1. Hazell, P.J. (2022) *Armour: Materials, theory, and design*. 2nd Ed. Boca Raton, London, New York, CRC Press. DOI: https://doi.org/10.1201/9781003322719
2. Rosenberg, Z., Dekel, E. (2020) *Terminal ballistics*. 3rd Ed. Cham, Springer Nature Switzerland AG. DOI: https://doi.org/10.1007/978-3-030-46612-1
3. Hanhold, B., Babu, S.S., Cola, G. (2013) Investigation of heat affected zone softening in armour steels. Part 1. Phase transformation kinetics. *Sci. and Technology of Welding and Joining,* 18(**3**), 247–252. DOI: https://doi.org/10.1179/1362171812Y.0000000100
4. Kostin, V.A., Poznyakov, V.D., Berdnikova, O.M. et al. (2020) Influence of structural transformations on mechanical properties of welded joints of armour steels. *Fizyko-Khimichna Mekhanika Materialiv*, 56(**4**), 36–43 [in Ukrainian].
5. *Madhusudhan* Reddy, G., Mohandas, T., Papukutty, K.K. (1998) Effect of welding process on the ballistic performance of high-strength low-alloy steel weldments. *J. of Materials Proc. Technology,* 74(**1-3**), 27–35. DOI: https://doi.org/10.1016/S0924-0136(97)00245-8
6. Slyvinskyy, O., Chvertko, Y., Bisyk, S. (2019) Effect of welding heat input on heat-affected zone softening in quenched and tempered armor steels. *High Temperature Material Proc.,* 23(**3**), 239–253. DOI: https://dx.doi.org/10.1615/HighTempMatProc.2019031690
7. Pang, W., Ahmed, N., Dunne, D. (2011) Hardness and microstructural gradients in the heat affected zone of welded low-carbon quenched and tempered steels. *Australasian Welding J.,* 56(**2**), 36–48.
8. Slyvins'kyy, O.A., Kvasnyts'kyy, V.V., Vladymyrskyi I.A. et al. (2024) Effect of heat input during welding on the microstructure and mechanical properties of the heat-affected zone of MIL-A-46100 armour steel. *Metallophysics and Advanced Technologies,* 46(**7**), 663–677. DOI: https://doi.org/10.15407/mfint.46.07.0663
9. Balakrishnan, M., Balasubramanian, V., Madhusudhan Reddy, G. (2013) Microstructural analysis of ballistic tests on welded armor steel joints. *Metallography, Microstructure,*

and Analysis, **2**, 125–139. DOI: https://doi.org/10.1007/s13632-013-0069-5
10. Balakrishnan, M., Balasubramanian, V., Madhusudhan Reddy, G. (2013) Effect of hardfacing consumables on ballistic performance of Q&T steel joints. *Defence Technology,* 9(**4**), 249–258. DOI: https://doi.org/10.1016/j.dt.2013.12.007
11. Garašić, I., Jurica, M., Iljkić, D., Barišić, A. (2019) Determination of ballistic properties on armox 500T steel welded joint. *Eng. Rev.,* 39(**2**), 186–196. DOI: https://doi.org/10.30765/er.39.2.8
12. DSTU V 9014:2020: *Arc welding of structures made of high-hardness steels for light-armored vehicles. Technical specifications*. Kyiv, DP "UkrNDNTs" [in Ukrainian].
13. Choo, S.-H., Baek, E.-R., Lee, S. (1996) Ballistic impact behavior of multilayered armor plates processed by hardfacing. *Metallurgical and Materials Transact. A,* **27**, 3335–3340. DOI: https://doi.org/10.1007/BF02663884
14. Balakrishnan, M., Balasubramanian, V., Madhusudhan Reddy, G. (2013) Effect of PTA hardfaced interlayer thickness on ballistic performance of shielded metal arc welded armor steel welds. *J. of Materials Eng. and Performance,* **22**, 806–814. DOI: https://doi.org/10.1007/s11665-012-0338-5
15. Klimpel, A., Luksa, K., Burda, M. (2010) Structure and properties of GMA surfaced armour plates. *Archives of Materials Sci. and Eng.,* 43(**2**), 109–116.
16. Ghauri, K.M., Iqbal, A., Ali, L., Ahmad, A., Hameed, G., Hussain, N. (2012) Enhancement of mechanical and ballistic properties of quenched and tempered high strength low alloy steel weldments. *J. of Faculty of Engineering & Technology,* 19(**1**), 27–41.
17. Slyvinskyy, O.A., Bornikov, A.S. (2018) Influence of carbon fiber additives on the structure and hardness of deposited austenitic metal. *Tekhnologicheskie Sistemy*, 2(**83**), 75–81. DOI: https://dx.doi.org/10.29010/083.9 [in Ukrainian].
18. Kim, C.J., Jeong, Y.C., Son, H.J., Seo, B.W., Kim, S., Lyu, S.-K., Hou, X., Cho, Y.T. (2024) Revolutionizing hardness via nanoparticle flux in welding of high-hardness armor steel. *Materials & Design,* **242**, 113001. DOI: https://doi.org/10.1016/j.matdes.2024.113001
19. *Krishna* Murthy, N., Janaki Ram, G.D., Murty, B.S. et al. (2014) Carbide-free bainitic weld metal: A new concept in welding of armor steels. *Metallurgical and Materials Transact. B,* **45**, 2327–2337. DOI: https://doi.org/10.1007/s11663-014-0120-1
20. Wang, W., Huo, L., Zhang, Y. et al. (2002) New developed welding electrode for improving the fatigue strength of welded joints. *J. of Materials Science & Technology,* 18(**6**), 527–531.
21. Skowronska, B., Szulc, J., Bober, M. et al. (2022) Selected properties of RAMOR 500 steel welded joints by hybrid PTA-MAG. *J. of Advanced Joining Processes,* **5**, 100111. DOI: https://doi.org/10.1016/j.jajp.2022.100111
22. Boulos, M.I., Fauchais, P., Pfender, E. (2023) *Plasma torches for cutting, welding and PTA coating*: Handbook of thermal plasmas. Cham, Springer, 659–741. DOI: https://doi.org/10.1007/978-3-030-84936-8_47
23. Rohan, P., Boxanova, M., Zhang, L. et al. (2017) High speed steel deposited by pulsed PTA — Frequency influence. In: *Proc. of the Inter. on ITSC 2017.* ASM International, 404–407. DOI: https://doi.org/10.31399/asm.cp.itsc2017p0404
24. Zikin, A., Hussainova, I., Katsich, C. et al. (2012) Advanced chromium carbide-based hardfacings. *Surface and Coatings Technology,* 206(**19–20**), 4270–4278. DOI: https://doi.org/10.1016/j.surfcoat.2012.04.039
25. Hållen, H., Lugscheider, E., Ait-Mekideche, A. (1991) Plasma transferred arc surfacing with high deposition rates. In: *Proc. of Conf. on Thermal Spray Coatings: Properties, Processes And Applications, Pittsburgh, USA*.
26. DuMola, R., Heath, G. (1997) New developments in the plasma transferred arc process. In: *Proc. of the Inter. Conf. on Thermal Spray.* ASM International, 427–434. DOI: https://doi.org/10.31399/asm.cp.itsc1997p0427
27. Wilden, J., Bergmann, J., Frank, H. (2006) Plasma transferred arc welding — Modeling and experimental optimization. *J. of Thermal Spray Technology,* **15**, 779–784. DOI: https://doi.org/10.1361/105996306X146767

ORCID
O.A. Slyvinskyy: 0000-0001-6418-4898,
M.M. Kovtoniuk: 0009-0007-8223-0983

CONFLICT OF INTEREST
The Authors declare no conflict of interest

CORRESPONDING AUTHOR
O.A. Slyvinskyy
National Technical University of Ukraine
"Igor Sikorsky Kyiv Polytechnic Institute"
37 Prosp. Beresteiskyi, 03056, Kyiv, Ukraine.
E-mail: o.slyvinsky@gmail.com

SUGGESTED CITATION
O.A. Slyvinskyy, M.M. Kovtoniuk (2025)
Approaches to enhancing the ballistic performance of welded joints in high and ultra-high hardness armor steels (Review).
The Paton Welding J., **12**, 11–19.
DOI: https://doi.org/10.37434/tpwj2025.12.02

JOURNAL HOME PAGE
https://patonpublishinghouse.com/eng/journals/tpwj

Received: 25.07.2025
Received in revised form: 16.10.2025
Accepted: 24.12.2025

DOI: https://doi.org/10.37434/tpwj2025.12.03

FORMATION OF COATINGS CONTAINING Ti_3AlC_2 MAX PHASE BY DEPOSITION OF TiC–TiAl POWDER BY PLASMA AND HIGH-VELOCITY OXY-FUEL SPRAYING METHODS

N.V. Vihilianska[1], T.V. Tsymbalista[1], P.P. Grishchenko[1], A.P. Murashov[1], O.Y. Gudymenko[2]

[1]E.O. Paton Electric Welding Institute of the NASU
11 Kazymyr Malevych Str., 03150, Kyiv, Ukraine
[2]V. Lashkaryov Institute of Semiconductor Physics of the NASU
45 Nauky Prosp., 03028, Kyiv, Ukraine

ABSTRACT

The work investigated the formation of coatings containing the MAX phase Ti_3AlC_2 by plasma and high-velocity oxy-fuel spraying using TiC–TiAl powder. The composite powder was produced by processing a powder mixture of the initial components TiAl and TiC in a planetary mill for 5 h, resulting in the formation of a powder with conglomerate-type particles containing the phases of the initial components and the target MAX phase Ti_3AlC_2. Coatings produced by plasma and high-velocity oxy-fuel spraying methods were investigated using X-ray phase analysis, optical microscopy and microdurometry. It was found that during plasma spraying, due to the intensive interaction of powder particles with the gas environment and high-temperature process conditions, the formation of titanium carbonitride $TiC_{0.2}N_{0.8}$ and a significant decrease in the content of the MAX phase Ti_3AlC_2 relative to the powder are observed in the coating. The coatings have a lamellar structure with high (~ 15 %) porosity and microhardness of 4390 ± 920 MPa. At high-velocity oxy-fuel spraying, due to the lower thermal load compared to the plasma spraying method, the coating retains most of the original phase composition of the powder. The coating structure is less lamellar and denser (porosity does not exceed 1 %), contains unmelted and partially melted deformed particles, and the average microhardness is 3810 ± 840 MPa.

KEYWORDS: coating, plasma spraying, high-velocity oxy-fuel spraying, MAX phase, phase composition, structure, microhardness

INTRODUCTION

Over the past two decades, a new class of nanolaminate compounds, the so-called MAX phases, which combine the properties of metals and ceramics, has attracted considerable attention of the scientific community. MAX phases with the general formula $M_{n+1}AX_n$ (n = 1, 2, 3,...) represent a large family of layered compounds with weak metallic bonds between M and A atoms and covalent bonds inside the layers $M_{n+1}X_n$, where M is an early transition metal; A is an element of group A; X–C, N, B and/or P [1]. Due to their unique structure, MAX phases exhibit excellent heat resistance, good electrical and thermal conductivity, relative ductility at high temperatures, and resistance to oxidation and thermal cycling [2]. Among the various compositions of MAX phases, the Ti–Al–C phases of system (Ti_2AlC and Ti_3AlC_2) are notable as one of the most thoroughly studied aluminium-containing carbides. These compounds are distinguished by high thermal stability, wear resistance, chemical inertness and the ability to form a protective α-Al_2O_3 film upon oxidation, which ensures their durability in aggressive environments [3, 4].

For the synthesis of MAX phases Ti_2AlC and Ti_3AlC_2, the methods of hot pressing [5], cold pressing followed by sintering (including spark plasma sintering) [6, 7], and mechanical alloying [8] are the most commonly used. The technology of self-propagating high-temperature synthesis, in the course of which synthesis occurs as a result of a solid-phase reaction, can also be considered a promising method for producing powders with MAX phase [9]. As initial materials, the powders of both simple elements (Ti, Al, C) and compounds (TiH_2, TiC, TiAl, TiO_2) in various combinations are used.

The most common methods for producing MAX phases on the surface of products in the form of thin films are phase vapour deposition (PVD) and magnetron sputtering [10]. Thermal spraying methods are used to deposit coatings with a thickness of > 50 μm.

The advantages of thermal spraying processes over other deposition methods are the simplicity of the equipment, the absence of the need to carry out the processes in a protective atmosphere and the ability to produce coatings of up to several mm thick on parts of various configuration. However, popular modern methods of thermal spraying, such as plasma and high-velocity oxy-fuel spraying (HVOF) have not found wide application for the formation of coatings based on Ti_3A1C_2 due to the high flame temperature, which usually causes decomposition and/or oxidation of the MAX phases [11, 12]. Instead, the methods of PS and HVOF are used to spray coatings based on the MAX

phase Ti_2A1C, in the phase composition of which, due to phase transformations during the spraying process, the MAX phase Ti_3A1C_2 is also formed [13–15].

Coatings with a high content of the MAX phase Ti_3A1C_2 (74–84 %) were produced by the plasma method using the sprayed material in the form of a suspension [16]. The formation of a high content of the MAX phase is probably associated with the formation of a protective aluminium oxide phase on the surface of the particles in a high-temperature vapour, which prevents further decomposition of the Ti_3AlC_2 phase.

Research is also being conducted on the development of composite coatings in which Ti_3A1C_2 MAX phase powder, which is usually produced by sintering, is used in coatings as a strengthening additive. Thus, to improve the operational characteristics of thermal protective coatings (TPC) under high temperature and high pressure, a new TPC design with a ZrO_2–Y_2O_3 ceramic layer and a NiCrAlY sublayer was developed, to which different amounts of Ti_3A1C_2 particles (5, 10, and 15 wt.%) were added [17]. The coatings were produced by supersonic plasma spraying. Studies of the resistance of coatings to high-temperature oxidation have shown that with 5 % of Ti_3A1C_2 in the sublayer, the coating exhibits a smaller weight increase than conventional TPC after oxidation at 950 °C for 80 h.

Composite coatings based on $LaMgAl_{11}O_{19}$ with the addition of 5, 10, and 20 wt.% Ti_3A1C_2 as a self-healing component and a binder for sintering [18]. The coatings were deposited by the plasma method, followed by annealing at 1200 °C to evaluate their self-healing ability; the behaviour during high-temperature oxidation in air and corrosion resistance at 1300 °C were studied. The results showed that an increase in the content of Ti_3A1C_2 significantly increases the self-healing efficiency, as evidenced by crack closure and pore isolation. The composite coating with 20 wt.% of Ti_3A1C_2 demonstrated the highest stability under the studied conditions and the stability of the phase composition, which indicates the prospects of its use as a hardened coating at high temperatures.

A nanocomposite coating was produced by plasma spraying of a powder mixture of 50 % of Ti_3A1C_2 – 50 % of Cu [19]. It was found that the nanocomposite coating has an unusual microstructure with nanomicrometre phase synergistic enhancement, consisting of submicrometre layers of Cu and nanoparticles of Cu(Al), Ti_4O_5, TiO_2 and $A1_2TiO_5$. During the spraying process, Al is removed from Ti_3AlC_2, forming a large amount of ductile Cu(Al) and diffusion of Cu into Ti_3AlC_2 occurs, resulting in the formation of a spatial Cu mesh structure in the coating. The nanocomposite coating has a high fracture toughness and resistance to crack growth, as confirmed by a three-point bending test.

THE AIM

of this study was to investigate the formation of coatings under plasma and high-velocity oxy-fuel spraying of coatings containing the MAX phase Ti_3A1C_2 when using mechanically synthesized TiC–TiAl powder for spraying.

MATERIALS AND RESEARCH PROCEDURES

The composite powder (CP) of the TiC–TiAl system was used as a material for spraying coatings. It was produced by the method of mechanochemical synthesis (MChS) by processing the initial TiAl and TiC powders in a high-energy planetary mill Activator 2SL for 5 h at a speed of 600/900 rpm. X-ray diffraction patterns of the initial TiAl and TiC powders used to produce the CP by the MChS method and their characteristics are shown in Figure 1 and Table 1, respectively.

The content of the initial powders in the mixture was calculated to produce the MAX phase Ti_3AlC_2 by reaction (1) and was 38.5TiAl + 61.5TiC (wt.%).

$$TiAl + 2TiC = Ti_3AlC_2. \quad (1)$$

Plasma spraying was carried out in a serial installation UPU-8M using a Metco F4 MB plasmatron

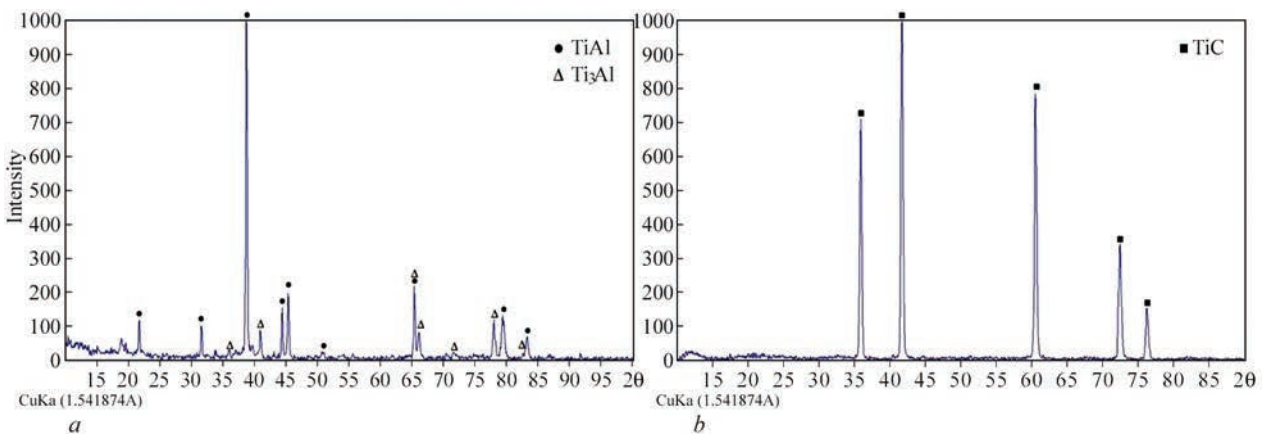

Figure 1. X-ray diffraction patterns of initial powders: *a* — TiAl; *b* — TiC

Table 1. Characteristics of initial powders used to produce the CP by the MChS method

Powder	Particle size, μm	Chemical composition, wt.%	Phase content, %
TiAl	< 40	Ti – 62.5; Al – 37.5	TiAl – 91; Ti_3Al – 9
TiC	40–63	Ti – 79.2–80; C – 19.4–20.2	TiC – 100

type. To spray coatings by the high-velocity oxy-fuel spraying method, the VShGPN-1 installation was used produced at the PWI on the basis of the HIPOJET 2700M prototype (Metallizing Equipment Co. Pvt. Ltd., India). The technological parameters of the PS and HVOF are given in Tables 2 and 3.

To study the powders and spraying coatings, metallography, microdurometry, and X-ray diffraction phase analysis (XRD) were used.

To study the structure of powders and sprayed coatings, a Neophot-32 optical microscope with a digital photography device was used. For quantitative analysis of the pore content in the coatings, an optical procedure (image analysis method) was used, which consists in determining the area falling on the detected pores relative to the entire surface area of the coating section. The digital image was processed by Image- Pro Plus software, which allows measuring porosity (highlighting inclusions that differ in colour and brightness), determining the number and percentage of pores by area.

Microhardness measurements were performed using a PMT-3 device at a load of 50 g. Each specimen was subjected to 30–50 measurements, followed by the determination of the average value and the construction of variation curves that allow finding the most probable microhardness values.

The phase composition of the powder and coating particles was studied using a PANalytical X'Pert PRO diffractometer with CuKαl radiation (λ = 0.15406 nm).

Table 2. Technological parameters of PS-coatings of TiC–TiAl powder system

Parameter	Value
Current, A	600
Voltage, V	40
Plasma gas flow rate Ar/N_2, l/min	30
Proportions of plasma-forming gas Ar/N_2, %	80/20
Transport N_2 gas flow rate, l/min	5
Powder flow rate, kg/h	1.4
Spraying distance, mm	100

Table 3. Technological parameters of HVOF-coatings of TiC–TiAl powder system

Parameter	Value
Fuel gas flow rate CH_4, l/min	28
Fuel gas pressure CH_4, atm	5.5
Oxygen flow rate, m^3/h	4
Oxygen pressure, atm	8
Air flow rate, m^3/h	15
Air pressure, atm	5
Transport gas flow rate, l/min	20
Transport gas pressure, atm	5
Spraying distance, mm	140

The voltage on the tube anode was 45 kV, the current was 40 mA. The diffraction patterns were recorded in increments of 0.025° with an acquisition time of 1 s. The diffractometric data were processed using the High Score Plus software.

RESULTS OF THE EXPERIMENT AND THEIR DISCUSSION

When a TiC–TiAl powder mixture is processed in a planetary mill for 5 h as a result of repeated processes, particle grinding, and cold welding, the final

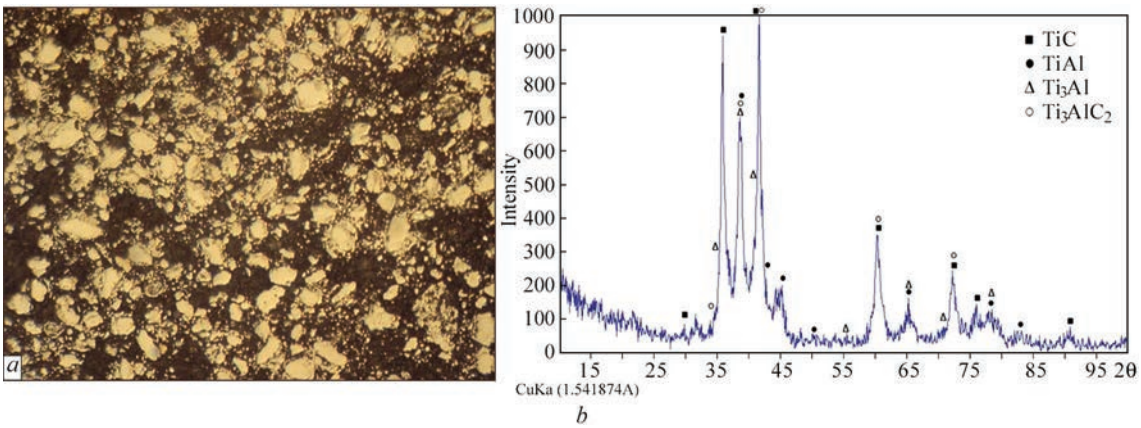

Figure 2. Microstructure (×400) (*a*) and X-ray diffraction pattern (*b*) of TiC–TiAl MChS powder

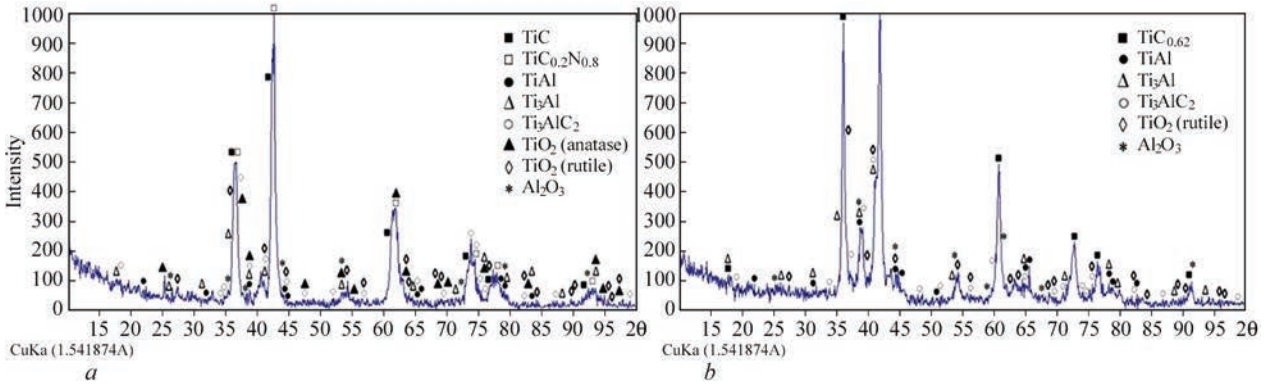

Figure 3. X-ray diffraction patterns of coatings produced by spraying TiCT–iAl MChS powder by plasma (*a*) and high-velocity oxy-fuel spraying (*b*)

MChS product is a composite powder consisting of conglomerate-type particles with a size of < 40 μm (Figure 2, *a*).

The X-ray phase analysis (Figure 2, *b*) revealed that the produced MChS powder has a multiphase structure consisting of the initial components (TiC, TiAl, and Ti_3A1) and the MAX phase Ti_3A1C_2, a product of the interaction of the initial components.

According to XRD data, the coating deposited by the plasma method of TiC-TiAl MChS powder consists of TiC carbide and titanium carbonitride phases $TiC_{0.2}N_{0.8}$, intermetallic phases TiAl, Ti_3Al, MAX phase Ti_3AlC_2, TiO_2 oxide in two modifications of rutile and anatase, and aluminium Al_2O_3 oxide (Figure 3, *a*). As a result of phase transformations occurring in the powder during the plasma spraying process, the intensity of peaks corresponding to the intermetallic phases TiAl, Ti_3A1, and the MAX phase Ti_3A1C_2 significantly decrease compared to the MChS powder. The main phases in the produced coating are TiC and $TiC_{0.2}N_{0.8}$. Here, the intensity of the TiC peak is also slightly decreasing relative to the initial powder, indicating a lower amount of this phase in the coating than in the powder. The presence of titanium carbonitride in the coating indicates the interaction of TiC carbide with nitrogen in the gas environment with the following reaction:

$$TiC + N_2 \rightarrow TiC_xN_{1-x}(0 \le x \le 1), \quad (2)$$

where x defines the ratio of carbon to nitrogen in the solid phase.

The formation of titanium oxide can be caused by the reaction of the titanium component of both TiC carbide, the MAX phase Ti_3A1C_2, and titanium aluminide with air oxygen.

In contrast to plasma spraying, no significant phase transformations occur during the spraying process when the TiC-TiAl powder is sprayed by the HVOF method (Figure 3, *b*). The main phase in the coating is titanium carbide of non-stoichiometric composition of $TiC_{0.62}$, the formation of which is the result of decarburization, i.e., a decrease in the carbon concentration in the structure of titanium carbide (TiC). This process typically occurs under conditions when carbon is removed from the lattice, forming the stoichiometry TiC_x, where $x < 1$, through interaction with the environment. The carbon in TiC can be oxidized in the presence of oxygen to form gaseous oxides such as CO_2 (or CO) by reaction:

$$TiC+0.38O_2 \rightarrow TiC_{0.62}+0.38CO_2. \quad (3)$$

The HVOF-coating also contains titanium aluminide phases TiAl, Ti_3Al, and the MAX phase Ti_3A1C_2, which have slightly lower intensity of phase peaks in the XRD pattern than in the XRD pattern of the MChS powder. In contrast to plasma spraying, the coating does not form a TiCN phase due to the shorter residence time of the particles in the spray flow due to the higher particle flight velocity at HVOF and, accordingly, the shorter interaction time of the titanium carbide powder particles with the gas environment. During the spraying process, only a slight oxidation of the titanium component occurs with the formation of the rutile modification in the titanium dioxide TiO_2 coating.

A decreased amount of the Ti_3A1C_2 MAX phase in the PS- and HVOF-coatings of the TiC–TiAl system relative to the MChS powder is a consequence of its oxidation and decomposition under the influence of high temperatures. This is a multistage process that includes structure degradation, interaction with oxygen, and formation of oxide products. At the first stage, at temperatures of 600–800 °C, Al is oxidized, as it is the most reactive element in the system and is the first to be oxidized, forming aluminium oxide. Aluminium oxide acts as a protective layer that limits further reaction and partially slows down the further oxidation. At the second stage, at temperatures of 800–1000 °C, the structure of the MAX phase degrades due to the release (loss) of aluminium. The residual titanium and carbon form titanium carbide TiC, which subsequently reacts with oxygen to form titanium dioxide TiO_2 and gaseous CO_2 (or CO). At a temperature above

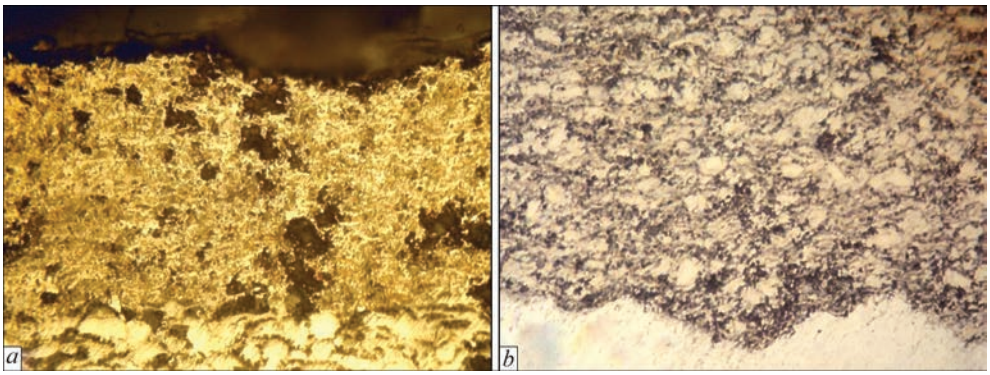

Figure 4. Microstructure (×400) of coatings produced by spraying TiC–TiAl MChS powder by plasma (*a*) and high-velocity oxy-fuel spraying (*b*)

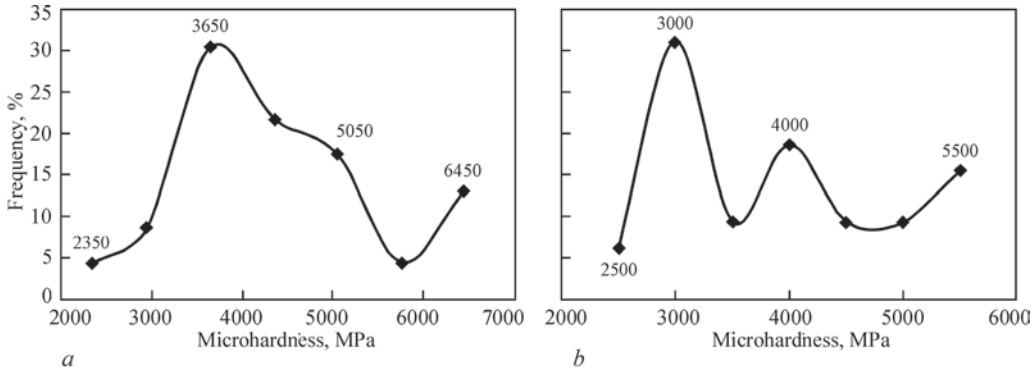

Figure 5. Variation curves of the distribution of microhardness values of coatings produced by spraying TiC–TiAl MChS powder by plasma (*a*) and high-velocity oxy-fuel spraying (*b*)

1000 °C, titanium carbide is actively oxidized and stable TiO_2 phases (rutile or anatase, depending on the temperature) and Al_2O_3 (corundum) are formed. The complete oxidation reaction of Ti_3AlC_2 in an oxygen environment is as follows:

$$4Ti_3AlC_2 + 23O_2 \rightarrow 12TiO_2 + 2Al_2O_3 + 8CO_2. \quad (4)$$

The results of the examination of the structure of the plasma coating of the TiC–TiAl system showed that it has a thin-lamellar heterogeneous structure (Figure 4, *a*). The lamellae of the coating have different colours ranging from light yellow to dark brown (oxide colour). The more intense yellow colour of the lamellae in the coating probably corresponds to the TiCN phase.

The coating contains defects in the form of pores and chipping in the amount of ~15 %. Chipping in the coating can occur due to the insufficient content of a ductile metal matrix in them, and during the preparation of specimens for microstructure examinations, solid particles of titanium carbides and carbonitrides, whose hardness can be 20–32 GPa [20], fall out of the coating due to low cohesive strength.

The structure of the HVOF-coating of the TiC–TiAl system has a structure with a slight degree of lamellarity (Figure 4, *b*). The coating is predominantly formed of unmelted partially deformed particles, which indicates that refractory powder particles during the short time of the particles' stay in the jet do not have time to receive the necessary thermal energy, go through the melting stage necessary for heating the powder particles and obtaining ductility. Therefore, due to the high flight velocity, some of the powder particles enter the coating in a solid state. The structure of the unmelted particles is similar to that of the initial powder. The porosity of the coating does not exceed 1 %.

The average microhardness of the plasma coating is 4390 ± 920 MPa. The multiphase nature of the coating is confirmed by the variation curve constructed from the microhardness values and the presence of 3 peaks on the curve corresponding to values of 3650, 5050 and 6450 MPa (Figure 5, *a*).

The average microhardness of the HVOF-coating is 3810 ± 840 MPa. There are three main peaks of microhardness values on the variation curve, corresponding to values of 3000, 4000 and 5500 MPa (Figure 5, *b*). The microhardness values at these peaks correspond to the titanium aluminide compounds TiAl, Ti_3Al (3500–4700 MPa [21] and ~ 5000 MPa [22], respectively) and the MAX phase Ti_3AlC_2 (2200–3460 MPa [23]). The absence of pronounced peaks of microhardness values on the variation curves of coatings of both types, which would correspond to the hardness values of titanium carbide and carboni-

tride (20000–32000 MPa), indicates the uniform distribution of these compounds in the cross-section of coatings in the form of small inclusions.

CONCLUSIONS

By the method of mechanochemical synthesis using a mixture of TiAl and TiC initial powders, the composition of which is designed to produce the final product of the Ti_3AlC_2 MAX phase, a composite powder with a conglomerate multiphase structure was obtained with the presence of phases of the initial components of the mixture and their interaction product — the MAX phase Ti_3AlC_2.

The coatings produced by the plasma spraying method have a thin-lamellar heterogeneous structure. A significant transformation of the phase composition of the powder during the spraying process under the influence of high temperatures and gas environment was established, in particular, the formation of the carbonitride phase $TiC_{0.2}N_{0.8}$ of titanium and aluminium oxides and a decrease in the content of the MAX phase.

The coatings deposited by the high-velocity oxy-fuel spraying method have a structure formed of partially unmelted particles with a low degree of lamellarity. The phase composition of the coating differs slightly from the phase composition of the MChS powder, which indicates limited phase transformations during spraying due to the shorter interaction time of the powder particles with the gas environment.

In both types of coatings, a decrease in the content of the MAX phase Ti_3AlC_2 is observed compared to the initial powder, which is determined by its thermal destruction and oxidation during spraying. According to the change in the intensity of the peaks corresponding to the MAX phase, this decrease is ~ 88 % for PS and ~ 52 % for HVOF.

The average microhardness of the coatings is 4390 ± 920 MPa for PS and 3810 ± 840 MPa for HVOF. The variation curves of microhardness confirm the multiphase nature of the coatings, and the absence of individual peaks on the curves that would correspond to high-hardness inclusions of carbide components indicates their uniform distribution in the structure of the coatings.

REFERENCES

1. Dahlqvist, M., Barsoum, M. W., Rosen J. (2024) MAX phases — Past, present, and future. *Materials Today*, **72**, 1–24. DOI: https://doi.org/10.1016/j.mattod.2023.11.010
2. Radovic, M., Barsoum, M. W. (2013) MAX phases: Bridging the gap between metals and ceramics. *American Ceramic Soc. Bulletin,* 92(**3**), 20–27.
3. Li, X., Xie, X., Gonzalez-Julian, J. et al. (2020) Mechanical and oxidation behavior of textured Ti_2AlC and Ti_3AlC_2 MAX phase materials. *J. of the European Ceramic Soc.*, 40(**15**), 5258–5271. DOI: https://doi.org/10.1016/j.jeurceramsoc.2020.07.043
4. Li, X., Zheng, L., Qian, Y. et al. (2017) Effects of high temperature oxidation on mechanical properties of Ti_3AlC_2. *J. Mater. Sci. Technol.* 33(**6**), 596–602. DOI: 10.1016/j.jmst.2016.05.004.
5. Wei, L., Liu, J., Wu, X. et al. (2019) In situ fabrication of Ti–Al/Ti_2AlC composite by hot-press sintering. *J. of Alloys and Compounds*, **813**, 52220. DOI: https://doi.org/10.1016/j.jallcom.2019.152200
6. Wang, P., Bingchu, M., Xiaolin H. et al. (2007) Fabrication of Ti_2AlC by spark plasma sintering from elemental powders and thermodynamics analysis of Ti–Al–C system. *J. of Wuhan University of Technology-Mater. Sci. Ed.*, 22(**2**), 325–328. DOI: https://doi.org/10.1007/s11595-006-2325-x
7. Xie X., Yang, R., Cui, Y. et al. (2020) Fabrication of textured Ti_2AlC lamellar composites with improved mechanical properties. *J. of Material Sci. and Technology*, **38**, 86–92. DOI: https://doi.org/10.1016/j.jmst.2019.05.070
8. Sadeghi, E., Karimzadeh, F., Abbasi, M.H. (2013) Thermodynamic analysis of Ti–Al–C intermetallics formation by mechanical alloying. *J. of Alloys and Compounds*, **576**, 317–323. DOI: https://doi.org/10.1016/j.jallcom.2013.05.196
9. Edrisi, A., Aghajani, H., Seyedein, S.H. et al. (2024) Synthesis of high purity Ti_2AlC MAX phase by combustion method through thermal explosion mode: Optimization of process parameters and evaluation of microstructure. *Ceramics Inter*. DOI: https://doi.org/10.1016/j.ceramint.2024.09.431
10. Eklund, P., Beckers, M., Jansson, U. et al. (2010) The Mn+1AXn phases: Materials science and thin-film processing. *Thin Solid Films*, 518(**8**), 1851–1878. DOI: https://doi.org/10.1016/j.tsf.2009.07.184
11. Vihilianska, N.V., Filonenko, D.V., Yushchenko, A.O. et al. (2024) Thermal spraying of coatings, containing Cr_2AlC MAX-phase (Review). *Avtomatychne Zvaryuvannya,* **1**, 51–59. DOI: https://doi.org/10.37434/as2024.01.06
12. Vihilianska, N., Yantsevich, K., Olevska, L. et al. (2024) Formation of coatings based on MAX phase Ti_3SiC_2 under gas-thermal deposition methods (Review). *Visnyk KrNU*, 4(**147**), 135–142.
13. Frodelius, J., Sonestedt, M., Björklund, S., et al. (2008) Ti_2AlC coatings deposited by high velocity oxy-fuel spraying. *Surf. Coat. Technol.,* 202(**24**), 5976–5981. DOI: https://doi.org/10.1016/j.surfcoat.2008.06.184
14. Sonestedt, M., Frodelius, J., Palmquist, J.-P. et al. (2010) Microstructure of high velocity oxy-fuel sprayed Ti_2AlC coatings. *J. of Materials Sci.*, 45(**10**), 2760–2769. DOI: https://doi.org/10.1007/s10853-010-4263-4
15. Zhang, Z., Lim, S. H., Chai, J. et al. (2017) Plasma spray of Ti_2AlC MAX phase powders: Effects of process parameters on coatings properties. *Surf. Coat. Technol.*, **325**, 429–436. DOI: https://doi.org/10.1016/j.surfcoat.2017.07.006
16. Yu, H., Suo, X., Gong, Y. et al. (2016) Ti_3AlC_2 coatings deposited by liquid plasma spraying. *Surf. Coat. Technol.,* **299**, 123–128. DOI: https://doi.org/10.1016/j.surfcoat.2016.04.076
17. He, W., Li, J., Liu, K. (2024) Ti_3AlC_2-modified NiCrAlY as a metallic bond coat for thermal barrier coatings: A study on high-temperature oxidation resistance. *J. of Physics: Conference Series,* **2808**, 012009. DOI: https://doi.org/10.1088/1742-6596/2808/1/012009
18. Huang, J., Chen, W., Lü, K.et al. (2024) Self-healing and thermal stability of $LaMgAl_{11}O_{19}$–Ti_3AlC_2 composites for high-temperature abradable applications. *Coatings*, 14(**8**), 938. DOI: https://doi.org/10.3390/coatings14080938
19. Li, Q., Yuan, X., Xu, H. (2019) Microstructure and fracture toughness of *in-situ* nanocomposite coating by thermal spray-

ing of Ti_3AlC_2/Cu powder. *Ceramics Inter.*, 45(**10**), 13119–13126. DOI: https://doi.org/10.1016/j.ceramint.2019.03.246
20. Matthews, A., Leyland, S. (1995) ASM Engineered Materials Reference Book. 2nd Ed. by Michael Bauccio. ASM International, Materials Park, OH, 1994 Hard Coatings for Tribological Applications. *Surf. Coat. Technol.*, **71**, 71–78.
21. Cui, N., Wu, Q., Yan, Z., Zhou, H., Wang, X. (2019) The microstructural evolution, tensile properties, and phase hardness of a TiAl alloy with a high content of the β phase. *Materials*, 12(**17**), 2757. DOI: https://doi.org/10.3390/ma12172757
22. Li, K., Wang, X., Chen, H. et al. (2023) Fabrication of Ti_3Al-based intermetallic alloy by laser powder bed fusion using a powder mixture. *Materials,* 16(**7**), 2699. DOI: https://doi.org/10.3390/ma16072699
23. Wang, X.H., Zhou, Y.C. (2010) Layered machinable and electrically conductive Ti_2AlC and Ti_3AlC_2 ceramics: A review. *J. Materials Sci. and Technology*, 26(**5**), 385–416. DOI: https://doi.org/10.1016/s1005-0302(10)60064-3

ORCID
N.V. Vihilianska: 0000-0001-8576-2095,
T.V. Tsymbalista: 0000-0001-9569-7776,
P.P. Grishchenko: 0000-0003-2640-8656,
A.P. Murashov: 0000-0002-0357-9068,
O.Y. Gudymenko: 0000-0002-5866-8084

CONFLICT OF INTEREST
The Authors declare no conflict of interest

CORRESPONDING AUTHOR
N.V. Vihilianska
E.O. Paton Electric Welding Institute of the NASU
11 Kazymyr Malevych Str., 03150, Kyiv, Ukraine.
E-mail: pewinataliya@gmail.com

SUGGESTED CITATION
N.V. Vihilianska, T.V. Tsymbalista, P.P. Grishchenko, A.P. Murashov, O.Y. Gudymenko (2025) Formation of coatings containing Ti_3AlC_2 MAX phase by deposition of TiC–TiAl powder by plasma and high-velocity oxy-fuel spraying methods.
The Paton Welding J., **12**, 20–26.
DOI: https://doi.org/10.37434/tpwj2025.12.03

JOURNAL HOME PAGE
https://patonpublishinghouse.com/eng/journals/tpwj

Received: 07.08.2025
Received in revised form: 07.11.2025
Accepted: 24.12.2025

DOI: https://doi.org/10.37434/tpwj2025.12.04

FEATURES OF FORMATION OF BIOCOMPATIBLE COATINGS FROM SILVER-DOPED HYDROXYAPATITE POWDER BY MICROPLASMA SPRAYING

S.M. Kaliuzhnyi[1], S.Yu. Maksymov[1], S.G. Voinarovych[1], O.M. Kyslytsia[1], N.V. Ulyanchich[2], V.V. Kolomiiets[2], V.M. Teplyuk[1], N.V. Prokhorenkova[3]

[1]E.O. Paton Electric Welding Institute of the NASU
11 Kazymyr Malevych Str., 03150, Kyiv, Ukraine
[2]Frantsevich Institute for Problems of Materials Science of the NASU
3 Omeliana Pritsaka Str., 03142, Kyiv, Ukraine
[3]School of Traditional and Alternative Energy, D. Serikbayev East Kazakhstan Technical University
69 Protozanov Str., Ust-Kamenogorsk, 070004, Kazakhstan

ABSTRACT

The work investigates the formation of bioceramic coatings from hydroxyapatite (HAp) doped with silver (HAp+Ag) using the microplasma spraying (MPS) method on titanium substrates. The influence of MPS technological parameters (current, plasma-forming gas flow rate, spraying distance) and particle size of the powder on the degree of particle melting, surface morphology and phase composition of the coatings was analyzed. It was established that optimization of MPS modes in an argon microplasma jet makes it possible to control the thermal decomposition of HAp and the ratio of crystalline to amorphous phases during the formation of HAp+Ag coatings. It was proven that HAp+Ag coatings produced by MPS exhibit antibacterial activity against Escherichia coli, Staphylococcus aureus, and Pseudomonas aeruginosa: they completely inhibit the growth of E. coli and significantly reduce the viability of the other tested microorganisms. HAp+Ag coatings on a zirconium interlayer demonstrated an adhesion strength exceeding 15 MPa, which is sufficient for their application on implant surfaces. The obtained results confirm the effectiveness of the applied MPS method and its prospects for creating economical, technologically optimized, and biofunctional coatings on titanium implants.

KEYWORDS: microplasma spraying, biocompatible coating, silver-doped hydroxyapatite, splat test, phase composition of coatings

INTRODUCTION

The use of metal implants in orthopaedics and dentistry is accompanied by a number of problems related to ensuring their osseointegration and long-term stability in the body.

One of the most effective approaches to improving the osseointegrative properties of bioinert titanium alloys is modifying their surface by applying bioceramic coatings based on hydroxyapatite (HAp ($Ca_{10}(PO_4)_6(OH)_2$)), the main mineral component of bone tissue [1].

Hydroxyapatite coatings promote the formation of a strong and stable contact between the implant and bone tissue, accelerate the process of osseointegration, and reduce the risk of metal ions being released from the alloy into the surrounding tissues, which reduces the probability of cytotoxic reactions [2].

However, such coatings do not eliminate the problem of bacterial infections, which still remain one of the leading causes of post-surgery complications [3].

Recent studies focus on developing strategies for long-term antibacterial protection of implant surfaces. A promising solution is to alloy HAp coatings with metal ions that have pronounced antimicrobial activity, particularly silver, which significantly reduces the risk of infection without the need for systematic antibiotic use [4, 5].

Various methods are used to form HAp coatings: sol-gel synthesis, plasma and laser spraying, pulsed and electrophoretic deposition, biomimetic approaches, microarc oxidation, RF and microwave spraying, electrospinning, spray pyrolysis, as well as their combinations [6–8]. The most widely used method is plasma arc spraying due to its relatively low cost, technological feasibility, and the ability to apply coatings to complex-shape products. Notably that this technology has been approved by the FDA (Food and Drug Administration, USA) for the creation of HAp coatings on medical implants [9, 10].

However, conventional plasma arc spraying has a number of limitations. The extreme thermal conditions of the process (the temperature of the plasma jet reaches 10000–15000 K), as well as the difference in the thermal expansion coefficients of the metal substrate and ceramic coating, cause residual stresses, cracking and reduced adhesion [11]. In this regard, microplasma spraying (MPS) technology is undergoing intensive development, which enables a significant reduction in the thermal impact on the substrate [12–15].

The key advantage of MPS is the use of a laminar microplasma jet with an extended high-temperature zone, which ensures uniform heating of powder particles and reduces the risk of overheating or decomposition. The use of argon as a plasma-forming gas further minimizes thermal gradients within the particles. The lower thermal power of the microplasma jet allows applying coatings even on small, thin-walled products without the risk of deformation.

Today, a significant number of studies are devoted to modelling and analyzing the influence of technological parameters (plasmatron power, spraying distance, composition and flow rate of plasma-forming gas, powder transportation) on the properties of the produced coatings [16–18].

As is known, thermal spraying involves the deposition of molten or semi-molten particles onto a rough surface of the substrate. Upon impact, they deform, forming splats that quickly solidify and form a coating layer. The nature of the interaction between the particles and the substrate affects their adhesion, and the subsequent build-up of layers forms the microstructure of the coating [19]. Properties such as porosity and adhesion strength directly depend on the characteristics of individual splats [20]. Therefore, studying the mechanisms of their formation is important for optimizing the technology.

Despite numerous theoretical, analytical and experimental studies, the process of splat formation during the creation of silver-doped hydroxyapatite (HAp+Ag) coatings using the MPS method remains insufficiently studied.

THE AIM OF THE WORK

was to study the influence of microplasma spraying technological parameters and powder particle size on the state of HAp+Ag powder particles during their collision with the substrate, as well as to analyze phase transformations in coatings and determine their antibacterial properties.

MATERIALS, EQUIPMENT AND METHODS USED IN THE EXPERIMENT

The sprayed material was ceramic powders of silver-doped hydroxyapatite (2 %) (BIOMATTECH Scientific and Technical Solutions Centre, Ukraine) of high purity (> 99 %) with particle sizes of 40–63 and 80–100 μm. The powders were produced by chemical precipitation from calcium salts (calcium nitrate tetrahydrate) and ammonium salts (diammonium phosphate), followed by ageing, washing, separation and drying of the formed precipitate, as well as its subsequent mechanical and heat treatment. The powder particles are predominantly fragmentary in shape (Figure 1, *a*), but due to the rolling operation, the corners of many particles are smoothed (Figure 1, *b*), which provided them with sufficient fluidity — 68–75 s/50 g.

The results of the analysis of the phase composition of HAp+Ag powders are shown in Figure 2.

The phase composition of the powder is completely crystalline $Ca_{10}(PO_4)_6(OH)_2$, with a Ca/P ratio of 1.67. Testing the fluidity of HAp powders under the operating conditions of the powder dispenser supplied with the MPS-004 installation showed that the produced powders have sufficient fluidity to ensure a stable and reproducible spraying process.

For experiments on spraying HAp+Ag powders, the MPS-004 microplasma spraying installation, equipped with a microplasmatron produced by PWI (Ukraine) was used [21]. More details on the features of the microplasma spraying process for biocompatible coatings from hydroxyapatite are described in the previous work [22].

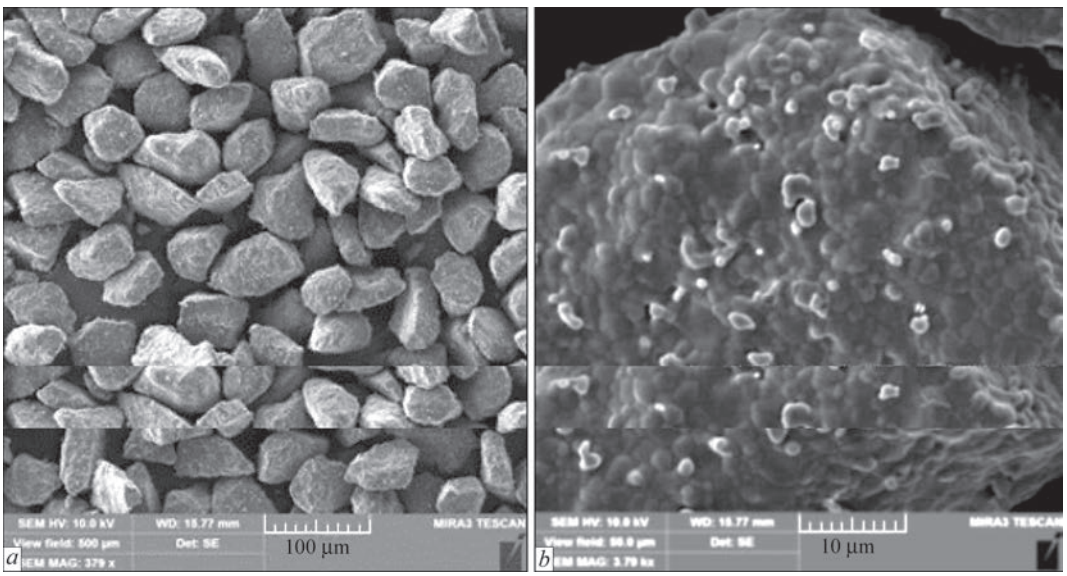

Figure 1. Appearance of HAp+Ag powder particles with a fraction of 40–63 μm

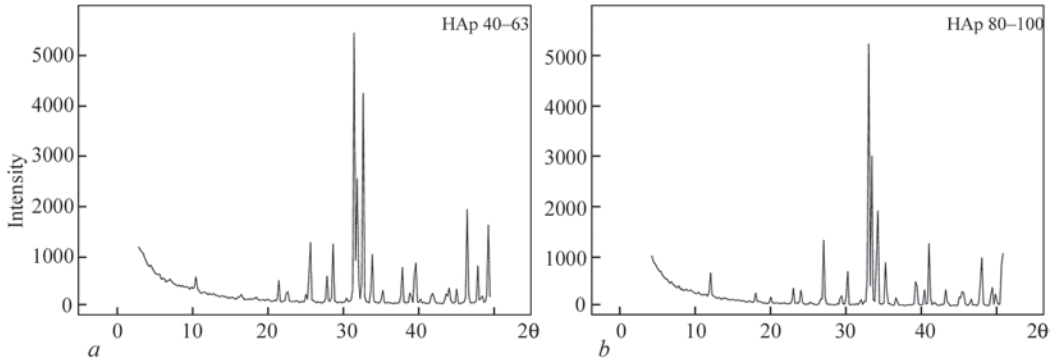

Figure 2. XRD results of HAp+Ag powders: *a* — fractions of 40–63 μm and *b* — fractions of 80–100 μm

To study the influence of MPS mode parameters, such as current (I, A), plasma-forming gas flow rate (Q_m, l/min), spraying distance (H, mm) and powder fraction (their average size (D_{fr}, μm) was selected) on the melting of HAp+Ag powder particles, the "splat test" method was used. The values of the spraying mode parameters were selected according to the experimental plan, which was developed using the mathematical planning method with the application of the 2^{4-1} matrix (Table 1).

The splats were obtained by moving glass plates with the size of 75×25×2 mm in a plane perpendicular to the axis of the microplasma jet. As a result, individual particles of the sprayed material, deformed upon contact with its surface, were adhered on the glass substrate in the form of splats. Visual inspection of the appearance of the splats was performed using a Nikon D40x digital camera (Nikon Corporation, Japan) mounted on a Unitron Versamet 2 microscope (Unitron Inc., USA). Based on the appearance and structure of the powder particles adhered on the substrate in the form of splats, their classification and analysis of the state in which the particle was at the moment of collision with the substrate were carried out.

The structure and elemental composition of the specimens were studied on cross-sections. The sections were prepared by stepwise grinding and polishing according to standard procedures using equipment and consumables from Struers Company (Denmark). Microstructural examinations were carried out in a CamScan S4 scanning electron microscope (Cambridge Scanning Company Ltd., UK) in the elastic backscattered electron (phase contrast) mode at an accelerating voltage of 20 kV. The elemental composition was analyzed using electron probe microanalysis (EPMA) with an Oxford Link Pentafet 5518 EDS energy dispersive detector and INCA 4.05 software. The detector was calibrated using cobalt at a voltage of 20 kV. Measurements were conducted at 20 kV. The absolute error of the method in quantitative analysis does not exceed 5 %, and with a calibration specimen, it is 2.5 %. The error in calculating the elements from the obtained spectra depends on the surface roughness, the spectrum acquisition time, and the chemical element, and ranges from 0.15 to 0.85 %.

X-ray examination of powders and coatings was performed using the method of wide-angle X-ray diffraction with an XRD-7000 diffractometer (Shimadzu, Japan), whose X-ray optical scheme is implemented by passing the primary beam through the specimen using CuK_α radiation (λ = 1.54 Å). When analysing the obtained diffraction patterns, the content of the crystalline phase $Ca_{10}(PO_4)_6(OH)_2$ was determined, as well as impurities of other crystalline or amorphous phases. Plates made of VT1-00 titanium of 10×10 mm were used as a substrate.

The antibacterial activity of the HAp+Ag coating against Pseudomonas aeruginosa, Staphylococcus aureus and Escherichia coli pathogens was evaluated in accordance with DSTU ISO 18593–2006 at the L.I. Medved's Research Center of Preventive Toxicology, Food and Chemical Safety of the Ministry of Health of Ukraine.

RESEARCH RESULTS AND THEIR DISCUSSION

Using an approach that involves distinguishing three characteristic zones in the cross-section of a HAp particle formed during its heating and melting in a plasma jet — an unmelted crystalline core, a layer of molten stoichiometric HAp, and an outer overheated layer with thermal decomposition products [23, 24], an analysis of the images of the splats obtained during

Table 1. Matrix for studying the influence of MPS mode parameters on the state of (HAp+Ag) powder particles during spraying

Mode No.	I, A	Q_m, l/min	H, mm	D_{fr}, μm
1	45	2	160	90
2	45	2	80	50
3	45	1	160	50
4	45	1	80	90
5	35	2	160	50
6	35	2	80	90
7	35	1	160	90
8	35	1	80	50

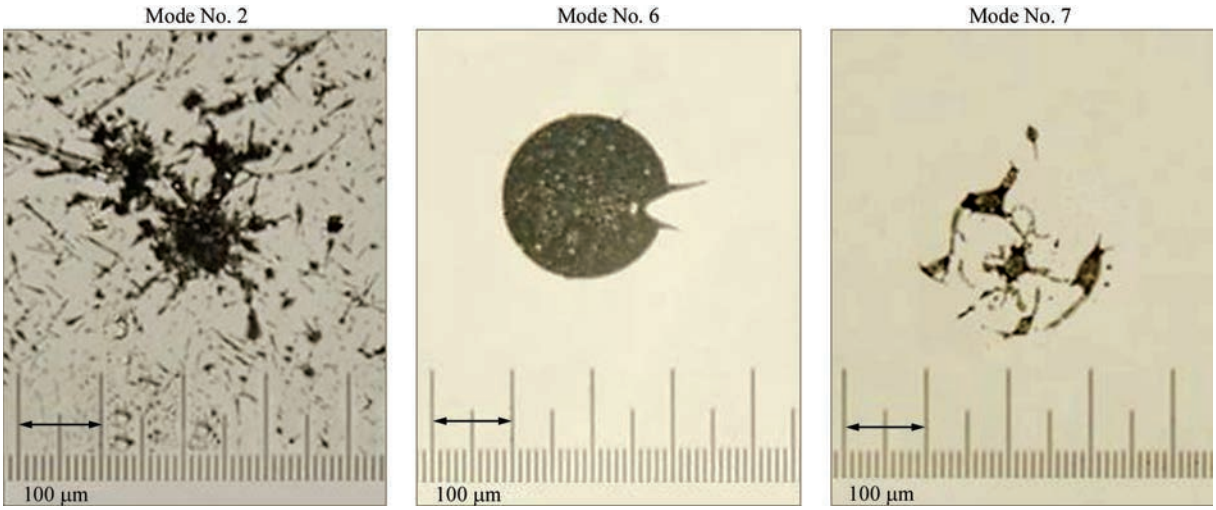

Figure 3. Splats of powder particles (HAp+Ag) at different MPS modes

the experiment was carried out. As a result, three characteristic types of splats were identified, the appearance of which is shown in Figure 3.

Analysis of the influence of technological parameters (current, plasma-forming gas flow rate, spraying distance) and powder particle size showed that complete melting of the material occurs in all MPS modes except No. 7 (Table 1). This is determined by the use of the minimum value of current at mode No. 7 in combination with large-sized particles (HAp+Ag), which did not ensure their complete melting. In addition, an increased spraying distance caused premature cooling of the particle surface outside the microplasma jet zone and partial solidification of the liquid phase, resulting in a small amount of liquid phase remaining on the surface of the substrate (Figure 3, mode No. 7).

At mode No. 2, on the contrary, the formation of overheated splats with a characteristic presence of a liquid phase in the form of droplets around them was observed. This is explained by a combination of MPS parameters: high value of current (45 A), minimum spraying distance (80 mm) and relatively small particle size (50 μm).

The least overheated were the splats obtained under the parameters of mode 6, where the current was 35 A, the plasma-forming gas flow rate was 2 l/min, the distance was 80 mm, and the particle size was 90 μm. Under such conditions, the temperature of the microplasma jet was lower, which reduced the probability of overheating, and larger particles were exposed to less acceleration and deformation, forming disc-shaped splats.

It is known that the shape of the splat directly affects the adhesion of the coating. For thermal methods of application, three bonding mechanisms are implemented: chemical, physical and mechanical, with the latter dominating [25–28]. Since the splat is the elementary unit of the layer build-up, the quality of its adhesion to the substrate determines the adhesive strength of the entire coating. The central disc-shaped part of the splat should be in close contact with the substrate, which is facilitated by the perpendicular action of the dynamic pressure of the particle. In contrast, splashes and fragments that fly parallel to the surface are less well adhered and can become a "weak link" in the coating structure.

Intensive heating of HAp particles in a plasma jet and their subsequent rapid cooling at the substrate provoke structural and phase transformations: dehydroxylated phases (oxyhydroxyapatite — OHAp, tricalcium phosphate — TCP, tetracalcium phosphate — TTCP) and amorphous calcium phosphate (ACP) [29]. Since the rate of resorption of these phases in the physiological environment exceeds that of stoichiometric HAp, their excess can lead to premature degradation of the coating and impaired osseointegration [30].

A number of studies (C. Yang, B. Weng, E. Chang, J. Wu) [31] has shown that the key factor in the formation of the phase composition is the heat content of the plasma jet and the thermal conductivity of the plasma-forming gas. The use of Ar/H_2 or Ar/He mixtures dramatically increases the thermal conductivity of the plasma and the temperature gradient in the particle, which enhances phase decomposition [32]. Thus, the Bio (Bi) criterion for oxide ceramics in Ar-plasma is 0.04–0.10, while in H_2-plasma it increases to 1.2–3.5 [33], indicating minimal temperature differences in Ar-plasma conditions. The negative effect of hydrogen has been confirmed experimentally [34]. Thus, the use of pure argon in microplasma spraying provides more favourable thermal conditions to reduce particle overheating and the degree of their decomposition, as well as promotes the formation of thicker splats and reduces amorphization. This opens up the

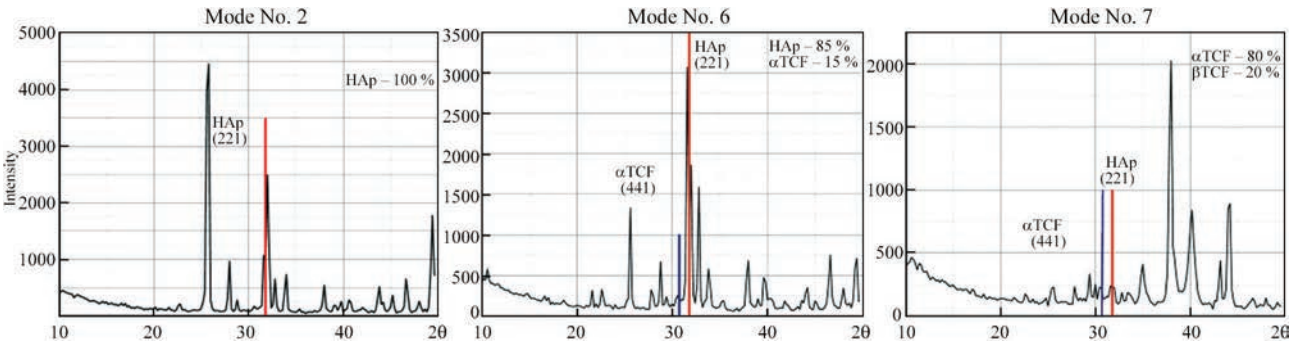

Figure 4. X-ray diffraction patterns of HAp+Ag coatings for MPS spraying modes Nos 2, 6 and 7 according to Table 1

possibility of regulating the phase composition and optimizing the bioactivity of coatings.

Therefore, the core challenge in developing optimal coatings is to achieve a balance between biocompatibility, which is ensured by the high crystallinity of stoichiometric HAp, and improved mechanical properties associated with the presence of a controlled amount of amorphous phase (usually 10–15 %) [35].

Figure 4 shows the results of X-ray diffraction studies of the produced coatings. The X-ray diffraction patterns for the specimen produced at mode 2 shows that the coating consists of single-phase crystalline hydroxyapatite. The intense and narrow diffraction maxima correspond to the reference data for the hexagonal structure of HAp. No extraneous crystalline phases, including thermal dissociation products, were detected. The high intensity of the peaks and the low background level indicate a high degree of crystallinity of the produced coating.

A high intensity of the (00_2)/(002) reflex (approximately $2\theta \approx 25.8–26°$), which is higher than the usually strongest reflex of approximately ≈ 31.7–32° (211) according to the standard data sheet for HAp, can be explained by the preferred orientation of the crystallites (texture), when the crystallites are oriented so that their *c*-axis is parallel to the coating surface, then the (001)-reflexes (especially (002) are enhanced relative to random powder.

A slight shift of the peaks to the right at 2θ means that the crystalline lattice has contracted, i.e. it has become more compact in the direction given by this reflex. Most probably, this means the loss of OH^- with the formation of oxyhydroxyapatite, which changes the parameters and leads to a reduction in *d* in certain directions.

Thus, according to the obtained diffraction pattern, spraying mode 2 ensured the preservation of the hydroxyapatite structure. It became possible due to the short interaction time of the particles with the microplasma jet, which is predetermined by the short spraying distance, high consumption of plasma-forming gas, and intense jet leakage. A small size of the particles contributed to their rapid acceleration, reaching high velocity and deposition rates on the substrate surface in a minimum period of time. In turn, a high value of the current ensured their complete melting and adhering on the substrate. The combination of these conditions made it possible to form a coating of single-phase crystalline hydroxyapatite.

The analysis of the X-ray diffraction pattern of the specimen formed at mode 6 showed that the coating has two-phase crystalline hydroxyapatite as the main phase (85 %) and α-tricalcium phosphate (α-TCP) in the amount of 15 %. All available peaks are sharp and clearly pronounced, indicating a high degree of crystallinity of both phases in the coating composition. The background peaks in the region of small angles (10–25°) are insignificant, indicating a small amount of amorphous component. The formation of a bioresorbable α-TCP phase occurred as a result of a partial thermal dissociation of the original HAp powder under microplasma jet conditions. The produced two-phase coating with a high degree of crystallinity is perspective for the application in implantology due to the combination of a stable HAp substrate and a bioactive, more soluble α-TCF phase, but its presence may further lead to a decrease in coating stability.

The two-phase composition of the specimen coating formed at mode 6 is explained by a number of factors. A large size of the powder particles caused their lower acceleration in the microplasma jet, which prolonged their stay in the high-temperature zone and ensured gradual heating until complete melting, despite the minimum current values and lower jet temperature. The use of a small spraying distance reduced the risk of solidification of the surface layer of the melt, which contributed to adhering of particles in the process of coating formation in a completely molten state with minimal deformation and ensured the preservation of a significant fraction of the hydroxyapatite crystalline phase.

According to the X-ray diffraction pattern of the specimen with coating formed at mode 7, it was found that the thermal effect of the microplasma jet is characterized by the minimum value of the current, the

Table 2. Elemental composition of Zr-HAp+Ag coating

Results in mass values, %									
Spectrum number	C	O	Si	P	Ca	Zr	Ag	Nb	Total
Spectrum 1	9.94	43.48	1.29	15.41	29.14	–	0.75	–	100
Spectrum 2	–	5.14	–	–	–	91	–	3.86	100

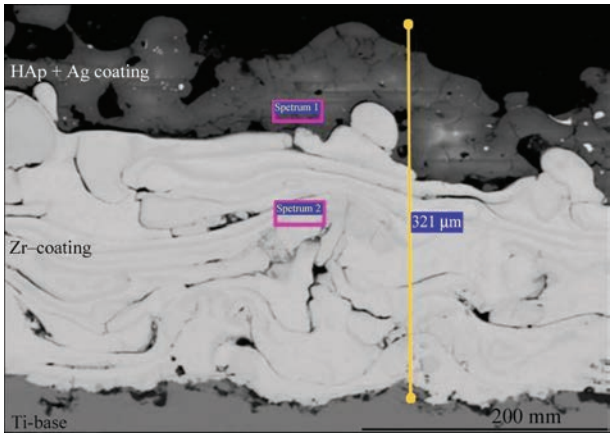

Figure 5. SEM image of the microstructure of the Zr-HAp+Ag coating with indicated areas of energy dispersive X-ray spectroscopy research

largest spraying distance, and the use of large-sized particles, which led to the melting of only their surface layer. Such particles bounced off the substrate without a sufficient amount of liquid phase. Thus, the coating was formed from a liquid surface layer, whose phase composition is about 80 % of α-TCF and 20 % of β-TCF. The presence of a pronounced halo in the diffraction pattern confirms the presence of the amorphous phase (AP). It is known that hydroxyapatite coatings containing a certain fraction of amorphous calcium phosphate are characterized by increased strength and wear resistance compared to their fully crystalline analogues [36]. In addition, the controlled dissolution of AP in the physiological environment can contribute to the accelerated release of Ca^{2+} and PO_4^{3-} ions, which in turn stimulates bone growth in the early stages of implantation. However, this process can also lead to accelerated degradation of the coating [37]. Thus, the spraying conditions at mode 7 ensure the formation of fully bioresorbable coatings consisting exclusively of various polymorphic modifications of tricalcium phosphate.

Work [38] demonstrated the effectiveness of the microplasma spraying method in the creation of biocompatible metal-ceramic two-layer coatings consisting of a zirconium sublayer (Zr) and an upper layer of HAp intended for application to the surface of titanium alloy implants. Adhesion tests have shown that the Zr-HAp two-layer coating demonstrates an adhesion strength of 28.0 ± 4.2 MPa, which exceeds the minimum permissible value of –15 MPa (according to ISO 13779-2), confirming an effective mechanical integration with the substrate. Biological studies have shown that the composition of the coating affects the proliferation of mesenchymal stem cells, which underscores the key role of chemical composition and surface topography in regulating the cellular response. Based on the above results of hydroxyapatite coating (spraying mode 2), a two-layer Zr-HAp+Ag coating was formed using zirconium as a sublayer. The microstructure of the produced coating is shown in Figure 5.

The results of the energy dispersive X-ray spectroscopy analysis (Table 2) confirm the chemical composition of the system consisting of a Zr-based sublayer and a HAp+Ag coating. The research also revealed that during the formation of coatings by the MPS method, the silver concentration decreases from 2 % to 0.75 %. This is explained by the evaporation of active silver particles that are part of the HAp powder structure.

The study of the antibacterial properties of HAp+Ag coatings produced by the MPS method against the pathogens Pseudomonas aeruginosa, Staphylococcus aureus and Escherichia coli showed that the quantity of viable cells of the tested microorganisms after exposure for 45 min (in % of the reference specimen) was as follows:

- E. coli (Escherichia coli) 0 %;
- S. aureus (Staphylococcus aureus) 46.6;
- P. aeruginosa (Pseudomonas aeruginosa) 39.5 %.

Thus, it can be concluded that silver-doped hydroxyapatite coatings produced by the MPS method retain pronounced antibacterial properties despite exposure to high temperatures. This indicates their potential for preventing bacterial complications on the surfaces of titanium implants in the early stages after implantation.

CONCLUSIONS

1. Due to the low power of the microplasma jet and the use of pure argon as a plasma-forming gas, microplasma spraying allows the formation of bioceramic coatings from silver-doped hydroxyapatite with minimal risk of overheating of the substrate and decomposition of the material to be sprayed, compared to conventional plasma arc spraying.

2. It is proved that the phase composition of coatings can be regulated by optimizing the microplasma spraying modes, which allows minimizing the formation of undesirable phases (TCF, TTCF, CaO) and achieves the optimal ratio of crystalline and amorphous components.

3. According to the analysis of diffraction patterns of hydroxyapatite coatings, mode 2 with the following technological parameters of microplasma spraying: current — 45 A, plasma-forming gas flow rate — 2 l/min, spraying distance — 80 mm, powder fraction — 50 μm, ensures the preservation of the single-phase crystalline structure of hydroxyapatite in the coating and can be recommended for its production.

4. The antibacterial properties of HAp+Ag coatings were confirmed on pathogens: with complete inhibition of E. coli growth (up to 0 %) and a significant decrease in the viability of S. aureus (up to 46.6 %) and P. aeruginosa (up to 39.5 %), which indicates the feasibility of using such coatings to prevent infectious complications after implantation.

5. The microplasma spraying method is an economical and versatile technology suitable for applying coatings at mass production of small titanium implants or those with complex geometries with specified biocompatible and antibacterial properties.

The published results were obtained within the framework of the project "Development of innovative biocompatible antibacterial coatings and technology for their application to orthopaedic implants for use in the treatment of injuries in military personnel and civilians", with the grant support of the National Research Foundation of Ukraine within the framework of the competition "Science for Strengthening Ukraine's Defence Capability" under contract No. 032/0070 of 03.03.2025.

ACKNOWLEDGEMENTS

The authors would like to express their sincere gratitude to Yaroslav Stelmakh and Valeriy Demchenko for their valuable assistance in conducting XRD studies of the coating surface and studying their microstructure by SEM, which made a significant contribution to the analysis of the coating characteristics in this research work.

REFERENCES

1. Eliaz, N., Metoki-Shlubsky, N. (2017) Calcium phosphate bioceramics: A review of their history, structure, properties, coating technologies and biomedical applications. *Materials,* 10(**4**), 334. DOI: https://doi.org/10.3390/ma10040334
2. Heimann, R.B. (2024) Plasma-sprayed osseoconductive hydroxylapatite coatings for endoprosthetic hip implants: Phase composition, microstructure, properties, and biomedical functions. *Coatings,* 14(**7**), 787. DOI: https://doi.org/10.3390/coatings14070787
3. Gupta, T.T., et al. (2020) Staphylococcus aureus aggregates on orthopedic materials under varying levels of shear stress. *Applied and Environmental Microbiology,* 86(**19**). DOI: https://doi.org/10.1128/aem.01234-20
4. Godoy-Gallardo, M., Eckhard, U., Delgado, L.M. et al. (2021) Antibacterial approaches in tissue engineering using metal ions and nanoparticles: From mechanisms to applications. *Bioactive Materials,* 6(**12**), 4470–4490. DOI: https://doi.org/10.1016/j.bioactmat.2021.04.033
5. Dube, E., Okuthe, G.E. (2025) Silver nanoparticle-based antimicrobial coatings: sustainable strategies for microbial contamination control. *Microbiology Research,* 16(**6**), 110. DOI: https://doi.org/10.3390/microbiolres16060110
6. Rios-Pimentel, F.F., Méndez-González, M.M., García-Rocha, M. (2023) A short review: hydroxyapatite coatings for metallic implants. *Heat Treatment and Surface Engineering, 5*(**1**). DOI: https://doi.org/10.1080/25787616.2023.2202002
7. Bansal, G., Gautam, R., Misra, J., Mishra, A. (2023) Coating methods for hydroxyapatite — A Bioceramic Material. *Bioceramics*. Springer. DOI: https://doi.org/10.1007/978-981-99-3549-9_13
8. Su, Y., Cockerill, I., Zheng, Y. et al. (2019) Biofunctionalization of metallic implants by calcium phosphate coatings. *Bioactive Materials,* **4**, 196–206. DOI: https://doi.org/10.1016/j.bioactmat.2019.05.001
9. Sun, L. (2018) Thermal spray coatings on orthopedic devices: When and how the FDA reviews your coatings. *J. of Thermal Spray Technology,* **27**, 1160–1171. DOI: https://doi.org/10.1007/s11666-018-0759-2
10. Mohseni, E., Zalnezhad, E., Bushroa, A.R. (2014) Comparative investigation on the adhesion of hydroxyapatite coating on Ti–6Al–4V implant: A review paper. *Inter. J. of Adhesion and Adhesives,* **48**, 238–257. DOI: https://doi.org/10.1016/j.ijadhadh.2013.09.030
11. Khor, K.A., Li, H., Cheang, P. (2004) Significance of melt-fraction in HVOF sprayed hydroxyapatite particles, splats and coatings. *Biomaterials,* 25(**7–8**), 1177–1186. DOI: https://doi.org/10.1016/j.biomaterials.2003.08.008
12. Alontseva, D., Azamatov, B., Safarova, Y. et al. (2023) A brief review of current trends in the additive manufacturing of orthopedic implants with thermal plasma-sprayed coatings. *Coatings,* 13(**7**), 1175. DOI: https://doi.org/10.3390/coatings13071175
13. Weiss, S., Alontseva, D., Safarova, Y. et al. (2025) Microplasma-sprayed titanium and hydroxyapatite coatings on Ti6Al4V Alloy: In vitro biocompatibility and corrosion resistance: Pt I. *Johnson Matthey Technology Review,* **69**. DOI: https://doi.org/10.1595/205651325X17201903387613
14. Alontseva, D., Safarova, Y., Voinarovych, S. et al. (2024) Biocompatibility and corrosion of microplasma-sprayed titanium and tantalum coatings. *Coatings,* 14(**2**), 206. DOI: https://doi.org/10.3390/coatings14020206
15. Borisov, Yu.S., Borisova, A.L., Tunik, A.Yu. et al. (2008) Effect of microplasma spraying parameters on structure, phase composition and texture of hydroxyapatite coatings. *The Paton Welding J.*, **4**, 10–15.
16. Cizek, J., Khor, K.A. (2012) Role of in-flight temperature and velocity of powder particles on plasma sprayed hydroxyapatite coating characteristics. *Surf. and Coat. Technol.,* 206(**8–9**), 2181–2191. DOI: https://doi.org/10.1016/j.surfcoat.2011.09.058
17. Dyshlovenko, S., Pawlowski, L., Roussel, P., et al. (2006) Relationship between plasma spray parameters and microcracking of hydroxyapatite coatings. *Surf. and Coat. Technol.,* 200(**20–21**), 3845–3855. DOI: https://doi.org/10.1016/j.surfcoat.2004.11.037

18. Gu, Y.W., Khor, K.A., Cheang, P. (2003) In vitro studies of plasma-sprayed hydroxyapatite/Ti-6Al-4V composite coatings in simulated body fluid. *Biomaterials,* 24(**9**), 1603–1611. DOI: https://doi.org/10.1016/s0142-9612(02)00573-2
19. Bolelli, G., Sabiruddin, K., Lusvarghi, L. et al. (2010) FIB assisted study of plasma sprayed splat-substrate interfaces. *Surf. and Coat. Technol.,* 205(**2**), 363–371. https://doi.org/10.1016/j.surfcoat.2010.06.057
20. Fukumoto, M., Hayashi, H., Yokoyama, T. (1995) Relationship between particle's splat pattern and coating adhesive strength of HVOF sprayed Cu-alloy. *J. of Japan Thermal Spraying Society,* 2(**3**), 149–156.
21. Yushenko, V. et al. (2006) Plasmatron for spraying of coatings. WO2004010747A1 – Google Patents.
22. Alontseva, D., Ghassemieh, E., Voinarovych, S. et al. (2019) Manufacturing and characterization of robot assisted microplasma multilayer coating of titanium implants. *Johnson Matthey Technology Review*, **64**, 157–167. DOI: https://doi.org/10.1595/205651320x15737283268284
23. Dyshlovenko, S., Pateyron, B., Pawlowski, L., Murano D. (2004). Numerical simulation of hydroxyapatite powder behaviour in plasma jet. *Surf. and Coat. Technol.,* 179(**1**), 110–117. DOI: https://doi.org/10.1016/S0257-8972(03)00890-9
24. *Morks M.F., Kobayashi A.* (2007). Influence of spray parameters on the microstructure and mechanical properties of gas-tunnel plasma sprayed hydroxyapatite coatings. *Mater. Sci. and Eng.: B.*, 139(**2–3**), 209–215. DOI: https://doi.org/10.1016/j.mseb.2007.02.008
25. Brossard, S., Munroe, P.R., Tran, A.T.T., Hyland, M.M. (2010) Study of the effects of surface chemistry on splat formation for plasma sprayed NiCr onto stainless steel substrates, *Surf. and Coat. Technol.*, 204(**9–10**), 1599–1607, 2-s2.0-71049164591. DOI: https://doi.org/10.1016/j.surfcoat.2009.10.008
26. Chandra, S., Fauchais, P., (2009) Formation of solid splats during thermal spray deposition, *J. of Thermal Spray Technology*, 18(**2**), 148–180, 2-s2.0-67349102724. DOI: https://doi.org/10.1007/s11666-009-9294-5
27. Xing, Y.Z., Li, C.J., (2009) Bonding characteristics of a plasma-sprayed Yttria-stabilized zirconia splat on a high-temperature substrate. In: *Proc. of the 4th Asian Thermal Spray Conference*, 285–288.
28. Fauchais, P. (2004) Understanding plasma spraying. *J. of Physics D: Applied Physics,* 37(**9**), R86–R108. DOI: https://doi.org/10.1088/0022-3727/37/9/R02
29. Heimann, R.B. (2016) Plasma-sprayed hydroxylapatite-based coatings: Chemical, mechanical, microstructural, and biomedical properties. *J. Therm. Spray Tech*., **25**, 827–850. DOI: https://doi.org/10.1007/s11666-016-0421-9
30. Klein, C.P.A.T., de Blieck-Hogervorst, J.M.A., Wolke, J.G.C., et al. (1990) Studies of the solubility of different calcium phosphate ceramic particles in vitro. *Biomaterials,* 11(**7**), 509–512. DOI: https://doi.org/10.1016/0142-9612(90)90067-z
31. Yang, C.Y., Wang, B.C., Chang, E., Wu, B.C. (1995) The influences of plasma spraying parameters on the characteristics of hydroxyapatite coatings: a quantitative study. *J. of Materials Sci.: Materials in Medicine,* 6(**4**), 249–257. DOI: https://doi.org/10.1007/bf00120267
32. Vardelle, A., Moreau, C., Themelis, N.J., et al. (2015) A perspective on plasma spray technology. *Plasma Chemistry and Plasma Processing,* 35(**3**), 491–509. DOI: https://doi.org/10.1007/s11090-014-9600-y
33. Borisov, Yu.S, Borisova, A.L. (1986) *Plasma powder coatings*. Kyiv, Tekhnika.
34. Dyshlovenko, S., Pawlowski, L., Roussel, P. (2005) Experimental investigation of influence of plasma spraying operational parameters on properties of hydroxyapatite. In: *Thermal Spray Connects: Explore its surfacing potential!* ASM International, 726–731.
35. Yang, Y., Kim, K.-H., Ong, J.L. (2005) A review on calcium phosphate coatings produced using a sputtering process — An alternative to plasma spraying. *Biomaterials,* 26(**3**), 327–337. DOI: https://doi.org/10.1016/j.biomaterials.2004.02.029
36. McPherson, R., Gane, N., Bastow, T.J. (1995) Structural characterization of plasma-sprayed hydroxyapatite coatings. *J. of Mater. Sci.: Materials in Medicine,* 6(**6**), 327–334.
37. LeGeros, R.Z. (2002) Properties of osteoconductive biomaterials: Calcium phosphates. *Clinical Orthopaedics and Related Research,* **395**, 81–98. DOI: https://doi.org/10.1097/00003086-200202000-00009
38. Voinarovych, S., Maksimov, S., Kaliuzhnyi, S. Et al. (2025) Functional assessment of microplasma-sprayed hydroxyapatite-zirconium bilayer coatings: Mechanical and biological perspectives. *Materials*, 18(**14**), 3405. DOI: https://doi.org/10.3390/ma18143405

ORCID

S.M. Kaliuzhnyi: 0000-0002-8132-3930,
S.Yu. Maksymov: 0000-0002-5788-0753,
S.G. Voinarovych: 0000-0002-4329-9255,
O.M. Kyslytsia:0000-0001-8894-4660,
N.V. Ulyanchich: 0000-0002-8806-0280,
V.V. Kolomiiets: 0000-0003-2322-7091,
V.M. Teplyuk: 0009-0009-9587-0327,
N.V. Prokhorenkova: 0000-0001-5987-6929

CONFLICT OF INTEREST

The Authors declare no conflict of interest

CORRESPONDING AUTHOR

S.G. Voinarovych
E.O. Paton Electric Welding Institute of the NASU
11 Kazymyr Malevych Str., 03150, Kyiv, Ukraine.
E-mail: serge.voy@gmail.com

SUGGESTED CITATION

S.M. Kaliuzhnyi, S.Yu. Maksymov,
S.G. Voinarovych, O.M. Kyslytsia, N.V. Ulyanchich,
V.V. Kolomiiets, V.M. Teplyuk,
N.V. Prokhorenkova (2025) Features of formation of biocompatible coatings from silver-doped hydroxyapatite powder by microplasma spraying. *The Paton Welding J*., **12**, 27–34.
DOI: https://doi.org/10.37434/tpwj2025.12.04

JOURNAL HOME PAGE

https://patonpublishinghouse.com/eng/journals/tpwj

Received: 03.10.2025
Received in revised form: 18.10.2025
Accepted: 24.12.2025

DOI: https://doi.org/10.37434/tpwj2025.12.05

STRUCTURE AND MECHANICAL PROPERTIES OF DEFORMED SEMI-FINISHED PRODUCTS MADE OF VT8 ALLOY PRODUCED BY ELECTRON BEAM MELTING

S.V. Akhonin[1], V.O. Berezos[1], O.G. Yerokhin[1], A.Yu. Severin[1], T.O. Mitina[1], V.A. Kryzhanovskyi[2]

[1]E.O. Paton Electric Welding Institute of the NASU
11 Kazymyr Malevych Str., 03150, Kyiv, Ukraine
[2]LLC "NVO Khvylia"
44/1 Naberezhna Peremohy Str., 49094, Dnipro, Ukraine

ABSTRACT

A comprehensive study was carried out to assess the quality of deformed semi-finished products manufactured from an ingot of the VT8 titanium alloy. Using electron beam remelting technology, 400-mm-diameter ingots were produced, from which semi-finished products in the form of hot-forged bars of 200 mm in diameter and disks of 440×145 mm were fabricated. The paper presents the results of investigations of the structure and mechanical properties of the obtained semi-finished products. It is shown that the metal of the produced ingots and deformed semi-finished products meets the requirements of the applicable standards.

KEYWORDS: *electron beam melting, heat-resistant titanium alloy, ingot, chemical composition, structure, deformation, mechanical properties*

INTRODUCTION

The modern development of high-tech industries — primarily aviation, aerospace, and energy imposes increased requirements on the structural materials used. Under these conditions, such characteristics as high specific strength, thermal and corrosion resistance, manufacturability during processing, and resistance to prolonged loading at elevated temperatures are of critical importance. Among the variety of lightweight structural alloys, titanium alloys occupy a special place due to their successful combination of these properties [1].

RELEVANCE AND PURPOSE OF THE STUDY

The VT8 alloy belongs to the group of two-phase (α+β) titanium alloys of martensitic type [2, 3] and is a titanium-based composition alloyed with aluminium and molybdenum. The alloy is produced in the form of forgings, stampings, bars, and plates, and is used for critical components operating under elevated temperatures and loads. In the annealed condition, VT8 can operate for long periods (over 6000 h) at temperatures up to 500 °C. In the heat-strengthened condition (quenching followed by aging), the alloy withstands operation at temperatures up to 450 °C, and under short-term exposure up to 100 h — at 500 °C [3]. It exhibits good weldability, corrosion resistance, and high mechanical properties at temperatures up to 450 °C. Due to its balanced phase composition and the ability to obtain a stable structure under various deformation and heat-treatment modes, VT8 alloy has found wide application in aircraft manufacturing, power engineering, and pipeline fittings production [4].

A key factor determining the quality characteristics of the metal is the method of its melting. The high chemical activity of titanium at elevated temperatures makes its production impossible under ordinary atmospheric conditions, as titanium becomes saturated with gases (O, N, H), forms chemical compounds, and becomes brittle. Therefore, industrial production of titanium alloys is carried out using special electrometallurgical methods: vacuum arc remelting (VAR), vacuum induction melting (VIM), plasma melting, and electron beam melting (EBM) [5].

The most widely used method remains VAR, which makes it possible to obtain large ingots of satisfactory quality. However, VAR has several drawbacks: the presence of liquation zones, nonuniform distribution of alloying elements, and porosity in the central regions of the ingot. All these factors necessitate triple remelting, as required by aviation standards. These limitations are particularly critical in the production of critical components, where microdefects can significantly affect service performance [6].

EBM, in contrast, ensures a higher level of purity and structural homogeneity of the metal. This method uses a high-energy-density electron beam focused on the surface of the metal under vacuum conditions. Melting occurs without contact with refractory materials, thereby eliminating contamination of the melt. Due to the use of an cold hearth, it becomes possible to remove dense nonmetallic inclusions through sed-

Figure 1. Batch of 400-mm-diameter VT8 titanium alloy ingots produced by EBM

imentation and to achieve more complete homogenization of the melt [7].

Ingots produced by EBM with an cold hearth are characterized by a directed macrostructure and a minimal content of residual impurities. This significantly improves the reproducibility of properties in finished products, increases component service life, and reduces the probability of sudden failures. Studies show that titanium alloys produced using this technology demonstrate improved fatigue strength, especially under cyclic loading at elevated temperatures [8].

Thus, the choice of melting technique has a decisive influence on the quality of the final semi-finished product. EBM with an cold hearth has increasingly been considered in recent years as the most promising technology for producing titanium alloys intended for critical applications.

Considering the need to increase the reliability of structures and the competitiveness of domestic materials on the international market, the study of the specifics of EBM technology and the properties of VT8 alloy produced by this method is both relevant and important.

Therefore, the purpose of this work was to investigate the structure and properties of VT8 alloy ingots produced by EBM and the deformed semi-finished products manufactured from them in order to confirm that the material meets the requirements of applicable standards.

EQUIPMENT AND RESEARCH PROCEDURE

To improve the manufacturing technology of high-temperature titanium alloy ingots, the E.O. Paton Electric Welding Institute of the NAS of Ukraine (PWI) carried out a series of melts to produce VT8 alloy ingots with a diameter of 400 mm. The ingots were produced using EBM with an cold hearth and batch feeding of liquid metal into a water-cooled mold.

As charge materials, titanium sponge grade TG-120 and alloying elements in the form of aluminium chips, molybdenum bar, and metallic silicon were used.

Using previously established and optimized modes of electron beam heating of the ingot in the mold on the UE-5812 EBM unit [9], experimental melts were performed to produce VT8 titanium alloy ingots. During the experimental melts, the following technological parameters were maintained constant according to the optimal melting modes: melting rate; time between the pouring of batches; and the height of the batches simultaneously poured into the mold (see technical specifications).

Technical parameters of the EBM process for a 400-mm-diameter VT8 alloy ingot

Melting rate, kg/h	270
Time interval between batch pouring, s	60
Height of batches simultaneously poured into the mold, mm	8
Power of the first gun (central heating), kW	50
Power of the second gun (peripheral heating), kW	70

As a result of the experimental melts, a batch of 400-mm-diameter VT8 alloy ingots was produced (Figure 1).

The distribution of alloying elements and impurities in the cast ingots was determined (Table 1). Chemical composition control of the produced ingots was carried out using a SPECTROPORT optical emission spectrometer. The gas content was measured using LECO gas analyzers TC-436 and RH-2. It was established that the chemical composition of the ingots corresponds to the standard composition of the VT8 alloy.

The detection of inhomogeneities in the metal was carried out using non-destructive ultrasonic testing with a UD4-76 flaw detector. Ultrasonic inspection of the VT8 titanium alloy ingots showed that defects

Table 1. Distribution of alloying elements and impurities along the length of a 400-mm-diameter ingot of VT8 titanium alloy produced by EBM, wt.%

Sampling location	Al	Mo	Fe	Si	C	O	N	H
Top	6.3	3.0	0.07	0.21	0.016	0.10	0.02	0.002
Middle	6.4	3.2	0.08	0.22				
Bottom	6.1			0.21	0.015	0.11		
GOST 19807–91	5.8–7.0	2.8–3.8	<0.30	0.2–0.4	<0.10	<0.15	<0.05	<0.015

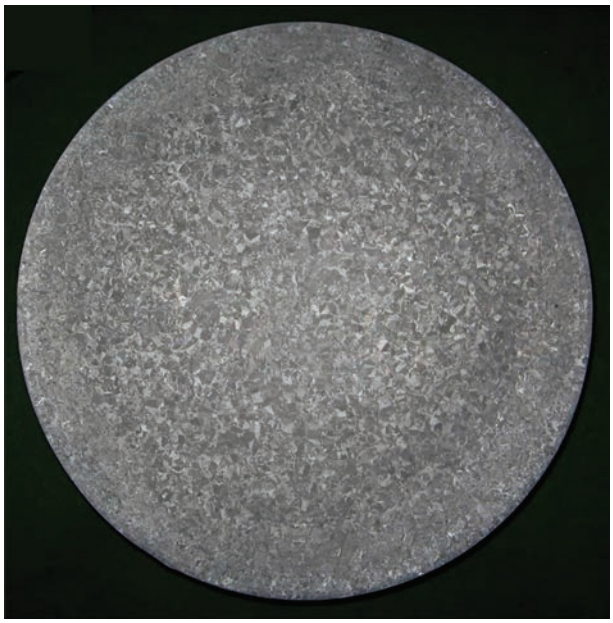

Figure 2. Macrostructure of a 400-mm-diameter ingot of VT8 titanium alloy in transverse cross-section

such as pores, shrinkage cavities, structural inhomogeneities, and nonmetallic inclusions were absent.

The ingot macrostructure was examined on a template prepared from the transverse cross-section of the ingot (Figure 2).

Visual examination showed that the macrostructure of the ingot contained no cracks, looseness, metallic or nonmetallic inclusions, or other defects. The macrostructure of the central region of the 400-mm-diameter ingot on the transverse template was dense and uniform, without differentiated zones. No significant differences were observed between the structure of the central and peripheral regions of the ingot. The macrograin size, determined according to the standard 10-point macrostructure scale, corresponded to points 8–9.

The VT8 alloy ingots produced by EBM were subjected to forging. Bars with a diameter of 200 mm were forged directly from the 400-mm EBM ingot. The forging of VT8 alloy ingots was performed according to industrial technology (Table 2), starting at 1100 °C in the β-phase region and finishing at 900 °C in the α+β region. As a result of deformation processing, 200-mm bars were manufactured.

Figure 4. Forged discs 440×145 mm made of VT8 titanium alloy

The machined bars, upon visual inspection, showed no surface cracks, delaminations, inclusions, liquation-type areas, or other defects (Figure 3).

Additionally, work was carried out to produce forged discs with a diameter of 440 mm from the experimental ingots. For this purpose, the 400-mm ingot was forged to an intermediate size, after which it was upset and forged into a disc-shaped billet with dimensions 440×145 mm (Figure 4).

To study the structure of forged billets from the 200-mm-diameter VT8 titanium alloy bar, a transverse template with a thickness of 10 mm was prepared. The macrostructure of the template was examined in two control zones (Figure 5).

Visual examination of the etched macrotemplates showed that no metallurgical or deformation-induced defects were present in the macrostructure. This condition of the macrostructure meets the requirements of the aviation standard, according to which cracks, delaminations, voids, films, metallic and nonmetallic

Figure 3. Forged bar with a diameter of 200 mm made of VT8 titanium alloy

Table 2. Forging temperature range of heat-resistant titanium alloy VT8

Alloy	Transformation temperature, °C	Ingot forging temperature, start (not higher)/finish (not lower), °C		Billet forging temperature, start (not higher)/finish (not lower), °C	
VT8	990	1100	900	1020	850

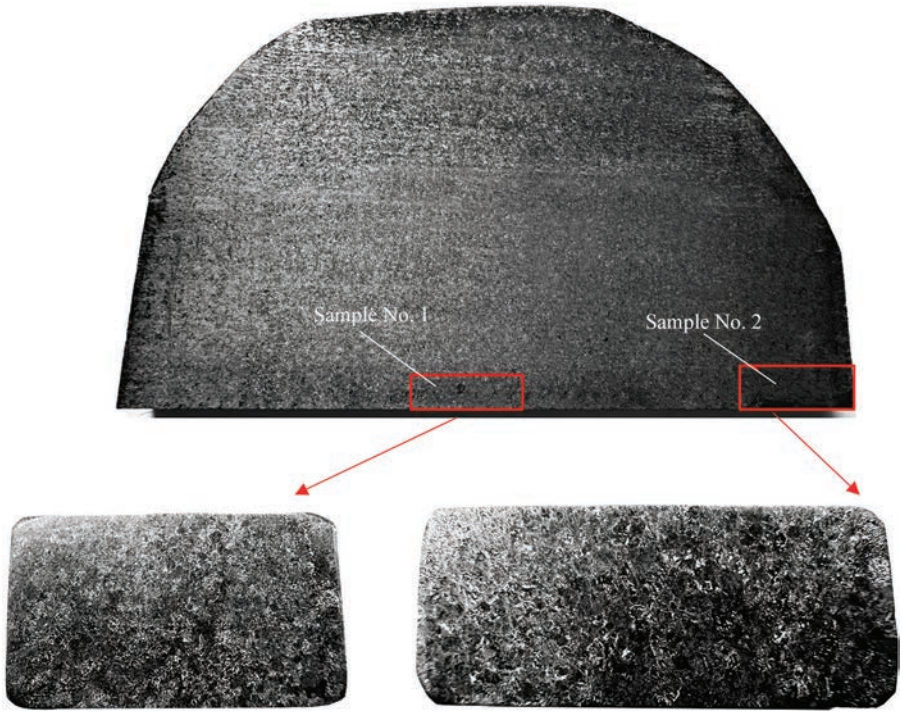

Figure 5. Macrostructure of a forged 200-mm-diameter bar of VT8 titanium alloy

inclusions detectable by the unaided eye are not permitted.

The macroscopic structure of the forged bar was characterized by a bright etched background and macrograins with clearly defined boundaries (see Figure 5). According to the standard 10-point scale for assessing the macrostructure of titanium alloys, the macrograin size corresponds to points 5–6.

Metallographic examination of the structure was carried out using a NEOPHOT-30 optical microscope. Microanalysis was performed on polished sections prepared in the transverse cross-section of the template, in various zones across its thickness.

The microstructures in different zones exhibit a similar character: the microstructure consists of β-transformed grains with a lamellar intragranular morphology of the α- and β-phases, with an α-phase fringe located along their boundaries. The β-transformed grains have a polyhedral shape, with sizes in the range of 250–600 μm. The thickness of the α-β-phases was 1–4 μm, and their length was 45–150 μm. According to the scale of acceptable microstructures for deformed semi-finished products made of α+β titanium alloys, individual massive regions of the α-phase are permissible and typically represent α-phase appearing in the plane of the polished section.

In certain areas, the microstructure can be classified as basket-weave type without an α-fringe along the grain boundaries, where α-β-phases are grouped into mutually intersecting packets.

Microstructures in the various zones of the examined template of the 200-mm-diameter bar are shown in Figure 6.

Mechanical testing was carried out on standard specimens cut out from templates of 200-mm-diameter bars (Table 3). The specimens for testing were cut

Table 3. Mechanical properties of 200-mm-diameter bars of VT8 alloy after forging

Sample No.	Tensile strength, kgf/mm²	Elongation, ε, %	Reduction of area, ψ, %	Impact toughness, kgf/mm²	Indentation diameter, mm
1	113.0	11.6	37.0	6.0	3.45
2		13.6	36.0	6.3	
OST 1 90107–73	95–120	≥8.0	≥21.0	≥3.0	3.2–3.7

Table 4. Mechanical properties of a 440-mm-diameter disk of VT8 alloy after forging

Sample No.	Tensile strength, kgf/mm²	Elongation, ε, %	Reduction of area, ψ, %	Tensile strength, kgf/mm²	Indentation diameter, mm	Hardness *HB*
1	114.5	12.0	27.5	114.5	3.40	321
2	111.0	10.0	26.0	6.0		331
OST 90000–70	100–120	≥9.0	≥25.0	≥3.0	3.2–3.7	–

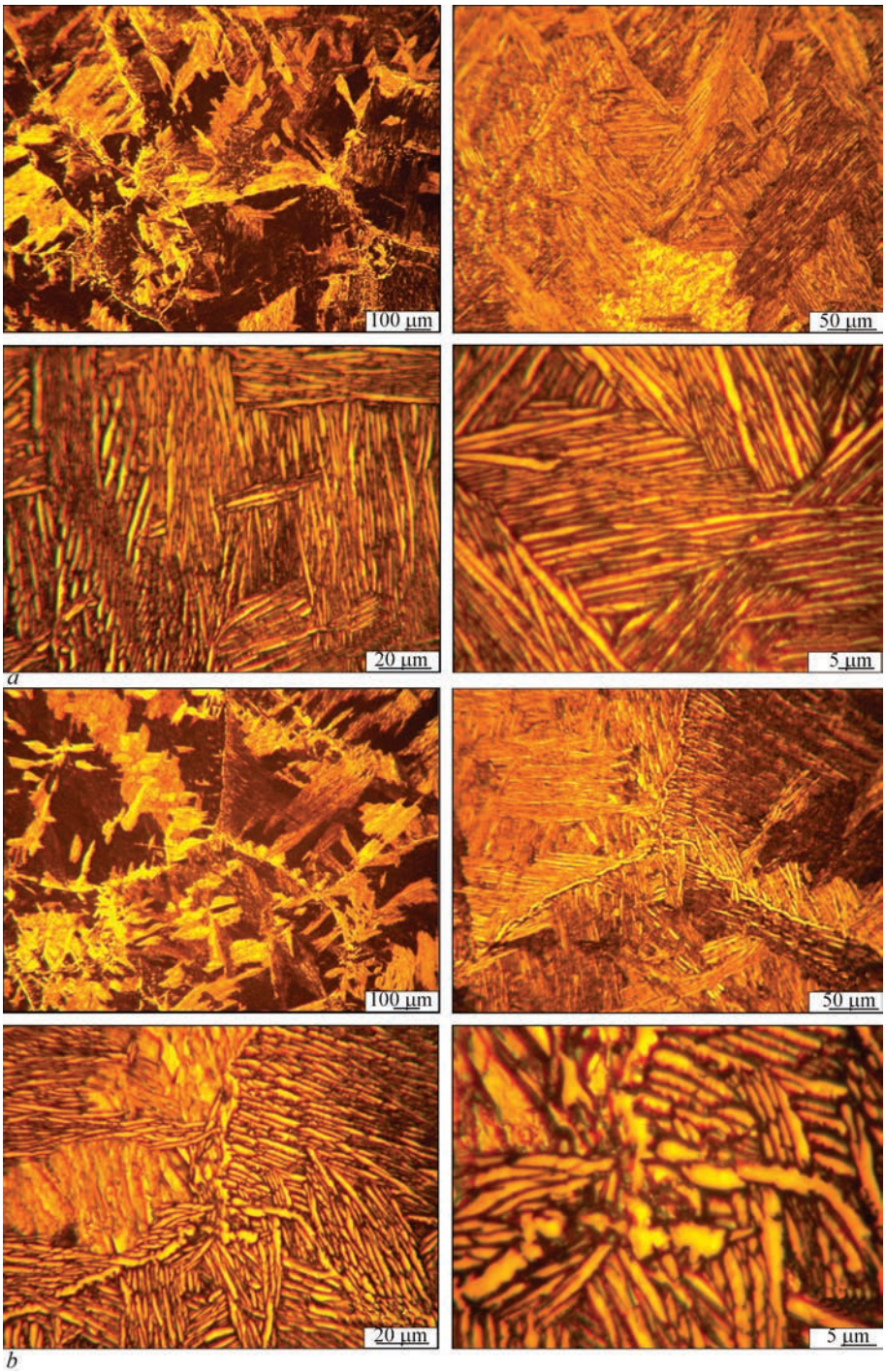

Figure 6. Typical microstructures of VT8 alloy in zone No. 1 (*a*) and zone No. 2 (*b*)

Table 5. Results of long-term heat resistance testing of VT8 alloy

Test temperature, °C	Tensile strength, kgf/mm^2	Long-term strength	
		Loading, kgf/mm^2	Test duration, h
500	63	54	52.5
	60	52	50.0

out closer to the central zone of the bar cross-section (at a distance of 1/4 from the center) and were subjected to heat treatment under the standard mode.

In addition, the mechanical properties of a forged VT8 alloy disk with dimensions 440×145 mm were examined (Table 4). To control the mechanical properties at elevated temperatures, bars were selected from the batch, from which specimens were cut out for determining ultimate strength and long-term strength (Table 5).

CONCLUSIONS

1. The comprehensive set of conducted studies demonstrated that the chemical composition of VT8 alloy ingots produced by EBCHM (electron-beam cold-hearth melting) and the mechanical properties of the semi-finished products in the form of forged bars and disks comply with the requirements of the standards (OST 1 90107–73, OST 90000–70).

2. Electron-beam melting is an effective method for obtaining high-quality ingots of heat-resistant titanium alloys from primary charge materials.

REFERENCES

1. Froes, F.H. (2015) *Titanium: Physical metallurgy, processing, and applications*. ASM International.
2. Arzamasov, B.N., Brostrem, V.A., Buche, N.A. et al. (1990) *Structural materials*: Refer. Book. Ed. by B.N. Arzamasov. Moscow, Mashinostroenie [in Russian].
3. Maslenkov, S.V., Maslenkova, E.A. (1991) *Steels and alloys for high temperatures*: Refer. Book. Book 2. Moscow, Metallurgiya [in Russian].
4. Lutjering, G., Williams, J. C. (2007) *Titanium*. Springer.
5. Leyens, C., Peters, M. (2003) *Titanium and titanium alloys: Fundamentals and applications*. Wiley-VCH.
6. Boyer, R., Welsch, G., Collings, E.W. (1994) *Materials properties handbook: Titanium alloys*. ASM International.
7. Gerdemann, S.J., White, J.C. (2002) Electron beam melting of titanium alloys. *J. of Materials Engineering and Performance*, 11(**3**), 303–309.
8. Semiatin, S.L., Bieler, T.R. (2001) The effect of α/β processing on the microstructure and texture of titanium alloys. *Metallurgical and Materials Transact. A*, 32(**5**), 1045–1057.
9. Trigub N.P., Zhuk G.V., Kornejchuk V.D. et al. (2007) Commercial electron beam installation UE-5812. *Advances in Electrometallurgy*, **1**, 9–11.

ORCID

S.V. Akhonin: 0000-0002-7746-2946,
V.O. Berezos: 0000-0002-5026-7366,
O.G. Yerokhin: 0000-0003-2105-5783,
A.Yu. Severin: 0000-0003-4768-2363,
T.O. Mitina: 0009-0005-3254-826X,
V.A. Kryzhanovskyi: 0000-0002-0917-8687

CONFLICT OF INTEREST

The Authors declare no conflict of interest

CORRESPONDING AUTHOR

V.O. Berezos
E.O. Paton Electric Welding Institute of the NASU
11 Kazymyr Malevych Str., 03150, Kyiv, Ukraine.
E-mail: titan.paton@gmail.com

SUGGESTED CITATION

S.V. Akhonin, V.O. Berezos, O.G. Yerokhin, A.Yu. Severin, T.O. Mitina, V.A. Kryzhanovskyi (2025) Structure and mechanical properties of deformed semi-finished products made of VT8 alloy produced by electron beam melting.
The Paton Welding J., **12**, 35–40.
DOI: https://doi.org/10.37434/tpwj2025.12.05

JOURNAL HOME PAGE

https://patonpublishinghouse.com/eng/journals/tpwj

Received: 10.07.2025
Received in revised form: 28.07.2025
Accepted: 16.12.2025

DOI: https://doi.org/10.37434/tpwj2025.12.06

RECYCLING OF NICKEL ALLOYS BY ELECTROSLAG REMELTING

Yu.V. Kostetskyi, V.P. Petrenko, E.O. Pedchenko, G.O. Polishko, V.A. Zaitsev

E.O. Paton Electric Welding Institute of the NASU
11 Kazymyr Malevych Str., 03150, Kyiv, Ukraine

ABSTRACT

The results of experiments on recycling nickel alloys by electroslag remelting (ESR) using a current-conducting mold are presented. The studies were carried out on the R-951 unit, where rational remelting parameters for consumable electrodes of variable cross-section made from nickel alloy waste were determined. The results confirmed the effectiveness of recycling production waste of EP648 nickel alloy by electroslag remelting with the use of a current-conducting mold. Optimal remelting modes for consumable electrodes of variable cross-section were established, ensuring process stability through rational power distribution between the electrode and the mold. The chemical composition of the obtained ingots met the standard requirements for EP648 alloy, and the products manufactured from them successfully passed quality control. The developed single-stage recycling technology enables direct return of nickel alloy waste into the production cycle and has high practical potential for industrial application. The research results may be used to improve existing methods of metal waste recycling and to develop new approaches to processing nickel alloys.

KEYWORDS: recycling, nickel alloy, electroslag remelting, two-circuit technology, current-conducting mold, ingot

INTRODUCTION

The concept of a circular economy encourages the metallurgical industry to reuse and more fully utilize technogenic waste with the aim of achieving zero waste production [1, 2]. This increases manufacturing competitiveness and promotes environmental sustainability by reducing the consumption of primary raw materials. The recycling of alloy steel and nickel-based alloy waste in Europe is an important component of green metallurgy, as the efficient return of alloy scrap into the production cycle significantly reduces energy and resource consumption [3, 4].

Among structural materials, steel and nickel alloys have substantial potential for repeated recycling and reuse [5]. Remelting of alloy scrap is typically performed in electric arc or induction furnaces [6, 7]. During melting, an important task is to minimize losses of valuable alloying elements, which is difficult to achieve under electric arc melting conditions [8]. Induction furnaces provide better assimilation of alloying elements and lower overall metal losses due to oxidation [7, 9]. However, under induction melting conditions, it is not possible to realize the refining capabilities of slags, and therefore to effectively remove undesirable impurities and nonmetallic inclusions from the metal melt. An additional problem of traditional methods for processing alloy scrap is the difficulty of obtaining high-quality ingots with a high level of physical and chemical homogeneity, as well as metal losses from cropping ingots and runners.

The quality of cast metal can be improved through the use of electroslag remelting (ESR) technology [7, 10–12]. The ESR process ensures effective removal of large nonmetallic inclusions, homogenization of the chemical composition throughout the ingot volume, improvement of the metal's micro- and macrostructure, and the production of dense ingots free of internal porosity and shrinkage cavities. At the same time, the chemical composition of the metal remains practically unchanged. ESR technology is widely used in industry to obtain high-quality ingots of critical applications from high-alloy steels and nickel-based alloys [10].

However, the direct integration of electroslag remelting technology into the traditional recycling chain of alloy steel and alloy waste is accompanied by additional costs, which limits its practical feasibility. To minimize production expenses, single-stage recycling processes based on electroslag technology have been proposed. These processes involve the use of nonconsumable electrodes and crucible-type electroslag melting [13, 14]. In the first variant, small scrap is loaded into the gap between the mold wall and the nonconsumable electrode. Under certain conditions, it is possible to use a consumable electrode of the same chemical composition as the scrap. However, this process has obvious limitations regarding the size of scrap fragments. Crucible electroslag melting offers greater flexibility in the allowable scrap size, but the metal accumulated in the melting crucible still needs to be poured into molds, which does not allow achieving ingot quality comparable to that of standard ESR.

A key limitation of using the canonical ESR process for recycling applications is the requirement to

use a consumable electrode with constant geometric parameters along its length [15]. This requirement is associated with the need to ensure process stability. For this purpose, specially manufactured cast or wrought electrodes are typically used. Evidently, implementing a single-stage recycling process based on classical ESR is extremely challenging.

The two-circuit electroslag remelting (ESR-TC) scheme developed at the E.O. Paton Electric Welding Institute of the NAS of Ukraine (PWI) [16, 17], which incorporates a current-conducting mold, relaxes the requirements for electrode geometry and expands the process capabilities for recycling applications. In this scheme, unlike the canonical process, electric current is supplied through two circuits simultaneously: consumable electrode–bottom plate and current-conducting mold–bottom plate (Figure 1). Consequently, the slag pool contacts two electrodes at once: the consumable electrode being remelted and the nonconsumable electrode, which is the mold component. The temperature regime at the periphery of the slag pool is determined by the nonconsumable electrode, enabling independent control of heat input into the slag and metal pools as well as the ingot buildup rate. Such control of the thermal balance is practically impossible in conventional ESR. The ESR-TC technology is successfully used for producing ingots from complex-alloyed steels, nickel-based superalloys, and titanium [18].

Studies have shown that during ESR with a current-conducting mold, the distribution of power between the supply circuits can vary within a wide range [16]. The use of an appropriate automatic control system of the process enables stable remelting of electrodes of variable geometry at a constant melting rate [19–21]. This simplifies the requirements and preparation of consumable electrodes for remelting and allows the recycling process to be implemented as a single-stage operation, producing a high-quality ingot directly by electroslag remelting of metallic waste.

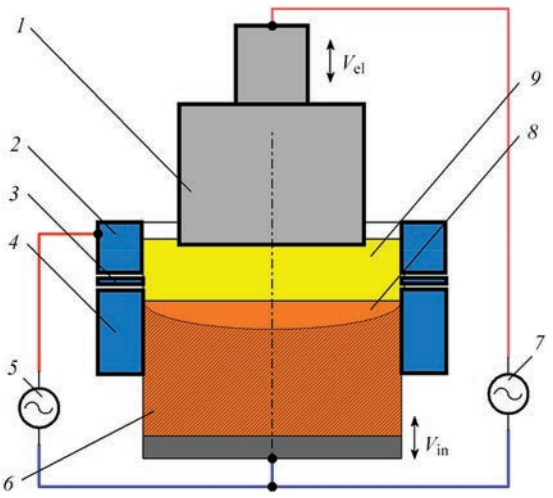

Figure 1. Schematic representation of ESR in a current-conducting mold with a two-circuit power supply scheme: *1* — consumable electrode; *2* — current-conducting section of the mold; *3* — insulating section of the mold; *4* — forming section of the mold; *5*, *7* — power sources; *6* — ingot; *8* — metal pool; *9* — slag pool

The present work presents the results of experimental studies on the recycling of technological waste of the EP648 nickel alloy using a single-stage scheme with the application of the ESR-TC technology with a current-conducting mold, yielding an ingot suitable for direct use in the production cycle after remelting.

EQUIPMENT, MATERIALS, AND RESEARCH METHODOLOGY

Experimental studies of the electroslag remelting of nickel alloy waste with the production of round ingots with a diameter of 180 mm were carried out in the Electroslag Technologies Laboratory of the PWI using an R-951 furnace equipped with a current-conducting mold and a downward ingot withdrawal scheme.

The furnace is equipped with two independent power sources with a capacity of 720 kVA each (transformers TShP-10000/1 (A-622)), upgraded for smooth regulation of the output voltage. The installed automatic control system provides the possibility to conduct the electroslag remelting process in an automatic mode with both liquid and solid start.

The electroslag remelting of the experimental material was performed in a short current-conducting mold with the forming section diameter of 180 mm (Figure 2, *a*). The mold had a sectional design (Figure 1): the upper section serves as a current-conducting (non-consumable) electrode, the lower section ensures high-quality formation of the ingot surface, and the insulating section prevents electrical breakdown between the current-conducting and forming parts.

A structural feature of the current-conducting section is a transverse slot filled with insulating material, which turns it into an open ring (Figure 2, *b*) [22]. Such a design, when the main melting current flows from the current-conducting section to the ingot, causes the appearance of a circular electric current $I_{circular}$ in the open ring and the corresponding magnetic field directed along the vertical axis of the mold (according to the right-hand rule). The current I_{mold}, which passes from the current-conducting section to the liquid metal pool, generates a magnetic field oriented perpendicular to the field of the circular current. The interaction of the electric and magnetic fields results in the appearance of the Ampère force, which induces rotational movement of the slag bath. This, in turn, intensifies heat transfer within it.

Consumable electrodes for electroslag remelting were formed from technological waste of EP648 nickel alloy of two types: cylindrical cut-offs with a

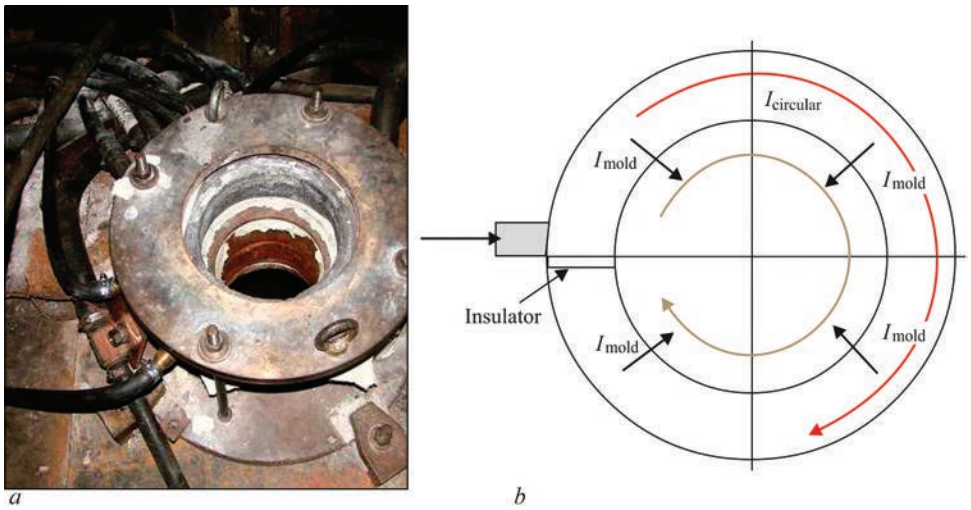

Figure 2. General view of the mold (*a*) and the scheme of electric current distribution in the current-conducting section and the direction of slag bath rotation (*b*)

diameter of 70 mm and a length of 160–210 mm, rejected due to shrinkage defects, and forged rings with diameters of 510 and 370 mm.

The standard chemical composition of the EP648 alloy is presented in Table 1. The results of selective incoming inspection of the chemical composition of the waste are presented in Table 2. Samples were taken from each batch of the incoming charge. The chemical composition was determined by spectral analysis.

Composite electrodes for electroslag remelting were assembled by welding individual fragments of the waste material. For this purpose, ENiCrMo-3 nickel-alloy welding wire was used, with a chemical composition close to that of the alloy being remelted. The consumption of welding material was limited to a minimum to reduce its influence on the chemical composition of the metal while ensuring sufficient joint strength considering the conditions of remelting.

Since the design of the composite electrodes does not allow the transmission of significant current, the remelting was performed using a quasi-passive electrode scheme. In this scheme, the main portion of the power is supplied through the circuit of the current-conducting mold.

The calculated productivity of the process Q_{melt} was determined using the empirical relation [23], kg/h:

$$Q_{melt} = kD_m,$$

where D_m is the mold diameter, mm, and k is an empirical coefficient, kg/(mm·h). According to industrial practice in steel remelting, the coefficient k is chosen within the range 0.4–0.8. Higher values are typical for low-alloy steels, while lower values correspond to high-alloy steels. In the case of nickel alloys, which have lower heat capacity compared to steels and a wider liquidus–solidus interval, the remelting process should be performed at the minimum possible productivity. Therefore, it is reasonable to use k = 0.4. Accordingly, for a mold with a forming section diameter of 180 mm, the recommended productivity is about 72 kg/h.

Typical slags for ESR of nickel alloys are based on the CaF_2–CaO–Al_2O_3 system, with the possible addition of other oxides such as SiO_2, MgO, and TiO_2, depending on the alloy composition. Titanium oxide is added to control the Al/Ti ratio in the metal and compensate for potential Ti losses. Silicon and magnesium oxides are introduced to adjust the physicochemical properties of the slag, particularly melting temperature

Table 1. Standard chemical composition of EP648 nickel alloy according to TU 14-1-4103–86, %

Al	Ti	Cr	Fe	Ni	Nb	Mo	W
0.5–1.1	0.5–1.1	32–35	≤4	Base	0.5–1.1	2.3–3.3	4.3–5.3

Table 2. Results of selective incoming inspection of the chemical composition of EP648 alloy scrap, %

Sample	Al	Ti	Cr	Fe	Ni	Nb	Mo	W
1	0.61	1.14	35.37	0.75	53.53	1.21	2.37	5.02
2	0.96	1.22	36.46		51.82	0.83	2.26	5.7
3	0.76	0.97	34.23	0.76	55.02	1.19	2.94	4.13
Average	0.78	1.11	35.35	0.75	53.46	1.08	2.52	4.95

Figure 3. Electroslag remelting process of the consumable electrode (*a*) and the external appearance of the obtained ingot (*b*)

and viscosity. At the same time, silica significantly influences the oxidizing potential of the slag, and therefore the degree of oxidation of aluminium and titanium in the metal during remelting. Thus, its concentration must be strictly controlled within the technological process. The negative effect of SiO_2 is reduced by lowering its activity through increasing slag basicity.

In this study, remelting was performed under a flux consisting of ANF-29 (Table 3) with the addition of pure CaF_2 in a 10:1 ratio.

To ensure stability of the chemical composition of the nickel alloy, slag from previous melts was reused in subsequent ones. It was assumed that the chemical composition of the slag during remelting evolves toward the equilibrium state. Slag for the second melt was taken from the first. To compensate for slag losses due to skull formation, pure CaF_2 was added in the amount of 500 g. Slag for the third melt was prepared from the slag of the second melt by adding 400 g of calcium fluoride.

Table 3. Chemical composition of ANF-29 flux according to TU U 20.5-00186520-126-2018, %

SiO_2	Al_2O_3	CaF_2	CaO	MgO	Fe_2O_3
10–15	13–17	37–45	24–30	2–6	<0.5

During remelting, in order to reduce the oxidative effect of atmospheric air, argon was supplied through an annular distributor into the melting zone at a flow rate of 15 l/min. Throughout the entire process, the slag bath was continuously deoxidized by adding metallic aluminium granules at an average feed rate of 3 g/min.

RESEARCH RESULTS AND DISCUSSION

During the first experiment (melt 1), a remelting of a single consumable electrode was carried out. The electrode was assembled from cylindrical cutoffs of the nickel alloy (Figure 3, *a*). The cylindrical fragments were joined by welding using seven welding electrodes with a diameter of 4 mm (amounting to 0.5 % of the total nickel alloy mass of 97 kg).

The melt was initiated using a liquid start. The total flux consumption amounted to 6 kg. The power supplied to the consumable electrode was maintained within the range of 40–50 kVA, while 150 kVA was delivered to the current-conducting section of the mold. Thus, the main portion of energy was introduced through the mold circuit, ensuring process stability. As a result of the remelting, a cylindrical ingot 490 mm in length was obtained (Figure 4, *b*). The average productivity of the process reached 80 kg/h.

A sample was taken from the heat part of the ingot to determine its chemical composition. The results of chemical analysis showed that the composition of the ingot metal corresponds to the standard composition of alloy EP648 (Table 4). The absolute percentage loss of the highly-active elements Al and Ti amounted to 0.11 and 0.15 %, respectively.

The experimental ingot was transferred to the production facility, where it was forged into rings of two size types (Figure 4). The manufactured rings were inspected according to the current production protocols for metallographic and ultrasonic testing. It was deter-

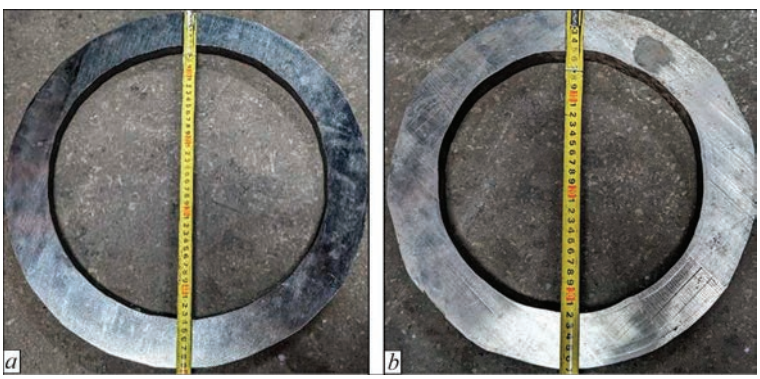

Figure 4. Forged rings from the ESR ingot with a diameter of 510 mm (*a*) and 370 mm (*b*)

Table 4. Chemical composition of the metal of the ESR ingot from the first melt, wt.%

Al	Ti	Cr	Fe	Ni	Nb	Mo	W
0.67	0.96	33.66	0.58	52.87	1.04	2.30	4.96

mined that the quality of the metal produced through recycling meets the requirements for alloy EP648-Sh according to GOST 22838–77.

The remaining ring segments that passed quality control but were not directed into further production, with a total weight of 27 kg, were used for repeated recycling. They were welded together into a single consumable electrode for subsequent electroslag remelting. Four consumable electrodes were manufactured from the remaining cylindrical cutoffs. One of them had a simplified design in the form of a long cylinder, while the others consisted of cylindrical fragments assembled in stacks of three at each level. The general appearance of the experimental electrodes prepared for remelting is shown in Figure 5, *a*.

At the second stage of the study, two melts (2 and 3) were carried out, resulting in ingots 1.1 and 1.25 m in length, respectively (Figure 5, *c*).

During melt 2, three electrodes of different designs were sequentially remelted; their appearance is shown in Figure 5, *a*. Electrode 1 consisted of cylindrical cutoffs welded together sequentially to form a cylindrical electrode. Electrode 2 was assembled from fragments of forged rings. Electrode 3 was formed from cylindrical cutoffs grouped into sets of three per level to increase the mold filling ratio. The diversity of consumable electrode designs within this melt made it possible to evaluate their remelting behavior and determine optimal approaches for forming electrodes from nickel-alloy scrap.

In Figure 5, *b*, the electroslag remelting process of electrode 2, assembled from forged ring fragments, is shown. This electrode design made it possible to verify the effectiveness of recycling waste pieces of complex shape and to evaluate the possibility of their remelting without loss of metal quality.

Figure 6 presents the parameter variation plots that illustrate the specific features of the melt progression. In particular, changes in the remelting modes are clearly observed depending on the melting stage and the electrode design (Table 5). Due to the increased filling ratio during the remelting of electrode 3, higher productivity was achieved compared to electrode 1, which was also assembled from cylindrical cutoffs (Table 5). At the same time, the plot clearly shows productivity jumps caused by transitions from one welded group of cylindrical fragments to the next, while the supplied power remained relatively stable. During the remelting of electrode 2 (Figure 5, *b*), assembled from ring fragments, productivity fluctuations were also observed, although without pronounced periodicity, which is explained by the specific characteristics of its construction. Meanwhile, it should be noted that due to the thermal inertia of the process and the sta-

Figure 5. General view of the electrodes prepared for melt 2 (*a*); electroslag remelting process of the electrode formed from ring remnants (*b*); ingots obtained after remelting the experimental electrodes, 1100 mm long (melt 2) and 1250 mm long (melt 3) (*c*)

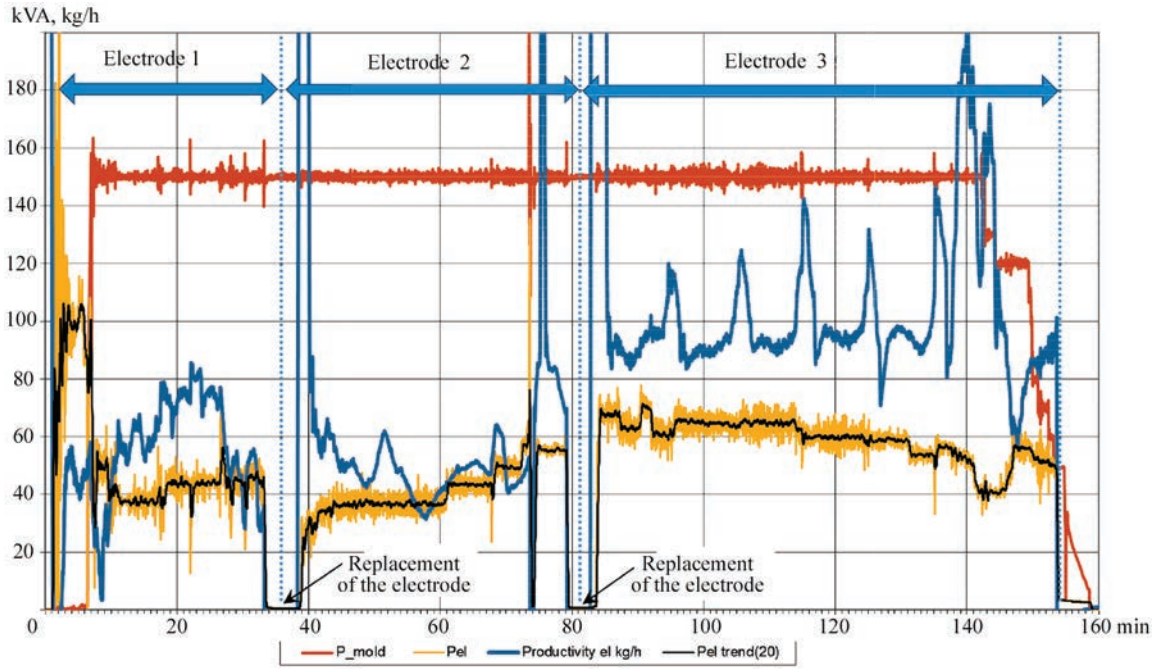

Figure 6. Plot of parameters during melt 2: P_{mold} — power supplied to the current-conducting section of the mold; P_{el} — power supplied to the electrode; Productivity el kg/h — electrode productivity in kg/h; P_{el} trend(20) — electrode power trend with linear filtering over 20 values

bility of the electrical regime, short-term productivity variations did not affect the quality of the ingot. This is confirmed by the surface appearance of the experimental ingots (Figure 5, *c*).

Thus, the design of the electrode directly affects the stability of the process and the productivity level of electroslag remelting. At the same time, the use of the TC ESR technology with a current-conducting mold allows for significant compensation of destabilizing effect caused both by unpredicted changes in the filling ratio during remelting and by electrode heterogeneities, ensuring a uniform and controlled process.

During experimental melt 3, two electrodes were sequentially remelted, the design of which replicated the third electrode from the second melt (Figure 5, *a*). Remelting modes were determined based on the results of the previous melt. The process was started with a dry start using a graphite electrode to form a bath of molten slag in the mold. After that, the current-conducting mold circuit was switched on, and the graphite electrode was replaced with a consumable electrode. The remelting was then carried out while maintaining a stable electrical regime (Figure 7). Analysis of the productivity plot showed a clear correlation with the structure of the assembled electrode: short-term productivity jumps occurred at the moments of transition between individual welded segments.

Samples from the head and bottom parts of the produced ingots were taken to determine their chemical composition using X-ray spectral analysis. The results are presented in Table 6: samples 1-1 and 2-1 correspond to the bottom part of the ingots, while 1-2 and 2-2 correspond to the head.

Analysis of the chemical composition of the experimental ingot metal (Table 3) confirmed full compliance with the requirements for the nickel alloy

Table 5. Chronometry of mode changes during experimental melt 2 (according to Figure 6)

Time interval, min	Process mode
0–6	Starting mode. Electric power applied to the electrode
7–34	Electrode 1 remelting. Two-circuit mode. Power distribution between electrode/mold — approximately 50/150 kVA. Productivity 70–80 kg/h
35–39	Replacement of the electrode
40–79	Electrode 2 remelting. Two-circuit mode. Power distribution between electrode/mold — approximately 40–50/150 kVA. Productivity 50–70 kg/h
80–84	Replacement of the electrode
85–154	Electrode 3 remelting. Two-circuit mode. Power distribution between electrode/mold — approximately 50–70/150 kVA. Productivity 100–110 kg/h

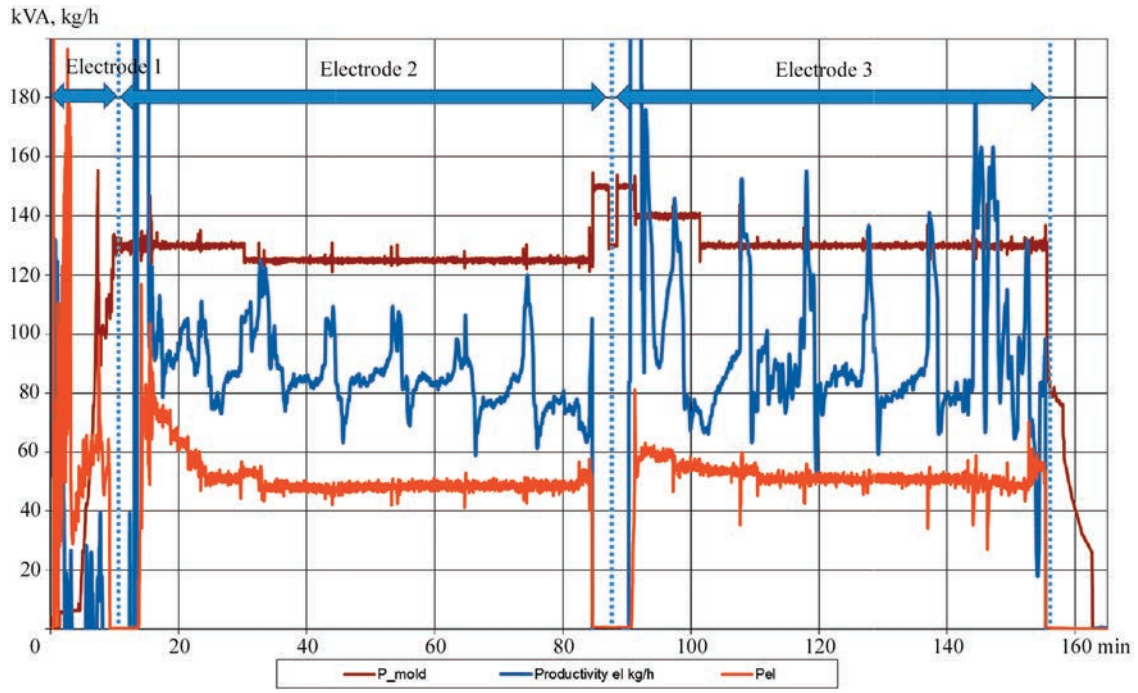

Figure 7. Plot of the parameters of experimental melt 3: P_{mold} — power supplied to the current-conducting section of the mold; P_{el} — power supplied to the electrode; Productivity el, kg/h — electrode productivity in kg/h

Table 6. Chemical composition of the experimental ingot metal, wt.%

Sample	Al	Ti	Cr	Fe	Ni	Nb	Mo	W
1–1	0.65	1.01	33.5	0.47	Base	0.75	3.3	4.9
1–2	0.62	1.08	34.05	0.41		0.68	3.1	4.4
2–1	0.55	0.93	33.6	0.5		0.58	3.0	4.6
2–2	0.52	1.09	34.7	0.45		0.66	3.3	4.7

EP648 according to TU 14-1-4103–86 (Table 1). The experimental ingots were transferred to production, where they were forged into rings. The finished products passed quality control and were approved for further use as intended.

Thus, the developed and tested single-stage recycling technology for EP648 nickel alloy process scrap based on the ESR process ensures the production of ingots suitable for direct use in the production cycle.

CONCLUSIONS

The conducted experimental studies confirmed the feasibility of recycling nickel alloys using a single-stage scheme based on ESR technology with a current-conducting mold. TC ESR technology with a current-conducting mold allows for compensation of destabilizing factors associated with the heterogeneity and variable geometry of consumable electrodes, while the overall energy and technological characteristics of the process remain acceptable for industrial application.

On the ESR R-951 installation, the features of remelting consumable electrodes of variable cross-section, formed from two types of EP648 nickel alloy process scrap, were thoroughly studied. Rational process parameters were determined, in particular, the optimal power distribution between the consumable electrode and the current-conducting mold at a level of 1/3, which ensures remelting stability. Under these conditions, remelting productivity was approximately 80 kg/h.

Analysis of the chemical composition of the obtained ingots showed full compliance with the normative requirements for the EP648 alloy, indicating the effectiveness of the developed approach in preserving alloying elements even when using assembled electrodes. It was determined that the ingots obtained through ESR recycling are suitable for direct use in the production cycle.

Thus, the tested technology ensures the return of EP648 nickel alloy process scrap into the production cycle, opening up prospects for reducing production costs through more rational use of expensive alloyed metals. Further research should focus on studying the impact of different electrode assembly schemes on process stability and on extending the technology to other nickel and high-alloy grades.

References

1. Branca, T., Colla, V., Algermissen, D. et al. (2020) Reuse and recycling of by-products in the steel sector: Recent achievements paving the way to circular economy and industrial symbiosis in Europe. *Metals*, 10(**345**). DOI: https://doi.org/10.3390/met10030345

2. Domenech, T., Bahn-Walkowiak, B. (2019) Transition towards a resource efficient circular economy in Europe: Policy lessons from the EU and the member states. *Ecological Economics*, **155**, 7–19. Elsevier, Amsterdam. DOI: https://doi.org/10.1016/j.ecolecon.2017.11.001
3. Xie, J., Xia, Z., Tian, X., Liu, Y. (2023) Nexus and synergy between the low-carbon economy and circular economy: A systematic and critical review. *Environmental Impact Assessment Review*, **100**, 107077. DOI: https://doi.org/10.1016/j.eiar.2023.107077
4. Feng, H., Chen, L., Liu, X., Xie, Z. (2017) Construction design for an iron and steel production process based on the objectives of steel yield and useful energy. *Inter. J. of Heat and Mass Transfer*, **111**, 1192–1205. DOI: https://doi.org/10.1016/j.ijheatmasstransfer.2017.04.096
5. Watari, T., Mclellan, B. (2024) Decarbonizing the global steel industry in a resource-constrained future — A systems perspective. *Philosophical Transact. of the Royal Society A*, 382(**2284**), 20230233. DOI: https://doi.org/10.1098/rsta.2023.0233
6. Diener, D.L., Tillman, A.M. (2016) Scrapping steel components for recycling — Isn't that good enough? Seeking improvements in automotive component end-of-life. *Resources, Conservation and Recycling*., **110**, 48–60. DOI: https://doi.org/10.1016/j.resconrec.2016.03.001
7. Wu, L., Liu, K., Mei, H. et al. (2022) Thermodynamics analysis and pilot study of reusing medium and high alloy steel scrap using induction melting and electroslag remelting process. *Metals*, 12(**6**), 944. DOI: https://doi.org/10.3390/met12060944
8. Varvara, D.A.I., Tintelecan, M., Aciu, C. et al. (2019) An assessment of the substance losses from charge composition used to the steelmaking — Key factor for sustainable steel manufacturing. *Procedia Manufacturing*, **32**, 15–21. DOI: https://doi.org/10.1016/j.promfg.2019.02.177
9. Gandhewar, V.R., Bansod, S.V., Borade, A.B. (2011) Induction furnace — A review. *Inter. J. of Eng. and Techn.*, 3(**4**), 277–284.
10. Arh, B., Podgornik, B., Burja, J. (2016) Electroslag remelting: a process overview. *Materials and Technology*, 50(**6**), 971–978. DOI: https://doi.org/10.17222/mit.2016.108
11. Mitchell, A. (2008) Electroslag technology for aerospace alloys. *Advances in Electrometallurgy*, **4**, 31–36 [in Russian].
12. Walek, J.,Odehnalová, A., Kocich, R. (2024) Analysis of thermophysical properties of electroslag remelting and evaluation of metallographic cleanliness of steel. *Materials*, 17(**18**), 4613. DOI 10.3390/ma17184613
13. Biktagirov, F.K., Veretilnyk, O.V., Shapovalov, V.O. et al. (2021) Comparative indices of different methods of processing shavings of high-alloyed steels and alloys. *Suchasna Elektrometalurhiya*, **4**, 11–15 [in Ukrainian]. DOI: https://doi.org/10.37434/sem2021.04.01
14. Kuskov, Yu.M., Ryabtsev, I.A., Kuzmenko, O.G., Lentyugov, I.P. (2020) *Electroslag technologies of surfacing and recycling of metal and metal-containing waste*. Kyiv, Interservice.
15. Mitchell, A. (2021) Electrode manufacture for the remelting processes. *Ironmaking & Steelmaking*, 48(**5**), 505–513, DOI: https://doi.org/10.1080/03019233.2020.1855690
16. Tsykulenko, A.K., Lantsmann, I.A., Medovar, L.B. et al. (2000) Two-circuit method of electroslag remelting consumable electrodes. *Advances in Special Electrometallurgy*, **3**, 141–144.
17. Dong, Y., Jiang, Z., Cao, H. et al. (2016) Study of single-power, two-circuit ESR process with current-carrying mold. Development of the technique and its physical simulation. *Metallurgical and Materials Transact. B*, 47(**6**), 3575–3581. DOI: https://doi.org/10.1007/s11663-016-0813-8
18. Medovar, L., Stovpchenko, G., Jianjun, G. (2024) State of the art of electroslag refining and challenges in the control of ingot cleanness. In: *Proc. of 12th Inter. Conf. on Molten Slags, Fluxes and Salts MOLTEN 2024*. Brisbane, AusIMM, ID: P-04120-D5P7M3.
19. Medovar, L., Fedorovsky, B., Petrenko, V. (2005) ESR with two power sources and process control. In: *Proc. of Inter. Symp. on Liquid Metal Processing and Casting*, *Santa-Fe, New Mexico*, 131–135.
20. Pedchenko, Ye., Medovar, L., Kostetsky, Yu. (2022) Electroslag remelting as a method of recycling non-compact high-speed steel tools. In: *Proc. of 31st Inter. Conf. on Metallurgy and Materials*. Brno, TANGER Ltd, 142–148. DOI: https://doi.org/10.37904/METAL.2022.4455
21. Pedchenko, Ye.O., Petrenko, V.L., Kostetskyi, Yu.V. et al. (2025) Electroslag remelting of variable cross-section electrodes using a two-circuit scheme. In: *Proc. of the VII Inter. Conf. on Welding and Related Technologies WRT 2024*. Yaremche, CRC Press, 25–28. DOI: https://doi.org/10.1201/9781003518518-5
22. Kuskov, Yu.M., Solovyov, V.G. (2018) Experimental study of slag and metal bath rotation during electroslag process in current-feeding mould. *Avtomaticheskaya Svarka*, **7**, 41–43 [in Russian]. DOI: https://doi.org/10.15407/as2018.07.07
23. Reitz J., Wietbrock B., Richter S. et al. (2011) Enhanced homogenization strategy by electroslag remelting of high-manganese TRIP and TWIP steels. *Advanced Eng. Materials,*13(**5**), 395–399. DOI: https://doi.org/10.1002/adem.201000322

ORCID

Yu.V. Kostetskyi: 0000-0003-0742-0684,
V.P. Petrenko: 0000-0003-2440-1901,
E.O. Pedchenko: 0000-0002-8824-4389,
G.O. Polishko: 0000-0001-7543-280X,
V.A. Zaitsev: 0000-0003-2498-8191

CONFLICT OF INTEREST

The Authors declare no conflict of interest

CORRESPONDING AUTHOR

Yu.V. Kostetskyi
E.O. Paton Electric Welding Institute of the NASU
11 Kazymyr Malevych Str., 03150, Kyiv, Ukraine.
E-mail: y.kostetsky@paton.kiev.ua

SUGGESTED CITATION

Yu.V. Kostetskyi, V.P. Petrenko, E.O. Pedchenko, G.O. Polishko, V.A. Zaitsev (2025) Recycling of nickel alloys by electroslag remelting.
The Paton Welding J., **12**, 41–48.
DOI: https://doi.org/10.37434/tpwj2025.12.06

JOURNAL HOME PAGE

https://patonpublishinghouse.com/eng/journals/tpwj

Received: 15.09.2025
Received in revised form: 14.10.2025
Accepted: 18.12.2025

DOI: https://doi.org/10.37434/tpwj2025.12.07

INVESTIGATION OF THE CAUSES OF DAMAGE TO THE WATER-WALL TUBES OF THE BOILER COOLER FOR CONVERTER GASES

S.O. Osadchuk, L.I. Nyrkova, L.V. Goncharenko

E.O. Paton Electric Welding Institute of the NASU
11 Kazymyr Malevych Str., 03150, Kyiv, Ukraine

ABSTRACT

The water-wall tubes of the boiler cooler for converter gases, which were damaged after five years of operation, have been examined. Optical microscopy revealed that corrosion damages in the form of cracks, oriented perpendicularly to the tube axis on the inner surface, propagated through intergranular corrosion along the boundaries of ferritic and pearlitic components. It was found that steam-water corrosion processes occurred on the inner surface of the tube, following the reaction of $3Fe + 4H_2O = Fe_3O_4 + 4H_2$ with hydrogen release, leading to the formation of small ulcers that developed into cracks due to the loss of integrity of the protective layer under operational thermal loads and mechanical stresses in local areas. The main cause of damage to the water-wall tubes is steam-water corrosion.

KEYWORDS: carbon steel, water-wall tubes, boiler cooler, inner corrosion, steam-water corrosion

INTRODUCTION

The boiler unit contains heat exchange surfaces for utilising flue gas heat. The main steam-generating surface of the boiler is seamless hot and cold deformed water-wall tubes made of carbon steel. Low- and medium-pressure boilers use gas-tight water walls made of fin or conventional tubes joined along the entire length by a welded strip [1]. The high corrosion resistance of boiler tubes is predetermined by the presence of a corrosion-resistant layer formed during operation. The effectiveness of the protective effect of this layer depends on its density and adhesion strength to the tube surface, which ensures its ability to protect against external chemical or physical and mechanical impacts. However, during the operation of heat and power equipment, damage can occur due to steam decomposition with the release of oxygen and hydrogen following the reaction $H_2O \rightarrow H_2 + O_2$, which causes the gradual destruction of the protective layer.

The effect of steam on the Fe_3O_4 protective layer can be caused by the properties of water: pH, salt and oxygen content, presence of copper, etc. The mechanical interaction depends on temperature, especially its fluctuations; scale formation, which leads to overheating of certain surface areas; reduction in the speed of the steam-water mixture [2].

CAUSES OF TUBE DAMAGE

Internal factors of tube damage include composition, heterogeneity and mechanical stresses, for example, due to welding or surfacing of metal. Carbon and low-alloy steels contain many elements (silicon, manganese, sulphur, etc.), that can form nonmetallic inclusions, which facilitate localized pitting corrosion and corrosion cracking. Steel heterogeneity can be a dominant factor under conditions of hydrogen depolarization corrosion. In this case, the corrosion rate is controlled by the hydrogen ion discharge reaction rate, which is catalytically accelerated by cathodic surface contamination [2].

In closed systems, corrosion with hydrogen release increases with growing temperature. Thermal loads on heating surfaces (heat flux density) also accelerate tube corrosion. For example, the corrosion potential of steel in condensate at a pressure of 10 MPa shifts from –0.7 to –0.9 V when the temperature changes from 0 to 400 °C [2] due to partial destruction of the protective film as a result of thermal stresses in the film arising from different coefficients of volumetric and linear expansion of the film and steel; mechanical impact of steam bubbles that form intensively on the metal surface; and the reducing effect of atomic hydrogen on the film. Atomic hydrogen is always formed when highly heated water comes into contact with steel as a result of hydrogen depolarization corrosion.

CORROSION OF HEATING SURFACES IN CONTACT WITH STEAM AND WATER

The heating surfaces of boilers are subject to external corrosion (by combustion products) and internal corrosion (by the heated medium) [1]. Carbon steel tubes in contact with steam and water sometimes suffer from corrosion damage due to both uniform and localized corrosion (oxygen, shutdown, alkaline, steam-water, hide-out, corrosion fatigue), which is accelerated by temperature [1, 2].

Carbon steel at a temperature of 120–150 °C in pure water mostly undergoes uneven corrosion with the formation of corrosion spots; at a temperature of 200–300 °C, corrosion spots become less; at a temperature of 350 °C, the surface is covered with a dark gray layer and corrosion spots are almost absent. To reduce steel corrosion in purified water, it is necessary to control the oxygen content [3].

OXYGEN CORROSION

which is observed both during operation of the boiler and when it is in reserve [1], manifests itself in the form of ulcers covered with iron corrosion products. Corrosion products, which are firmly bonded to the metal and have a black colour, are formed by magnetite Fe_3O_4. Oxygen corrosion occurs mainly in places where moisture accumulates, especially during downtime under a film of condensed steam [2]. Ulcers on the elements of the boiler which is out of service indicate *shutdown corrosion* [1]. To protect steam and hot water boilers from oxygen corrosion, thermal deaeration of feed and make-up water is used, as well as preservation of the boiler when it is in reserve or under repair. Protection against shutdown corrosion is carried out by using a solution of ammonia or gaseous nitrogen when the boiler is idle for more than 1–2 months; by filling the boiler with deaerated water and maintaining a constant excess pressure in it — up to three days.

Iron corrodes in water even in the absence of oxygen. In the condensate, iron acts as an anode, so it is oxidized. The fraction of the ferrous ion (Fe^{2+}) depends on the temperature of the medium, pH, and flow conditions. At low temperatures, Fe^{2+} reacts with water forming insoluble ferrous hydroxide $Fe(OH)_2$. If the condensate flow rate is high enough, colloidal $Fe(OH)_2$ is carried downstream and deposited elsewhere. In areas of low flow rate, $Fe(OH)_2$ is deposited near the oxidation site, forming a porous oxide layer. [4].

STEAM-WATER CORROSION

is the destruction of metal as a result of the chemical interaction of metal with steam water [2]: $3Fe + 4H_2O \rightarrow Fe_3O_4 + 4H_2$. Copper, which enters from the elements of the feed water tract together with iron oxides, has a catalytic effect and contributes to the release of hydrogen [2]. The destruction of carbon steel becomes possible at temperatures above 400 °C. The products of the interaction reaction are gaseous hydrogen and magnetite. Steam water corrosion is uniform and local in nature. In the first case, a layer of corrosion products is formed, sometimes silver in colour. Local corrosion takes the form of ulcers, grooves and cracks. The main cause of steam-water corrosion is the heating of the tube wall to a critical temperature, at which the metal oxidation reaction with water intensifies. This is facilitated by a number of conditions, including poor circulation in the tube; high heat flux densities (more than $230 \cdot 10^3$ W/m^2); the appearance of a film boiling mode, which leads to overheating of the metal. Prevention of steam-water corrosion is carried out by eliminating the causes that provoke overheating of the tube metal. It should be noted that this corrosion cannot be eliminated by changing or improving the water-chemical regime of the boiler unit, since the causes of steam-water corrosion depend on the hydrodynamic processes in the boiler, as well as operating conditions [2]. It is emphasized [5] that steam-water corrosion occurring in a weakened area can be the initial stage of hydrogen embrittlement and create some prerequisites for hydrogen attack — destruction of the protective magnetite layer and release of hydrogen. At present, there are known cases of steam-water corrosion damage not only of horizontal but also of vertical water-wall tubes, for example, near welds made by resistance welding or using backing rings.

ALKALINE CORROSION

of heating surfaces, which occurs by an electrochemical mechanism, manifests itself in the form of localized fractures (grooves) of water-wall tubes and brittle damage (intercrystalline cracks — alkaline or caustic brittleness) in places of boiler water evaporation [2]. In most cases, alkaline corrosion of heating surfaces is accompanied by steam-water corrosion [1, 2], in particular, it develops on thermally stressed tubes of the water-wall system [2]. Corrosion cracking, which occurs by the intercrystalline mechanism, is caused by high tensile stresses in tubes that come in contact with boiler water; the presence of dissolved caustic soda in the boiler water and high relative alkalinity of boiler water, exceeding 20 % [1]. The mechanism of alkaline corrosion in the form of brittle (non-deformation) cracks consists in the occurrence of a potential difference between the grain body and its boundary in the stressed metal. At temperatures above 200 °C, protective films are destroyed under the action of concentrated (evaporated) solutions of caustic soda (5–10 %) in places of poor circulation of boiler water, which has hydrated and carbonate alkalinity [2].

HIDE-OUT CORROSION

occurs under the sludge layer by electrochemical and chemical mechanisms due to contamination of the feed water with iron and copper oxides [1, 2]. Corrosion manifests itself in the form of ulcers and pits with sharply defined contours. Corrosion of water-wall tubes can occur both at high and normal alkalinity of

boiler water [2]. The difference in the chemical composition of boiler water has almost no effect on the initiation of corrosion. The main cause is contamination of the feed water with copper and iron oxides [2]. Damage to the metal surface, regardless of its origin, in the presence of iron and copper oxides become centres of hide-out corrosion [1].

CORROSION FATIGUE

is a specific form of damage associated with the simultaneous action of corrosion and cyclic thermal stresses. In this case, transcrystalline cracks appear [1].

The water-chemical regime, which is generally described in NPAOP 0.00-1.81 [6], should provide the operation of the boiler and the feed tract without damage to their elements due to the deposition of scale and sludge, an increase in the relative alkalinity of the boiler water to dangerous limits or due to metal corrosion. The choice of the method of water treatment for feeding boilers must be carried out in accordance with the requirements of the manufacturer's operational documentation.

The experience of operating boilers has shown that damage to water-wall tubes is associated with the initiation and growth of transverse cracks on the inner surfaces oriented towards the plume, which arise first of all due to primary deposits on the outer surface of the tubes [7]. Others consider this phenomenon to be the result of internal tube corrosion, the types of which have been discussed above [1, 2].

Despite a stable circulation of water in the side water wall and the compliance of its velocity with the calculated values, the main cause of metal ruptures in the water-wall tube is corrosion and local overheating of the wall in the area of internal deposits [8].

Corrosion failure of the steam generator module tube resulted in steam leakage from the gas-facing tube. Due to the destruction of the oxide layer on the inner surface of the tube, cracks from fatigue loading were formed and propagated, which led to microstructural degradation and transcrystalline cracking [9].

The conducted analysis showed that to date, the issue of determining the type of corrosion of the tubes of the boiler heating surfaces, which causes their damage, has not been sufficiently studied.

THE AIM OF THE WORK

is to find the causes of damage to the water-wall surfaces of the boiler cooler for converter gases.

RESEARCH METHODS

The tubes of the water-wall surface of the boiler cooler for converter gases with an internal diameter of 32 mm and a wall thickness of 5 mm made of carbon steel 20 of the composition, wt.%: C — 0.18; Si — 0.30; Mn — 0.52; S — 0.009; Cr — 0.07; Ni — 0.09; Cu — 0.13 were investigated. A protective water wall in the form of tubes, designed for radiation protect of the lower chambers from the converter and mechanical action from the converter neck, is placed in the lower part of the boiler. The gap between the tubes is rewelded with a strip.

The specimens were examined with the naked eye in daylight. Corrosion products were removed in a 20 % acetic acid. Corrosion damage was revealed according to [10]. Metallographic examinations were performed in a NEOPHOT 21 microscope using an Allied Vision 1800 U-2050c digital camera and SEO ImageLAB v1.0 software on unetched sections and after etching them in a 4 % alcoholic solution of nitric acid. The ferrite grain size was determined according to [11]. The analysis of deposits from the inner surface of the tube specimen was carried out by ICP-spectral analysis using an iCAP 6500 DUO Termo E.C. instrument.

PRESENTATION OF THE MAIN MATERIAL. RESEARCH AND ANALYSIS OF THE OBTAINED RESULTS

ANALYSIS OF OPERATING CONDITIONS OF WATER-WALL TUBES

Cooler for converter gases is a vertical water-tube, single-drum steam boiler with a volume of 170 m^3 with forced circulation, designed to cool heavily dusty high-temperature gases entering during the steel melting process from the converter into the gas purification unit. The composition of converter gases at the time of maximum gas release is as follows: carbon monoxide CO — 47 %; carbon dioxide CO_2 — 21.5 %; nitrogen N_2 — 30 %; hydrogen H_2 — 1.5 %; dust — 65 %. It should be noted that high-temperature converter gases contain hydrogen (1.5 %), but are in contact with the outer surface of the water-wall tubes.

The operating pressure of the boiler is 20 kgf/cm^2, the saturated steam temperature is 250 °C, the gas temperature at the converter outlet is 1700 °C; at the cooler outlet during the main operating mode is 700 °C; the steam capacity is 280 t/h.

The main feature of the boiler operation is the cyclical supply of converter gases, and, as a result, a variable thermal load. Chemically purified water and steam-water mixture circulate in tubes, the outer surface of which is in contact with high-temperature converter gases. During operation, the boiler is washed and treated with chemical reagents. There were no deviations from the boiler operating modes. During the absence of electricity for 1 year, the boiler was decomissioned and preserved with nitrogen. The first corrosion damage in the tubes was detected after

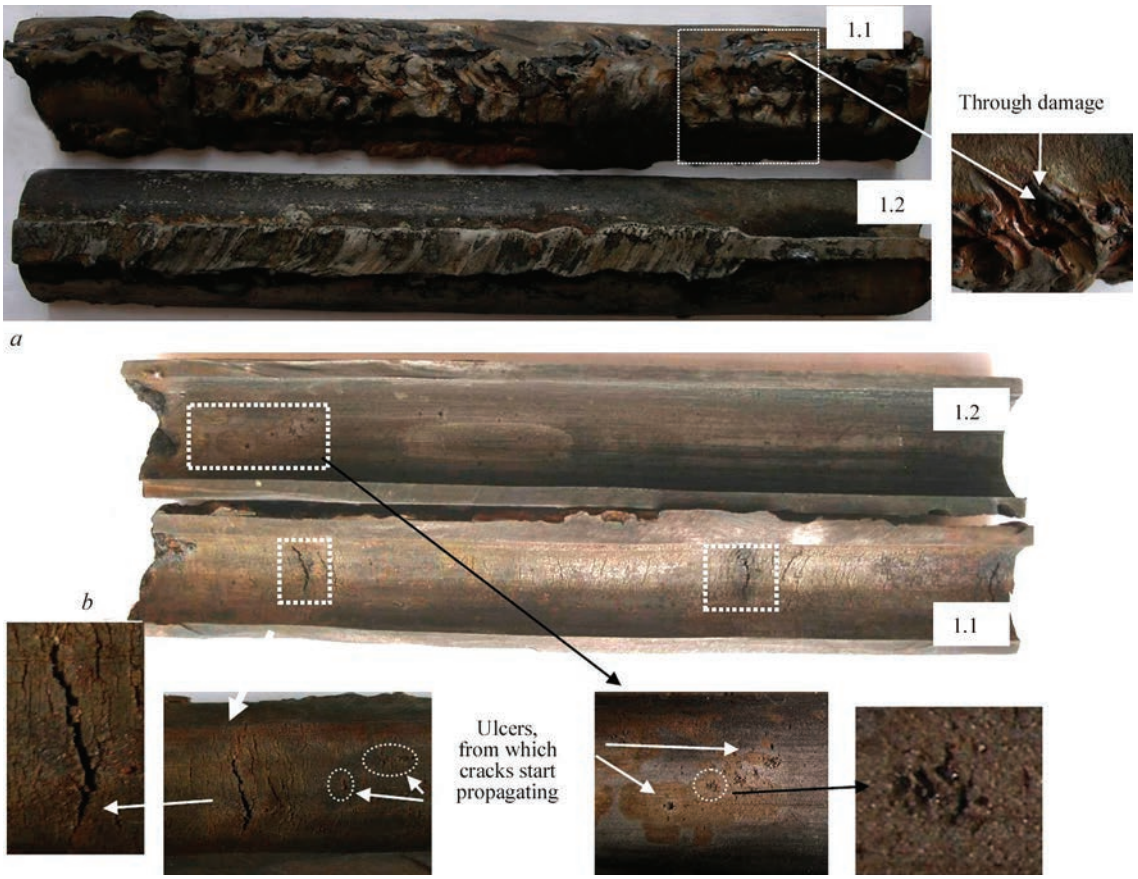

Figure 1. Appearance of the tube specimen cut out from the water-wall surface of the boiler cooler: *a* — outer surface; *b* — inner surface

5 years of operation. Repair of the emergency areas was carried out by replacing the tubes and rewelding the defects.

During the examination of a seamless tube specimen cut out from the boiler water-wall surface, it was found (Figure 1) that the outer surface is uneven, covered with a layer of dark gray products formed during the combustion of converter gases. On the outer surface of the specimen part (1.1) along the axis of the tube, a metal layer of approximately 40 mm in width was deposited in several layers using manual arc welding. In several places on the longitudinal deposited layer there are deposits across the axis of the tube. Within the deposited layer, small shallow cracks are visible, located transversely to the tube axis. At the boundary between the longitudinal and transverse deposited layers, propagated cracks and a through damage were revealed. On the outer surface of the other half of the specimen (1.2) along the tube axis, a metal strip of approximately 6 mm in size is welded-on, the reinforcement on which is removed. On this part of the tube, there are no cracks on either the inner or outer surfaces.

On the inner surface (Figure 1, *b*) a large number of small cracks were found across the tube axis. It is noted that larger cracks are located in areas of the specimen having a layer deposited across the tube on the outer surface, presumably made during the repair of cracks. The inner surface in this part of the tube is deformed. It has dark gray iron corrosion products (Figure 1, *b*), presumably magnetite, firmly bonded to the tube surface, individual small ulcers and transverse cracks of various sizes. Presumably, the cracks were formed and propagated during the transportation of the steam-water mixture. Their growth was accelerated by heating the outer surface of the tube during contact with converter gases heated to a high temperature, temperature changes during the steel melting process and mechanical stresses (due to the structural features of the water-wall, repair works by rewelding defects). In areas where the layer of deposited metal is thicker and there is a layer deposited across the tube from the outside, the cracks on the inner surface have a greater depth and opening (Figure 1, *b*). On the outer surface, corrosion is continuous, uneven and on the inner side it has the form of cracks [10].

Analysis of deposits from the inner surface of the tube (Figure 2) showed that their main component is iron (43.76 %). Silicon (0.04 %), manganese (0.85 %) were found, which are part of the tube metal and entered the system during operation as a result of dissolution. In addition, there are calcium (6.96 %),

magnesium (1.51 %), which form hardness salts, as well as zinc (0.96 %), aluminium (0.37 %), copper (0.07 %), etc. [2]. Sodium, which is present in the deposit (1.04 %), at high temperature in a strongly alkaline environment can create prerequisites for alkaline corrosion.

METALLOGRAPHIC EXAMINATIONS OF A WATER-WALL TUBE SPECIMEN

Metallographic sections revealed through and non-through (Figure 3) cracks, which demonstrate the propagation of corrosion from the inner surface. The structure of the tube metal is ferrite-pearlitic with pronounced banding. The ferrite grain size is 0.11–0.138 μm.

Due to prolonged heating, the structure underwent some changes (Figure 4): the structure of the zones located closer to the inner surface of the tube is characterized by a decrease in the density of the pearlite component preserving the banding (Figure 4, *a*). In the zones on the outer surface (Figure 4, *c*) a carbon phase was formed at the boundaries of the ferrite grains, its amount being greater than on the inner surface of the tube, which leads to embrittlement of the

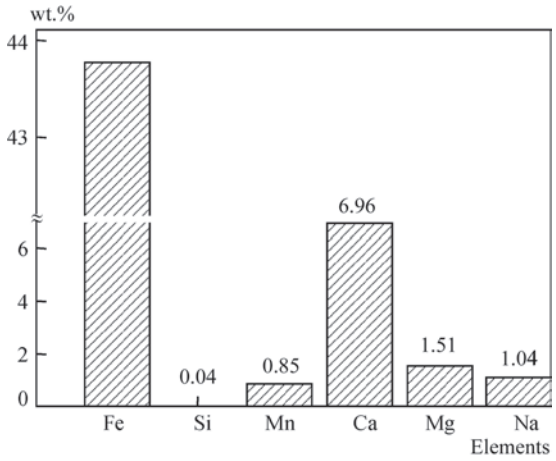

Figure 2. Chemical composition of the deposits on the inner surface of the tube

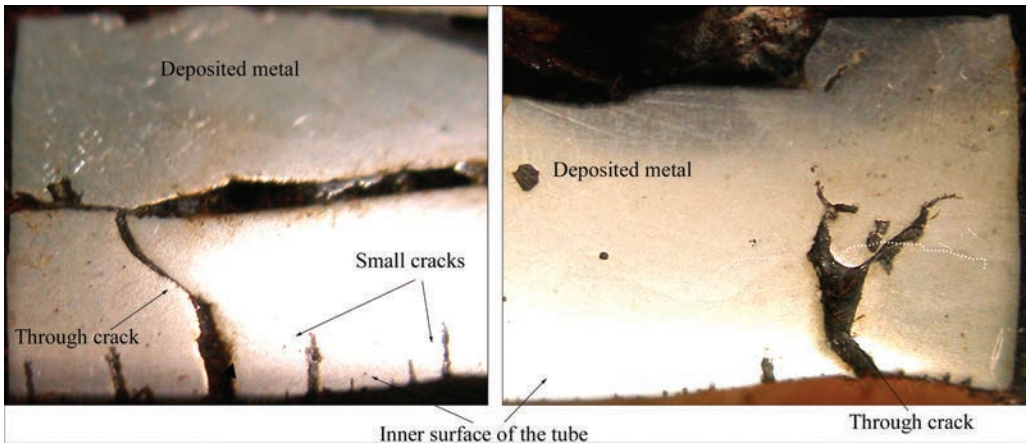

Figure 3. Appearance of cracks on the inner surface of the tube specimen

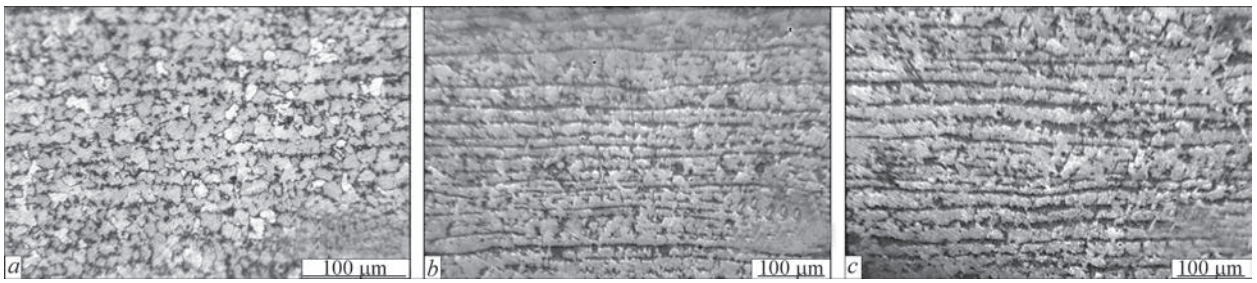

Figure 4. Microstructure of the tube specimen in the areas: next to the area with cracks (*a*), at a distance from the areas with cracks near the inner (*b*) and the outer surfaces (*c*)

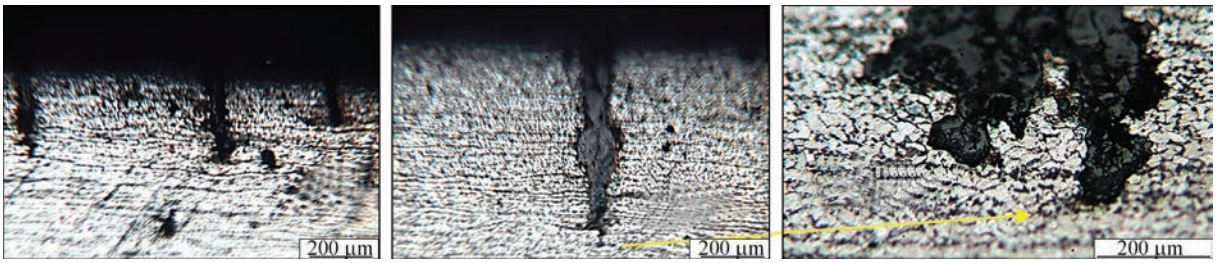

Figure 5. Cracks formed on the inner surface of the tube specimen after five years of operation

metal due to the accumulation of the second phase at the grain boundaries.

The revealed transverse brittle cracks with a maximum depth of 1.6 mm on the inner surface propagated perpendicularly to the tube axis (Figure 5). Near the crack walls, the curvature of pearlite bands is visible, which indicates deformation of the tube wall, presumably due to depositing metal layers from the outside. The cracks propagated in depth and width due to intergranular damage with grain separation along the boundary of the ferrite and pearlite components, apparently due to the action of hydrogen. The etching of the crack tip and its blunting indicate the course of anodic processes. Thus, it was found that corrosion damage in the form of cracks located transversely to the tube axis propagated from the inner surface by the mechanism of intergranular fracture along the boundaries of the ferrite and pearlite components.

CONCLUSIONS

Damage to the metal of the tubes of the water-wall surfaces of the boiler cooler for converter gases occurred on the inner surface due to a complex interaction of factors during operation: steam-water corrosion with the release of hydrogen, which contributes to the embrittlement of steel due to the absorption of hydrogen by the metal in places of destruction of the magnetite layer; thermal loads on the tube wall and mechanical stresses caused by the deposited layer on the outer surface. The causes of steam-water corrosion depend on the hydrodynamic processes in the boiler and depend little on the water-chemical regime of the boiler unit.

REFERENCES

1. Tkachenko, S.Y., Stepanov, D.V., Bodnar, L.A. (2016) *Boiler installations*: Training Manual. Vinnytsia, VNTU [in Ukrainian].
2. Akolzin, P.A. (1982) *Corrosion and protection of metal in thermal power equipment*. Moscow, Energoizdat [in Russian].
3. Zhijuan Zhao, Bingqing Cao, Dong Jin (2023) Research on corrosion of carbon steel in simulated boiler steam-water system. *J. of Physics: Conference Series*, **2539**, 012024. DOI: https://doi.org/10.1088/1742-6596/2539/1/012024
4. *Handbook of Industrial Water Treatment. Boiler Water Systems. Chapt. 19 — Condensate System Corrosion*. https://www.watertechnologies.com/handbook/handbook-industrial-water-treatment.
5. https://leg.co.ua/arhiv/generaciya/vodorodnoe-ohrupchivanie-parogeneriruyuschih-trub/Page-2.html [in Russian].
6. (2018) NPAOP 0.00-1.81–18: *Health and safety rules for operating pressurized equipment* [in Ukrainian].
7. Gladkov, V.E., Berezin, V.M., Bondar, K.M. (2009) Physical and chemical analysis of the conditions for the formation and growth of transverse cracks in screen tubes. *Vestnik YuUrGU*, **10**, 48–54 [in Russian].
8. Popov, M.S., Belyakov, I.I., Tolstyh, A.D. (2024) Analysis of damages to boiler screen tubes BKZ-160-100-GM. *Inter. J. of Industrial Eng.*, 2(**4**), 218–223. DOI: https://doi.org/10.61927/igmin168
9. Chae, H. (2021) Corrosion failure analysis of condensate pre-heater in heat recovery steam generator. *Corrosion Sci. and Technology*, 20(**2**), 69–76. DOI: https://doi.org/10.14773/cst2021.20.2.69
10. (1985) GOST 9.908–85: *Unified system for protection against corrosion and ageing. Metals and alloys. Methods for determining corrosion and corrosion resistance indicators* [in Russian].
11. (2019) DSTU 8972:2019: *Steels and alloys. Methods for detecting and determining grain size* [in Ukrainian].

ORCID

S.O. Osadchuk: 0000-0001-9559-0151,
L.I. Nyrkova: 0000-0003-3917-9063,
L.V. Goncharenko: 0000-0001-8371-2078

CONFLICT OF INTEREST

The Authors declare no conflict of interest

CORRESPONDING AUTHOR

L.I. Nyrkova
E.O. Paton Electric Welding Institute of the NASU
11 Kazymyr Malevych Str., 03150, Kyiv, Ukraine.
E-mail: lnyrkova@gmail.com

SUGGESTED CITATION

S.O. Osadchuk, L.I. Nyrkova, L.V. Goncharenko (2025) Investigation of the causes of damage to the water-wall tubes of the boiler cooler for converter gases. *The Paton Welding J.*, **12**, 49–54.
DOI: https://doi.org/10.37434/tpwj2025.12.07

JOURNAL HOME PAGE

https://patonpublishinghouse.com/eng/journals/tpwj

Received: 29.05.2025
Received in revised form: 18.08.2025
Accepted: 24.11.2025

AOTAI COBOTS: A NEW ERA OF WELDING AUTOMATION

Aotai Electric Corporation, known for its innovations in welding technology and welding equipment, has introduced its own line of collaborative robots (cobots) specially adapted for welding tasks. Unlike traditional industrial robots, AOTAI cobots Ai7 and Ai10 series (the technical parameters of which are presented in Table 1) are designed to work safely side by side with personnel without the need for massive protective barriers and comply with the ISO 10218-1 safety standard. Since safety is one of the most important characteristics of collaborative robots, they are equipped with advanced sensors such as torque sensors and collision detection systems and can immediately detect contact and limit the output force when interacting with people, preventing accidents without the need for physical protective barriers.

Table 1. Technical characteristics of Aotai Electric Cobots

	Ai10	Ai7
Weight	38.5 kg	24 kg
Payload	10 kg	5 kg
Repeatability	±0.02 mm	±0.02 mm
Range	1350 mm	786.5 mm
Reach	1513 mm	908.5 mm
Speed	1.9 m/s	3.0 m/s
Service life	30000 h	30000 h

Collaborative robots (cobots) are characterized by safety, ease of use, flexibility and integration. Safety is the basis of human-robot cooperation, as joint operations must ensure the protection of the operator.

Ease of use and flexibility are key advantages that allow cobots to quickly adapt to complex, flexible production processes. Integration allows cobots to penetrate diverse markets and complement human labor in a wide range of applications.

Aotai cobots are easy to use, allowing small and medium-sized workshops to automate work without the need for a specialized robotics engineer. One of the latest developments of Aotai Electric is the Mini COBOT Welding Station (see Figure 1), which mainly consists of a cobot, a welding machine and a welding platform.

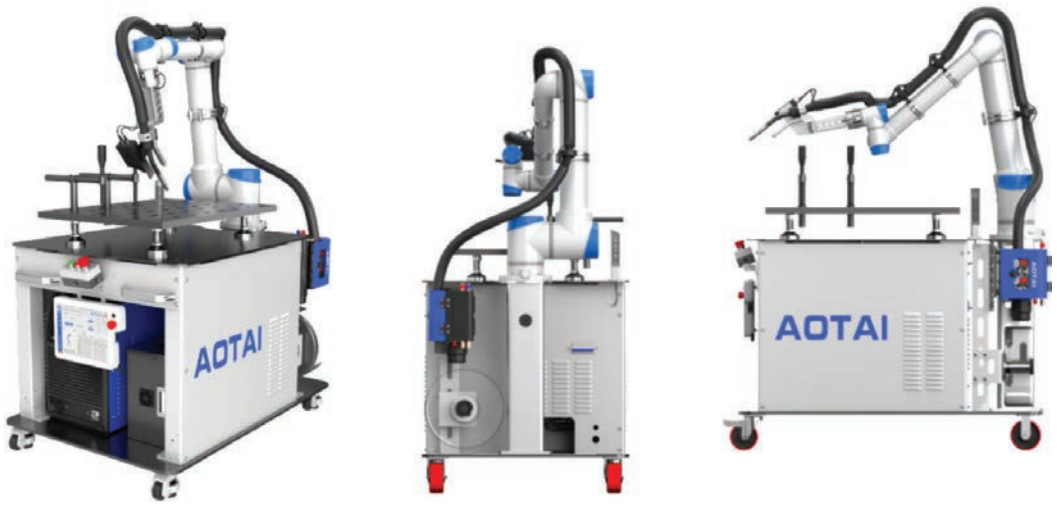

Figure 1. Mini COBOT Welding Station

This complex offers increased usability for welding tasks by integrating additional functions such as a flexible platform, a laser positioning system and other auxiliary equipment.

Its key features are as follows:

- Integrated arc welding software: Deep integration with the robot control system allows you to freely switch between welding modes and easily adjust welding parameters.
- User-friendly interface: The arc welding software has a clear structure and setup instructions, which simplifies the parameter configuration process for users.
- Laser sensing system: The integrated laser sensing system allows real-time position monitoring on the training pendant, which is conducive to accurate positioning.
- End tool with integrated buttons: The tool at the end of the cobot has buttons for switching operating modes, recording points and performing other functions, which ensures convenient operation.
- 4WD + encoder motor.

The system uses a fully digital motor control system with precise and stable wire feed powered by a 4WD motor + encoder motor, which provides efficient, accurate and user-friendly welding solutions.

Of particular note is the AOTAI Mini COBOT welding station (see Figure 2), which uses a magnetic base and a welding cart that integrates the welding machine and the robotic system for easy mobility and control.

Figure 2. AOTAI Mini Cobot Welding System

The magnetic base plate allows the robot to be securely fixed on steel structures. Equipped with a 10-meter wire feed cable, it provides convenient work in a wide working area.

Despite the fact that the main specialization of AOTAI cobots is arc welding (MIG/MAG, TIG), their versatility allows them to be used in the following areas: laser welding and cutting; grinding and polishing; palletizing and moving.

AOTAI cobots are not just a replacement for a welder, but also a powerful tool that can not only replace heavy and often repetitive work with improved quality and stability of obtaining high-quality seams, but also helps in the development, manufacture and implementation of new products, which leads to increased profitability of production.

SCIENTIFIC AND TECHNICAL CONFERENCE "WELDING AND RELATED TECHNOLOGIES FOR THE RECOVERY OF UKRAINE"

On February 27, 2025, E.O. Paton Electric Welding Institute (PWI), Kyiv, Ukraine hosted the scientific and technical conference "Welding and Related Technologies for the Recovery of Ukraine". More than seventy researchers, engineers, and industrial practitioners from institutes and organizations in Kyiv, Dnipro, Lviv, Kamianske, and Poltava took part in the event. The conference was held in the format of plenary and poster presentations.

Address by Academician of the National Academy of Sciences of Ukraine I.V. Krivtsun

The conference was opened by the Director of the E.O. Paton Electric Welding Institute, Academician of the National Academy of Sciences of Ukraine I.V. Krivtsun. He noted that the conference was dedicated to scientific and technical challenges in the field of welding and related technologies. Without exaggeration, it can be stated that welding technologies, which have been widely used in various branches of industry for more than one hundred years, remain among the most relevant areas of development in modern industrial production. The potential for further advancement of these technologies requires continued scientific research and practical validation, which is precisely the focus of this conference.

During the conference, the following plenary reports were presented:

Plenary presentation by D.I. Stelmakh

● Matviichuk V.A. "*GTE Components Made of VT6 Alloy: Additive Manufacturing and Properties*" (PWI);

● Kovalchuk D.V. "*xBeam 3D Metal Printing — New Research, Materials, and Technological Solutions*" (NVO "Chervona Hvilya", Kyiv);

● Yarovytsyn O., Cherviakov M., Motrunych S., Volosatov I., Zviagintseva G., Pestov V., Khrushchov H., Tomko D., Junwen D. "*Materials Science Challenges of Arc Additive Manufacturing of Inconel 625 Alloy Parts*" (PWI);

● Korzhyk V.M., Illyashenko Ye.V., Chygileichyk S.L., Torba Yu.I., Chechet O.V. "*3D Printing of Heat-Resistant Alloy Products by Additive Plasma-Arc Surfacing: New Technological Approaches and Equipment Development*" (PWI; JSC Zaporizhzhia Machine-Building Design Bureau "Progress"; Zaporizhzhia Polytechnic National University);

● Shapovalov Ye.V., Dolynenko V.V., Koliada V.O., Vashchenko V.M., Novodranov A.S., Vashchenko O.Yu., Mangold A.M., Klishchar F.S. "*Development and Research of a Robotic System for Implementing WAAM Additive Technology for Manufacturing Drilling Tools*" (PWI);

● Korzhyk V.M., Strohonov D.V., Tereshchenko O.S. "*Application of Arc Plasma Torches with Tubular Copper Electrodes for Producing Fine Spherical Metal Alloy Powders*" (PWI);

● Demchenko V., Nomirovskii D., Krivtsun I. "*Optimization of Current Pulse Shape Based on the Criterion of Force Action of*

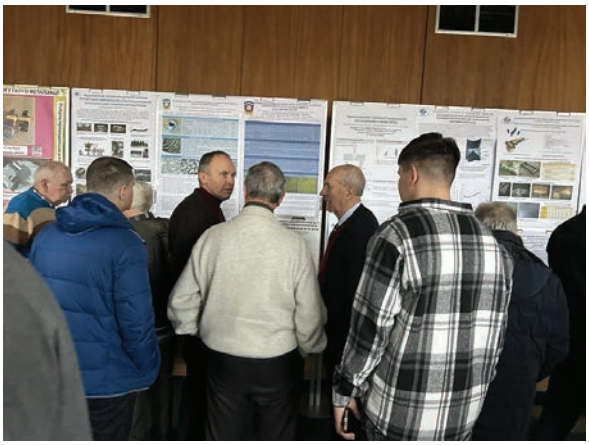

During the poster presentation session

Exhibition of equipment, materials, and technologies for welding and non-destructive testing

Modulated Current" (PWI; Taras Shevchenko National University of Kyiv);

● Kovalenko Dmytro, Krivtsun Igor, Biber Alexander, Mokrov Oleg, Pavlov Oleksii "*Features of Increasing Penetration in High-Frequency Pulsed TIG Welding of Carbon and Stainless Steel (Experimental Studies)*" (PWI; RWTH Aachen University; ISF — Welding and Joining Institute);

● Lobanov L., Stelmakh D., Dyadin V., Savytsky V. "*Technical Diagnostics of Bridge Conditions Based on Photogrammetry Using Unmanned Aerial Vehicles*" (PWI);

● Makhnenko O.V., Milenin O.S., Velykoivanenko O.A., Rozynka G.P., Makhnenko O.O. "*Numerical Analysis of the Operational Strength of Welded Absorber Rods of the Control and Protection System of the WWER-1000 Nuclear Reactor*" (PWI);

● Pavlii O.V. "*Digital Systems for Radiographic Inspection of Welded Joints*" (LLC Scientific and Production Firm "Diagnostic Instruments", Kyiv);

● Yudin Yu.V. "*AOTAI Collaborative Robots as a System Solution to Workforce Crises Caused by the Shortage of Qualified Workers at Industrial Enterprises*" (LLC "WTC", Kyiv).

The conference also featured 48 poster presentations in the fields of welding, electrometallurgy, non-destructive testing, technical diagnostics, and related technologies, prepared by specialists from Ukraine and countries outside the region.

Several companies participated in an express exhibition of equipment, materials, and technologies for welding and non-destructive testing, including:

● PJSC "OKO Association", Kyiv — a leading Ukrainian developer of ultrasonic and eddy-current flaw detectors, including those for rail and weld inspection;

● LLC "Scientific and Production Firm "Diagnostic Instruments", Kyiv — equipment and materials for non-destructive testing, as well as NDT and flaw detection services;

● LLC "WTC", Welding Technologies Center, Kyiv — a full range of pipeline welding equipment and AOTAI collaborative robots;

● LLC "VELTEK", Kyiv–Dnipro — a leader in the production of flux-cored wires in Ukraine;

● LLC "NVO "Chervona Hvilya", Kyiv — technologies for 3D printing of high-quality parts from titanium, niobium, stainless steel, copper, and other metals using xBeam 3D Metal Printing technology with welding wire;

● LLC "Promavtozvarka", Kyiv — welding equipment and systems for electric arc metallization.

The event brought together leading Ukrainian researchers, engineers, and representatives of industry, who presented current research results and technological developments in the fields of welding and materials science. Within the framework of the conference, advances in additive manufacturing, robotic systems, high-temperature materials, non-destructive testing, and digital technologies in welding processes were showcased. Special attention was paid to the application of modern technologies for the restoration of critical infrastructure, bridges, energy systems, and industrial facilities in the post-war period. Participants emphasized the importance of integrating scientific developments into practice, expanding cooperation between the scientific community and business, and training highly qualified specialists for the implementation of large-scale reconstruction projects.

The conference became a landmark event for experience exchange and for defining strategic directions in the development of welding technologies in Ukraine. The obtained results will contribute to strengthening the technological potential of the country and to the formation of effective solutions for rapid and safe infrastructure recovery.

Considering the scale of challenges in the field of welding in the implementation of Ukraine's reconstruction projects, the conference participants expressed their wish to hold a similar conference annually on November 27, the birthday of Academician Borys Paton.

The collection of conference abstracts is available at:
https://patonpublishinghouse.com/ukr/proceedings/WRT2025

Oleksandr Zelnichenko, Iryna Romanova
"PATON PUBLISHING HOUSE" LLC